THE STUDY OF EXCLUSIVE PION ELECTROPRODUCTION REACTION FROM KAON-LT EXPERIMENT AT JEFFERSON LAB HALL C

A Thesis

Submitted to the Faculty of Graduate Studies and Research

In Partial Fulfillment of the Requirements

for the Degree of

Doctor of Philosophy

In

Physics

University of Regina

By

ALI USMAN

Regina, Saskatchewan

July 2025

UNIVERSITY OF REGINA

FACULTY OF GRADUATE STUDIES AND RESEARCH

SUPERVISORY AND EXAMINING COMMITTEE

Ali Usman, candidate for the degree of **Doctor of Philosophy in Physics,** has presented a thesis titled, ***The study of exclusive pion electroproduction reaction from the Kaon-LT experiment at Jefferson Lab Hall C,*** in an oral examination held on **May 30, 2025**. The following committee members have found the thesis acceptable in form and content, and that the candidate demonstrated satisfactory knowledge of the subject material.

External Examiner:	Dr. Caroline Kathrin Riedl, University of Illinois Urbana-Champaign
Supervisor:	Dr. Garth Huber, Department of Physics
Committee Member:	Dr. David Gaskell, Jefferson Lab
Committee Member:	Dr. Zisis Papandreou, Department of Physics
Committee Member:	Dr. Gwen Grinyer, Department of Physics
Committee Member:	*Dr. Sandra Zilles, Department of Computer Science
Chair of Defense:	Dr. Chris Oriet, Faculty of Graduate Studies and Research

*Unable to attend

Abstract

A central problem of modern physics concerns our understanding of the internal structure of hadrons (baryons and mesons) within the Quantum Chromodynamics (QCD) framework. QCD predicts that partons (quarks and gluons), have dramatically different interaction strengths in different regimes. At very small impact parameter interactions (high momentum transfer, i.e. hard interactions), partons interact feebly and these interactions can reliably be described by perturbative QCD. At large impact parameter (small momentum transfer, i.e. soft interactions) partons interact with great strength, resulting in color confinement within hadrons. QCD also predicts that hadronic reaction amplitudes factorize into hard and soft parts from moderate to high momentum transfer. The pion is a good candidate for studies leading to our improved comprehension, due to its relatively simple structure and its experimental accessibility. Form Factors and Generalized Parton Distributions (GPDs) are important observables to understand hadron structure. GPDs can be extracted through experimental measurements of the cross-section of exclusive pion electroproduction reaction. This cross-section is dictated by the longitudinal and transverse polarizations of the virtual photon. Considering the recoil system in such a reaction, the ground state nucleon $p(e, e'\pi^+)n$ reaction has been studied in detail but little is known about the nucleon-to-resonance ($N \to \Delta$) transition GPDs. Experimental Hall C at Jefferson Lab is a unique facility that can host high precision studies of exclusive meson electroproduction reactions. Kaon-LT experiment is one of the first coincidence commissioning experiments using newly installed Super High Momentum Spectrometer (SHMS) in Hall C. A significant amount of work has been done by the author to understand and improve the performance of the Data Acquisition System (DAQ), target and magnet systems and particle detectors. The Kaon-LT experiment provides a unique opportunity to study the higher resonance pion electroproduction reaction $p(e, e'\pi^+)\Delta^0$ at momentum transfer ($2.0 < Q^2 < 6.0$ GeV^2), invariant mass ($W > 2.25$ GeV) and Mandelstam t ($0.15 < |t| < 1.0$ GeV^2). The final results include first ever measurement of the beam spin asymmetry and polarized cross-section ratio for the $p(e, e'\pi^+)\Delta^0$ reaction and comparison with the $p(e, e'\pi^+)n$ reaction in Hall C, as well as recent results from CLAS12.

Acknowledgments

I am sincerely grateful to my advisor, Dr. Garth Huber, for his unwavering support and mentorship throughout my PhD. His insightful guidance on my research, facilitation of hands-on training during multiple experiments, and encouragement to present at national and international conferences have been invaluable to my academic and professional development. I also deeply appreciate his support for my extra-curricular initiatives, which have enriched my experience and prepared me for future career opportunities.

I would like to extend my appreciation to all members of my research group at University of Regina. Their collaboration and feedback have fostered a supportive environment where we continuously learn from one another and contribute to each other's projects. My gratitude also goes to the Kaon-LT/Pion-LT Collaboration, particularly the spokespersons, for their dedicated guidance throughout my research. The collaborative spirit has provided me with opportunities to share my expertise while benefiting from the collective knowledge and contributions of others.

Finally, I would like to thank all the scientists and support staff at the Jefferson Lab for their expertise during data collection and analysis. In particular, I appreciate the support from Hall C SIDIS Collaboration in the simulation studies. All of these contributions were invaluable to the success of this work.

Post-Defense Acknowledgments

I would like to express my sincere gratitude to my PhD supervisory committee, Dr. David Gaskell, Dr. Zisis Papandreou, Dr. Gwen Grinyer, and Dr. Sandra Zilles, for their dedicated guidance, thoughtful advice, and encouragement throughout my studies. The important discussions during annual meetings were a highlight of my PhD. I am also thankful for their detailed feedback, which enhanced its clarity and quality of this thesis. I am equally grateful to my external examiner, Dr. Caroline Riedl, for her thorough review of my thesis and constructive questions during the defense. I appreciate her kind words about my research and defense.

I acknowledge that this work was primarily supported by the Natural Science and Engineering Research Council (NSERC) through grant [SAPIN-2021-00026] awarded to my supervisor. This work was also partially funded by Faculty of Science, the Faculty of Graduate Studies and Research, and the Office of the Vice President (Research) at the University of Regina.

I warmly thank Dr. Gwen Grinyer and Dr. Tanya Dahms for ensuring I had the resources and support to complete this work. Their encouragement also inspired my advocacy for improved services for graduate students. Finally, I am grateful to all the administrative staff for their professionalism and day-to-day assistance throughout my program. Working behind the scenes, they are the backbone of student success.

Contents

List of Figures

List of Tables

Transparency Statement

I declare no AI-assisted technology was used in the preparation of this thesis.

Chapter 1

Physics Motivation

1.1 Introduction

One of the important goals of modern physics is to understand the nature of matter at the most fundamental level. The universe, in all its complexity, is composed of elementary particles that interact through fundamental forces. These interactions govern everything from the stability of atoms to the processes occurring in the densest astrophysical objects. The Standard Model of particle physics (SM) provides the best theoretical framework to describe these particles and their interactions, but it remains incomplete. In particular, our understanding of how protons, neutrons, and other hadrons (the bound states of quarks) are structured within the framework of Quantum Chromodynamics remains one of the major unresolved questions in modern nuclear and particle physics.

At the heart of hadron structure studies lies the question: *How do quarks and* *gluons form the bound states observed in nature?* Unlike electrons, which are fundamental particles and do not exhibit internal structure, hadrons are composite objects bound together by the strong nuclear force. The strong force, described by QCD, is responsible for binding quarks (the elementary constituents of hadrons) together via the exchange of gluons (the mediating particles of strong interactions). Unlike other forces in nature, the strong force exhibits confinement, meaning quarks are never found in isolation but always within bound states. However, due to the complexity of QCD, the distribution of quarks and gluons inside hadrons is not straightforward to calculate from first principles [1].

Several fundamental open questions arise in this context:

- How are quarks and gluons distributed inside hadrons?
- What is the mechanism of confinement?
- How do hadrons acquire mass?
- How does the strong force behave in different energy regimes?

Understanding hadron structure is crucial for a wide range of physics, from interpreting results at high-energy particle colliders to modeling the properties of dense nuclear matter found in neutron stars. In the following sections, we will explore how QCD governs hadron structure, the role of pions in probing strong interaction dynamics, and how experimental techniques allow us to study these fundamental questions.

1.1.1 Standard Model

The Standard Model of particle physics is the most successful theoretical framework describing the fundamental building blocks of nature and the forces that govern their interactions. It was developed over several decades, with key contributions from many physicists, and has been experimentally verified with high precision. The Standard Model provides a comprehensive description of three of the four fundamental forces of nature, explaining how all known elementary particles interact. These forces are:

- **The Electromagnetic Force** is responsible for interactions between electrically charged particles, such as electrons and protons. It governs phenomena like electricity, magnetism, and light and is mediated by a particle called the photon (γ).

- **The Weak Nuclear Force** is responsible for radioactive decay and certain nuclear reactions. This force allows particles to change from one type to another (such as a neutron decaying into a proton), which plays a crucial role in nuclear fusion inside stars. It is mediated by the W and Z bosons.

- **The Strong Nuclear Force** is the most powerful of the three forces in the Standard Model. It binds quarks together inside hadrons, such as protons and neutrons, ensuring the stability of atomic nuclei. The force is mediated by gluons (g), which facilitate the interaction between quarks.

The fourth fundamental force, gravity, is not included in the Standard Model. Unlike the other forces, which are described using quantum field theory, gravity is best explained by Einstein's general theory of relativity, a classical theory of spacetime curvature. A quantum theory of gravity remains an open problem in physics.

The Standard Model organizes all known elementary particles into two broad categories: fermions, which make up matter, and bosons, which mediate interactions between them. Fig. 1.1 shows all the elementary particles in the Standard Model.

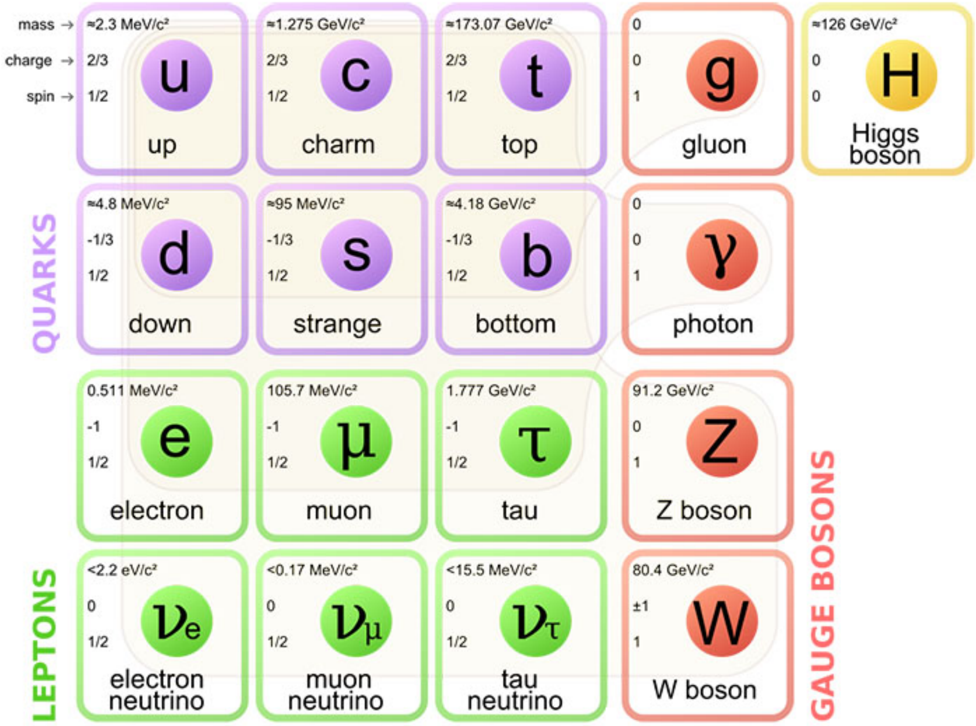

Figure 1.1: Elementary particles in the Standard Model of Particle Physics [2].

Fermions: The Building Blocks of Matter

All matter in the universe is composed of fermions, which are particles that obey the Pauli exclusion principle (meaning no two identical fermions can occupy the same quantum state simultaneously). Elementary fermions are further classified into quarks and leptons.

- Leptons are the fundamental particles that interact with each other through the electromagnetic force or weak nuclear force. They include electrically charged particles like electrons (which are a key component of atoms) and electrically neutral particles with extremely small masses (neutrinos). They interact only via the weak nuclear force and gravity. Neutrinos are produced in nuclear reactions, such as those in the Sun.

- Quarks are the fundamental constituents of hadrons. They interact via the strong force and cannot exist in isolation due to a property known as confinement. Quarks come in six different types, known as flavors. In addition to electric charge, quarks also possess color charge (a unique property of strongly interacting particles).

Each quark and lepton has an antiparticle, which has the same mass but opposite charge. For example, the positron (e^+) is the antiparticle of the electron.

Bosons: The Force Carriers

Bosons are quanta of fundamental fields, where vector bosons mediate the fundamental interactions between particles, and the scalar boson is responsible for mass of all elementary particles. The Standard Model includes the following bosons:

- Photon (γ) – The carrier of the electromagnetic force, responsible for electric and magnetic interactions.
- W and Z Bosons – The carriers of the weak nuclear force, responsible for processes such as beta decay.
- Gluons (g) – The carriers of the strong nuclear force, which bind quarks together inside hadrons. Unlike photons, gluons are subject to the force they mediate (self interaction), leading to complex interactions.
- Higgs Boson – This particle is responsible for giving mass to elementary particles through the Higgs mechanism. This is the only scalar boson in the Standard Model.

One of the key discoveries of particle physics is that quarks do not exist freely in nature. Instead, they are always confined inside composite particles called hadrons due to the strong nuclear force. The process that binds quarks together is governed by QCD. Hadrons are classified into two major categories:

- Baryons are composite particles made of three quarks (qqq) or anti-quarks ($\bar{q}\bar{q}\bar{q}$). The proton is a positively charged baryon found in all atomic nuclei. The neutron is a neutral baryon also found in atomic nuclei. The free neutron decays via beta decay.

- Mesons are composite particles made of a quark and an anti-quark ($q\bar{q}$). Pions ($\pi^+,\ \pi^-,\ \pi^0$) are the lightest mesons, playing a key role in mediating nuclear forces between protons and neutrons. Kaons ($K^+,\ K^-,\ K^0,\ \bar{K^0}$) are a heavier meson, important in studying fundamental symmetries of particle interactions.

Despite the successes of the Standard Model, there are still fundamental gaps in our understanding of hadron structure. Quarks are never observed in isolation, but the exact mechanism that forces them to remain bound inside hadrons is not yet fully understood. The internal structure of hadrons is determined by the momentum, spin, and spatial distributions of quarks and gluons. Understanding this structure is essential for advancing our knowledge of nuclear matter.

The proton's mass (938.27 MeV/c^2 [2]) is much larger than the sum of its current quarks' masses (9 MeV/c^2 [2]). If the Higgs mechanism is turned off, the proton would still retain substantial mass, which suggests that most of its mass arises from the energy of quark-gluon and gluon-gluon interactions [3]. Similarly, the spin of the proton (once thought to be entirely due to its quarks) is now known to have significant contributions from gluons and orbital angular momentum. At low energies, hadrons behave as bound states of quarks, while at high energies, they exhibit a more free particle behavior (known as asymptotic freedom). Understanding this transition is essential for improving our knowledge of hadron structure and parton (quarks and gluons) interactions.

1.1.2 Quantum Chromodynamics

Quantum Chromodynamics is the fundamental theory describing the strong interaction, which governs the behavior of quarks and gluons, the building blocks of protons, neutrons, and other hadrons. In QCD, the force between quarks is mediated by gluons, which themselves carry color charge (self-interact), leading to the property of confinement (quarks and gluons are never observed in isolation but always bound inside hadrons). Another essential feature of QCD is asymptotic freedom, meaning that at very high energies, quarks and gluons interact weakly, allowing perturbative techniques to be applied (strong coupling constant α_S is very small), whereas at low energies, interactions become strong and require non-perturbative methods.

The internal structure of hadrons is characterized by how quarks and gluons are distributed within them. These distributions are described by fundamental QCD observables extracted from high-energy scattering experiments. The most widely studied of these are parton distribution functions (PDFs), which describe the probability of finding a quark or gluon carrying a certain fraction of the hadron's longitudinal momentum. PDFs play a crucial role in interpreting high-energy reactions such as Deep-Inelastic Scattering (DIS), where a high-energy electron scatters off a nucleon, probing its internal partonic structure. The DIS reactions can either be inclusive (reactions where not all final state particles are detected) or exclusive (reactions where all final state particles are detected).

The exclusive reactions such as Deeply Virtual Compton Scattering (DVCS) and meson electroproduction provide additional insights into hadron structure. In these processes, the struck hadron remains intact or transitions into a specific final state, allowing access to more detailed information about the spatial and spin distributions of quarks and gluons. This information is encoded in GPDs, which extend the concept of PDFs by incorporating both longitudinal momentum and transverse spatial distributions. GPDs provide a unified description of hadron structure, linking form factors (quantities that describe the hadron's transverse spatial distribution) with the partonic distributions inside the nucleon.

Another approach to describing hadron structure, particularly at lower momentum transfers, is based on Regge theory. This framework models the exchange of families of particles, known as Regge trajectories, to explain high-energy scattering phenomena. Regge models have been successfully applied to describe the behavior of hadronic cross-sections at low and intermediate energies, complementing perturbative QCD approaches.

The interplay between PDFs, GPDs, and Regge-based models provides a comprehensive picture of hadron structure. While PDFs describe the longitudinal momentum distributions of partons, GPDs offer a more complete spatial and spin-dependent view, and Regge theory helps understand the hadronic interactions in the non-perturbative regime. High-energy experiments at facilities such as Jefferson Lab (JLab) and the future Electron-Ion Collider (EIC) are designed to explore these fundamental aspects of QCD, combining precise experimental data with theoretical advances to deepen our understanding of the strong interaction.

1.2 The Pion

The pion (π-meson) is the lightest meson and plays a crucial role in understanding the strong interaction. It was first proposed by Hideki Yukawa in 1935 [4] as the particle responsible for mediating the nuclear force that binds protons and neutrons within an atomic nucleus. The existence of the pion was experimentally confirmed in 1947 when pions were observed in cosmic rays [5]. Today, pions are central to the study of hadron structure and QCD. The fundamental properties of the three pion states are summarized in Table 1.1.

Unlike protons and neutrons, which are baryons composed of three valence quarks, pions are mesons (composed of valence quark and anti-quark pair) and have integer

Property	π^+	π^-	π^0
Quark Content	$u\bar{d}$	$d\bar{u}$	$\frac{1}{\sqrt{2}}(u\bar{u} - d\bar{d})$
Electric Charge	+1	-1	0
Mass	139.57 MeV	139.57 MeV	134.98 MeV
Spin	0	0	0
Mean Lifetime	2.6×10^{-8} s	2.6×10^{-8} s	8.4×10^{-17} s

Table 1.1: Properties of different pion states [2].

spin, making them bosons. They play a unique role in the Standard Model as pseudo-Goldstone bosons, arising from the spontaneous breaking of chiral symmetry in QCD. This means that pions are not fundamental force carriers like photons or gluons, but they emerge as a consequence of deeper symmetries in the theory of strong interactions. Pions are essential in studying hadron structure and the strong interactions for a variety of reasons.

- **Mediators of the Nuclear Force:** At low energies, pions mediate the residual strong interaction between nucleons (protons and neutrons) in the atomic nucleus. This interaction explains why atomic nuclei are bound together despite the repulsive electromagnetic force between protons. The properties of nuclei that we observe are dominantly because the pion is significantly less massive than the nucleon. If the pion mass was higher (2/3 the nucleon mass instead of 1/7), the universe would have a dramatically different structure. Hence, our existence is fundamentally linked to the mass and other properties of the pion.

- **Probes of Chiral Symmetry Breaking:** As a Goldstone boson, the existence of pions and their relatively low masses provide direct evidence for spontaneous chiral symmetry breaking in QCD. Understanding their properties helps physicists explore how the interactions between quarks and gluons give rise to the structure of hadrons.

- **Access to the Strong Interaction at Different Energy Scales:** Pions play a role in both the non-perturbative (low-energy) and perturbative (high-energy) regimes of QCD. Their interactions provide crucial experimental data for testing theoretical models of hadron structure.

- **Connections to GPDs and PDFs:** Pions contribute to our understanding of how quarks and gluons are distributed within nucleons, linking different aspects of hadron structure through QCD factorization (more details in Section 1.3).

Since direct observations of individual quarks and gluons are impossible due to confinement, studying pion structure allows scientists to infer information about the underlying quark-gluon dynamics. Pions can be studied through various experimental techniques, including pion-nucleon scattering and pion production in high-energy collisions. One of the most effective ways to investigate pion structure and interactions is through exclusive pion electroproduction, where an electron is used to probe pions. Electroproduction processes can be categorized as elastic or inelastic:

- **Elastic Pion Scattering:** The initial and final nucleons remain the same, meaning the internal structure of the nucleon does not change. While this process is useful for measuring basic pion properties, it has limitations because elastic reactions do not provide direct access to the internal quark-gluon dynamics.

- **Inelastic Pion Production:** The target nucleon transitions into an excited state or transforms into another hadronic state. This process is more sensitive to the internal quark structure of the nucleon and provides insight into how pions interact within the nucleon environment.

Although pion beams have been historically used to study hadron interactions, they suffer from several challenges. Since pions have a short mean life time (listed in Table 1.1), creating a stable pion target for scattering experiments is impossible. On the other hand, high-energy pion beams often contain unwanted particles (such as muons), making it challenging to isolate clean experimental data. Finally, traditional pion scattering experiments have limitations in reaching very high energy scales, where QCD effects become dominant. For these reasons, inelastic pion electroproduction has become a preferred method for studying pion structure. By using a well-controlled electron beam, experiments at facilities like Jefferson Lab can precisely probe the internal structure of hadrons through pion electroproduction.

1.2.1 Exclusive Pion Electroproduction

An indirect way of understanding pion structure is by studying exclusive pion electroproduction reactions. The exclusive reaction are those particle reactions in which the four momenta of all final state particles are directly measured or uniquely reconstructed. This can be done by scattering an electron beam off a nucleus. Since the pion is the mediator of the nuclear force, it is understood that nuclei carry a sea of virtual pions. Exclusive pion electroproduction in the t-channel, where the interacting photon scatters from this virtual pion cloud in a quasi-elastic process (left panel of Fig. 1.2) can result in production of a charged pion (π^+) along with a hadron i.e. $p(e, e'\pi^+)n$ or $p(e, e'\pi^+)\Delta^0$ [6]. Here, the e' corresponds to scattered electron. The reactions are given as follows:

$$e^- \; + \; p \; \rightarrow \; e^{-'} \; + \; \pi^+ \; + \; n, \tag{1.1}$$

$$e^- \; + \; p \; \rightarrow \; e^{-'} \; + \; \pi^+ \; + \; \Delta^0. \tag{1.2}$$

Fig. 1.3 illustrates the kinematics in the exclusive pion electroproduction reaction. It can be observed that the incident electron and the target proton interact by the

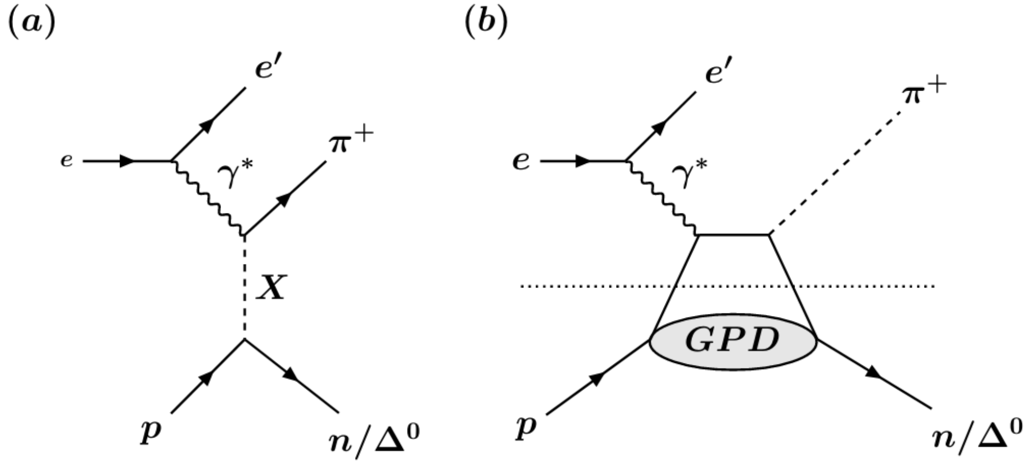

Figure 1.2: Feynman diagram for pion exclusive electroproduction. The left panel shows the Regge process and the right panel shows the GPD process.

exchange of a virtual photon γ^* (in the scattering plane). In the final state there is a scattered electron, a positively charged pion π^+ and a hadron (in the reaction plane). There are a number of important kinematic quantities in this reaction. The equations for these quantities are given in Fig. 1.3 and they are described as:

- $-Q^2$ is the square of the four momentum transfer to the virtual photon which is the square of the difference between the four momenta of incident and scattered electron. Q^2 sets the resolution scale of the probing interaction ($\lambda \approx \hbar c/Q$).

- W^2 is the square of the hadronic invariant mass, which is equal to the square of the sum of four momenta of target proton and virtual photon. Note $(p_\gamma + p_p)^2 = (p_\pi + p_n)^2$.

- t is the Mandelstam variable which indicates the square of the difference between four momenta of the virtual photon and final pion. Note $(p_\gamma - p_\pi)^2 = (p_p - p_n)^2$. t sets the impact parameter of the interaction ($b \approx \hbar c/\sqrt{-t}$).
- ϕ_π is the azimuthal angle between the scattering and reaction planes.

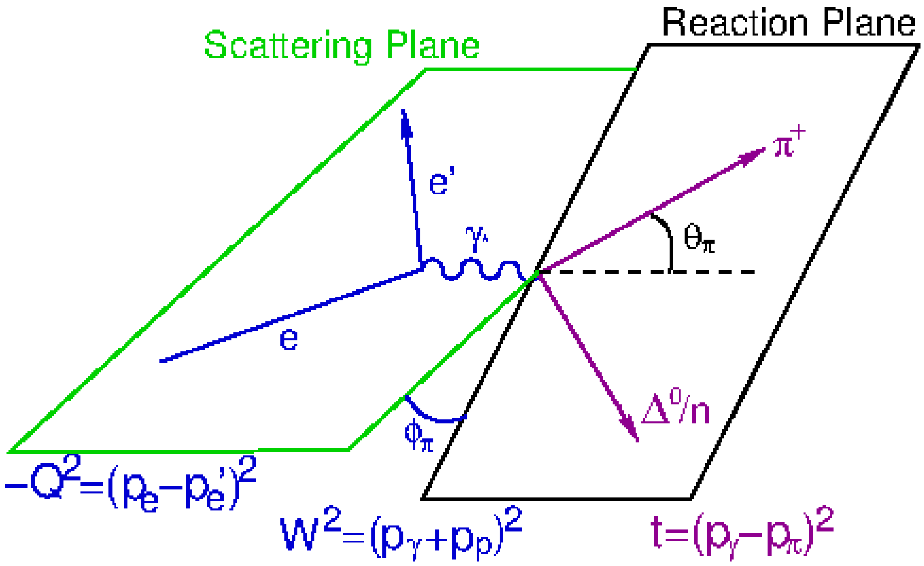

Figure 1.3: Different planes for Exclusive Pion Electroproduction reaction. The indicated momenta are four vectors.

Exclusive pion electroproduction serves as a powerful tool to probe the internal structure of hadrons and gain insight into the fundamental properties of QCD. This reaction has been studied at low Q^2 in a number of previous experimental studies including Brauel et al. and Jefferson Lab 6 GeV experiments [7, 8, 9]. Since this reaction is fully exclusive, it provides access to key non-perturbative features of the nucleon, allowing for a deeper understanding of how quarks and gluons contribute to observable hadronic properties.

One of the central motivations for studying this reaction is its connection to GPDs (see the right panel in Fig. 1.2), which encode the three-dimensional structure (longitudinal momentum and transverse position) of hadrons. Unlike inclusive DIS, where only one-dimensional PDFs are accessible, exclusive processes such as pion electroproduction allow for a more comprehensive picture of quark and gluon dynamics. In particular, the measurement of different polarization observables and cross-sections in pion electroproduction provides constraints on chiral-odd (transversity) GPDs (details in Section 1.3.2), which remain less well understood than their chiral-even counterparts. The extraction of these distributions is crucial for understanding the role of orbital angular momentum in nucleon structure, a major open question in hadron physics.

Additionally, exclusive pion electroproduction is sensitive to the interplay between perturbative and non-perturbative QCD dynamics. At low momentum transfer, the reaction is governed by hadronic degrees of freedom, where meson cloud effects and chiral symmetry breaking play dominant roles. At higher energies and momentum transfers, factorization theorems in QCD [10] suggest that the reaction becomes increasingly sensitive to the underlying quark-gluon structure, offering a way to study the transition between the non-perturbative and perturbative regimes. Investigating this transition is essential for testing QCD predictions and improving phenomenological models of hadron structure.

Another motivation for studying this reaction is the role of Regge theory and the exchange of mesons in the t-channel [11]. A t-channel process in exclusive pion electroproduction refers to a reaction mechanism where the virtual photon interacts with the target nucleon by exchanging a meson (e.g., a pion or a Reggeon), transferring momentum t and leading to the production of a pion in the final state. In this process, the pion pole contribution decreases as function of $-t$ (as shown in the Born term model $t/(t-m_\pi^2)$ [12]). At lower momentum transfer, pion electroproduction is influenced by the exchange of Reggeized mesons, such as the ρ and a_2 trajectories. Understanding these exchanges helps clarify how QCD manifests at different distance scales and provides an avenue for testing models of meson-baryon interactions.

This thesis focuses on the study of exclusive pion electroproduction over a wide range of kinematics, covering different energy and momentum transfer regions. By systematically varying the kinematic variables, such as the photon virtuality Q^2, the invariant mass of the final state W, and the momentum transfer t, it is possible to explore different aspects of hadron structure.

At lower Q^2, the reaction is dominated by hadronic degrees of freedom, providing insights into pion-nucleon interactions and meson exchange dynamics. At intermediate Q^2, the interplay between hadronic and partonic descriptions becomes evident, allowing for studies of QCD factorization and the role of GPDs. At higher Q^2, the reaction is expected to be governed by partonic sub-processes, where the scattering occurs at the quark level, making it possible to extract fundamental QCD observables such as the pion's parton distributions.

By analyzing data at a wide range of kinematics, this study aims to bridge the gap between the non-perturbative and perturbative descriptions of QCD, providing new constraints on hadron structure models. The results will contribute to ongoing efforts to refine theoretical frameworks, improve our understanding of QCD at intermediate energies, and guide future experiments at facilities such as JLab and the upcoming EIC.

1.2.2 Cross-Section

The cross-section of the exclusive pion electroproduction reaction is a fundamental experimental observable that provides direct access to the internal structure of hadrons. In particular, precise cross-section measurements enable the extraction of PDFs and GPDs from data, which are essential to understanding the spatial and momentum structure of quarks and gluons within nucleons. The separation of different components of the cross-section allows for the disentanglement of various underlying reaction mechanisms, leading to a more complete picture of hadron structure in the framework of QCD.

Since exclusive pion electroproduction involves a virtual photon exchanged between the electron and the target nucleon, the cross-section depends on the polarization states of the virtual photon. The differential cross-section for the reaction can be decomposed into multiple components as follows [13]:

$$\begin{aligned} 2\pi \frac{d^2\sigma}{dt d\phi} &= \epsilon \frac{d\sigma_L}{dt} + \frac{d\sigma_T}{dt} + \sqrt{2\epsilon(1+\epsilon)} \frac{d\sigma_{LT}}{dt} \cos\phi \\ &+ \epsilon \frac{d\sigma_{TT}}{dt} \cos 2\phi + h \cdot \sqrt{2\epsilon(1-\epsilon)} \frac{d\sigma_{LT'}}{dt} \sin\phi \end{aligned} \quad (1.3)$$

where

- σ_L is the longitudinal cross-section, which arises from interactions mediated by a longitudinally polarized virtual photon.

- σ_T is the transverse cross-section, corresponding to interactions with a transversely polarized virtual photon.

- σ_{LT} and σ_{TT} are interference terms that arise due to the coupling between longitudinal and transverse virtual photon contributions. Note, the transverse polarization can be in two directions whereas longitudinal polarization can be in one direction only.

- $\sigma_{LT'}$ is the polarized cross-section term, which depends on the helicity of the electron beam and is sensitive to spin-dependent interactions.

- ϕ is the azimuthal angle (same as ϕ_π in Fig. 1.3).

- h is the helicity of the electron beam. Mathematically $h = \vec{s} \cdot \vec{p}/|\vec{s}||\vec{p}|$, where $\vec{s}$ is the spin vector, $\vec{p}$ is the momentum vector.

- ϵ is the polarization of the virtual photon, which is given as the ratio of flux of longitudinal and transversely polarized virtual photons. In the lab frame:

$$\epsilon = \left[1 + 2\frac{(E_e - E_{e'})^2 + Q^2}{Q^2} \tan^2 \frac{\theta_{e'}}{2}\right]^{-1} \tag{1.4}$$

where

- E_e is the initial electron beam energy.

- $E_{e'}$ is the scattered electron energy.

- Q^2 is the four-momentum transfer squared.

- $\theta_{e'}$ is the electron scattering angle.

The five-fold differential cross-section is:

$$\frac{d^5\sigma}{dQ^2\ dW\ d\phi_e\ d\Omega_\pi^*} = \Gamma_\nu(Q^2,\ W) \cdot \frac{d^2\sigma}{d\Omega_\pi^*}, \tag{1.5}$$

where $d\Omega_\pi^* = dsin\theta_\pi \cdot d\phi_\pi$ is the pion solid angle in the γp center of mass frame and Γ_ν is the photon flux and can be written, in Hand convention [14], as follows:

$$\Gamma_{\nu} = \frac{\alpha}{2\pi^2}\frac{E_{e'}}{E_e}\frac{q_L}{Q^2}\frac{1}{1-\epsilon} \tag{1.6}$$

where α is the fine structure constant and $q_L = (W^2 - M_p^2)/2M_p$ is the equivalent real-photon energy. The two-fold differential cross-section can be transported to the Lorentz-invariant cross-section (in Eq. 1.3) as follows:

$$\frac{d^2\sigma}{d\Omega_{\pi}^*} = \frac{d^2\sigma}{dtd\phi}\cdot\frac{dt}{dcos\theta^*} \tag{1.7}$$

where $dt/dcos\theta^* = 2\,|p_{\pi}^*|\,|q^*|$ is a Jacobian factor and p_{π}^* and q^* are the three momenta in the center-of-mass frame of the pion and the photon respectively.

A precise determination of the different cross-section components requires specialized experimental techniques. The t-dependence of the cross-section is sensitive to the reaction mechanism, whereas the Q^2 dependence of the cross-section can validate the hard-soft factorization. The Rosenbluth separation method [9] enables the separation of unpolarized cross-section terms by performing measurements at fixed values of Q^2 and W, while varying ϵ. This method necessitates multiple beam energy settings to systematically control ϵ and extract the longitudinal and transverse contributions.

For the polarized cross-section $\sigma_{LT'}$, an alternative approach is used. The measurement of the beam spin asymmetry (BSA), which arises when using a longitudinally polarized electron beam incident on an unpolarized target, provides access to $\sigma_{LT'}$.

This term is particularly important in probing spin-dependent effects in pion electroproduction and is a key focus of this thesis. Specifically, this work investigates the polarized cross-section for the exclusive $p(e, e^{'}\pi^{+})\Delta^{0}$ reaction over a wide kinematic range, providing insights into the spin structure of the nucleon and its excited states.

Beyond the standard pion electroproduction reactions on protons, the transition from a nucleon to a Δ^{0} final state introduces an additional layer of complexity. This process is governed by transition GPDs, which extend the traditional GPD framework to nucleon-to-resonance transitions. These transition GPDs encode the spatial and momentum distribution of partons while incorporating the spin and isospin structure of excited baryonic states.

1.3 QCD Factorization

Factorization in QCD is a fundamental concept that allows the separation of short-distance (hard) and long-distance (soft) physics in high-energy scattering processes [15]. It provides a systematic framework for describing exclusive reactions, such as pion electroproduction, in terms of perturbatively calculable hard scattering amplitudes and non-perturbative hadronic structure functions.

Factorization is essential because it enables the interpretation of experimental data in terms of underlying quark and gluon dynamics, allowing for direct comparisons between theoretical predictions and measurements. The hard-soft separation is particularly crucial in exclusive processes, where the interaction involves a highly virtual photon that probes the short-distance structure of the nucleon while simultaneously generating a final-state meson through long-distance hadronization.

Mathematically, factorization expresses the amplitude of the exclusive reaction as a convolution of a hard scattering kernel and a non-perturbative hadronic matrix element:

$$M = H \otimes\ F, \tag{1.8}$$

where H represents the hard scattering coefficient, which can be calculated in perturbative QCD, and F is the soft, non-perturbative function describing hadron structure, such as a GPD or a distribution amplitude [16].

1.3.1 Regge-Based Approach to Factorization

One of the earliest approaches to understanding factorization in exclusive reactions is based on Regge theory. Regge theory describes high-energy hadronic interactions in terms of the exchange of families of particles, known as Regge trajectories, which have similar baryon numbers but different masses and spin [17].

In the context of exclusive pion electroproduction, Regge-based models provide a framework to describe the reaction at moderate energies where the exchanged virtual photon interacts via meson exchange mechanisms. The amplitude for pion production can be expressed as a sum over Reggeon exchanges (the exchange of entire Regge trajectories instead of a single particle), with the dominant contributions coming from vector mesons such as the ρ and ω, as well as pseudoscalar mesons like the pion [18].

A typical Regge-based model [11] for the pion electroproduction amplitude is written as:

$$M_{Regge} \propto \sum_i C_i \left(\frac{s}{s_0}\right)^{\alpha_i(t)} e^{i\pi\alpha_i(t)}, \tag{1.9}$$

where:

- s is the squared center-of-mass energy,
- t is the squared momentum transfer,
- $\alpha_i(t)$ represents the Regge trajectory for the exchanged particle i,
- C_i are coupling constants,
- s_0 is a normalization scale.

Regge-based models successfully describe certain features of pion electroproduction at lower energies, particularly in the forward kinematic region where meson exchange dominates. However, they do not incorporate explicit quark and gluon degrees of freedom, limiting their applicability at higher energies where a more fundamental QCD-based approach is needed [19].

1.3.2 Generalized Parton Distributions

Generalized Parton Distributions provide a rigorous framework for factorization in exclusive reactions. Unlike traditional PDFs, GPDs contain information about both the longitudinal momentum and transverse spatial distributions of quarks and gluons within nucleons [20]. They offer a unified picture of hadron structure, linking inclusive deep inelastic scattering (DIS), form factors, and exclusive reactions.

In the context of exclusive pion electroproduction, the scattering amplitude factorizes into a hard sub-process, calculable in perturbative QCD, and a GPD describing the nucleon's non-perturbative structure. The leading-order amplitude [20] for deeply virtual pion electroproduction is given by:

$$M \sim \sum_q e_q H^q_{\pi N} \otimes E_q, \tag{1.10}$$

where $H^q_{\pi N}$ represents the quark-helicity conserving GPDs, and E_q accounts for helicity-flip contributions. These distributions encode critical information on hadron structure, including quark angular momentum contributions to the nucleon spin [21]. There are two main types of GPDs:

Chiral-even GPDs (Leading-Twist)

These GPDs conserve the helicity (spin projection) of the quarks and are accessible in deeply virtual exclusive reactions like Deeply Virtual Compton Scattering (DVCS) and Deep Exclusive Meson Production (DEMP):

- **H(x, ξ, t)**: Describes how the momentum and spatial distribution of quarks change when the nucleon remains in the same spin state.
- **E(x, ξ, t)**: Describes how the spatial distribution changes when the nucleon undergoes a spin flip. It is related to the orbital motion of quarks inside the nucleon.
- $\tilde{H}(x, \xi, t)$: Represents the quark's helicity distribution when the nucleon does not change its spin.
- $\tilde{E}(x, \xi, t)$: Represents the helicity distribution when the nucleon undergoes a spin flip and is important for understanding spin-orbit correlations.

Chiral-odd (Transversity) GPDs

These GPDs describe how the nucleon's internal structure changes when quarks undergo a helicity flip, making them sensitive to the transverse polarization of quarks. These distributions are more challenging to access experimentally:

- $H_T(x, \xi, t)$: The transversity counterpart of $H(x, \xi, t)$, describing the transverse polarization distribution of quarks.
- $E_T(x, \xi, t)$: The transversity counterpart of $E(x, \xi, t)$, related to orbital angular momentum effects for transversely polarized quarks.

- $\tilde{H}_T(x, \xi, t)$: Describes helicity-flip effects with a connection to the chiral-even $\tilde{H}(x, \xi, t)$.

- $\tilde{E}_T(x, \xi, t)$: Related to nucleon spin-flip effects in transversity interactions.

Studying these GPDs experimentally helps us visualize the nucleon's internal structure in three dimensions and test fundamental aspects of QCD.

1.3.3 Transition GPDs

GPDs have also been extended to describe the transition between a nucleon and an excited baryonic state, such as the Δ resonance. These are referred to as Transition Generalized Parton Distributions. These distributions encode the spatial and momentum structure of quarks in excited hadronic states. They help bridge the gap between ground-state nucleon structure and resonance excitations, offering a complementary view of the non-perturbative regime of QCD. Since the Δ baryon is the lowest-lying nucleon excitation, studying this reaction through transition GPDs provides crucial information on the mechanisms governing baryon excitations and their role in hadron structure.

Experimental studies of the $N \to \Delta$ transition via pion electroproduction offer a way to constrain theory predictions. These measurements help determine the spatial distribution of partons in excited states and provide insight into the transition form factors that characterize the $N \to \Delta$ interaction. Moreover, transition GPDs play an essential role in understanding the interplay between chiral symmetry breaking and confinement in QCD, as they provide a direct link between hadron structure and non-perturbative QCD dynamics.

A comprehensive study of transition GPDs requires precise cross-section measurements for the ground state nucleon as well as resonances. A cross-section ratio from the two reactions can provide invaluable information to minimize the large theoretical uncertainty for transition GPDs [22]. The measurements performed at different kinematics can allow study of reaction mechanism as well as the extraction of transition amplitudes and their dependence on momentum transfer. These studies complement traditional GPD analyses and deepen our understanding of hadronic structure beyond the ground-state nucleon.

This thesis is the first ever measurement of the $p(e, e^{'}\pi^{+})\Delta^{0}$ reaction. By studying the $p(e, e^{'}\pi^{+})\Delta^{0}$ reaction, this thesis aims to explore the role of transition GPDs in nucleon resonance formation and the partonic structure of the Δ^{0}. These studies complement traditional GPD extractions from ground state reactions and contribute to a deeper understanding of hadron structure in QCD. The results obtained in this work will provide new constraints on transition GPDs and enhance our understanding of the non-perturbative regime of QCD.

The polarized structure function $\sigma_{LT'}$ is related to the convolutions of tensor and helicity non-flip transition GPDs with sub-process amplitudes, as expressed in:

$$\sigma_{LT'} \sim \sqrt{-t'} \ \ \mathrm{Im}\left[G^3_{T_5} \cdot A + c\, G^3_{T_7} \cdot A'\right], \tag{1.11}$$

where A and A' are helicity amplitudes, and c is an unknown kinematic factor. The tensor transition GPDs $G^3_{T_5}$ and $G^3_{T_7}$ can be related to the ground state tensor GPD H_T in the large N_c limit, making them sensitive to the tensor charge of the resonance [23].

1.3.4 Previous Experiments

The CLAS collaboration measured beam spin asymmetries in deep exclusive electroproduction ($\gamma^* N \to \pi^- \Delta^{++}$) using longitudinally polarized electrons on an unpolarized hydrogen target in the CLAS12 detector [24], published in 2023 [23]. This reaction was fully exclusive with all final state particles detected. A cut on $M(\pi^+\pi^-) > 1.1$ GeV is applied to reject the dominant background from $\gamma^*\ p\ \to\ p\ \rho^0\ \to\ p\ \pi^+\ \pi^-$ and other multi-pion production processes.

The Δ^{++} peak in the $p\pi^+$ invariant mass was selected, with good background control (as shown in [23]), and beam-spin asymmetries were determined for various Q^2, x_B, and $-t$ bins. The extracted $\sigma_{LT'}/\sigma_0$ ratio for $\pi^-\Delta^{++}$ was compared with results from $\gamma^* N \to \pi^+ n$ [25] and $\gamma^* N \to \pi^0 p$ [26] electro-production, as shown in Fig. 1.4. The results indicate that the $\pi^-\Delta^{++}$ cross-section ratio $\sigma_{LT'}/\sigma_0$ has the opposite sign and approximately twice the magnitude compared to $\pi^+ n$. This

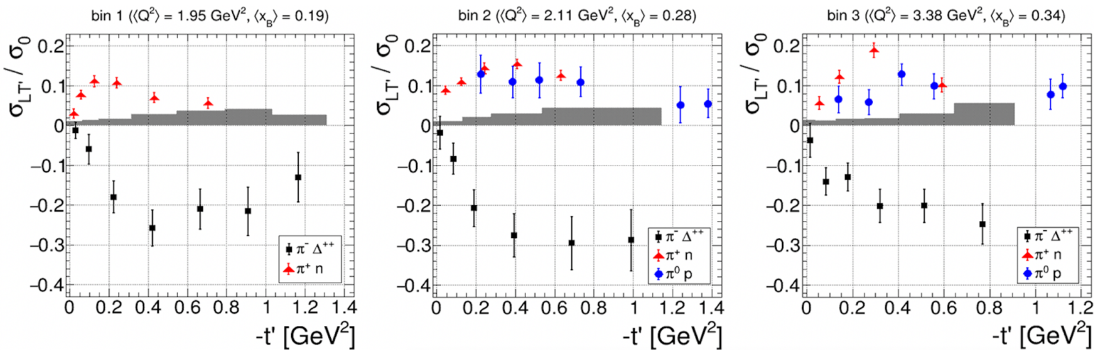

Figure 1.4: Results for $\sigma_{LT'}/\sigma_0$ for different exclusive reactions from CLAS12 [23].

difference can be explained by the interaction of the virtual photon with different quarks (u, d) for each reaction. The large magnitude of $\sigma_{LT'}/\sigma_0$ for $\pi^-\Delta^{++}$ is a clear signature of the excitation process encoded in transition GPDs [23].

1.4 This Thesis

This thesis presents the first-ever measurement of the $p(e, e'\pi^+)\Delta^0$ reaction, providing crucial insights into the role of transition GPDs in nucleon resonance formation and the partonic structure of the Δ^0. While traditional GPD extractions primarily focus on ground-state nucleon structure, this study extends the framework to nucleon-to-resonance transitions, offering a new perspective on hadron structure within the context of QCD. By analyzing the beam spin asymmetry and cross-section ratio for the $p(e, e'\pi^+)\Delta^0$ reaction, and comparing it with the well-studied $p(e, e'\pi^+)n$ reaction, this work establishes new constraints on transition GPDs models. Additionally, the results from Hall C at Jefferson Lab are compared with recent CLAS12 measurements, contributing to a more comprehensive understanding of the non-perturbative regime of QCD.

1.4.1 Experimental Coverage

This research herein leverages the high-resolution spectrometers and fixed-target experimental setup at Jefferson Lab Hall C, ensuring precise control over kinematic variables. The study focuses on the pion electroproduction reaction $p(e, e'\pi^+)\Delta^0$ at momentum transfers in the range $2.0 < Q^2 < 6.0$ GeV^2, invariant mass values of $W > 2.25$ GeV, and Mandelstam t in the region $0.15 < |t| < 1.0$ GeV^2. These kinematic conditions enable the investigation of higher resonance contributions and facilitate a detailed analysis of Δ^0 resonance in exclusive pion electroproduction. This work will study the exclusive $\pi^+\Delta^0$ reaction at wide range of kinematics and also allow a first measurement of the Q^2-dependence of the polarized cross-section ratio at fixed x_B. This will provide a new test of the rate of change of cross-section in $N \to \Delta$ transition reactions. Additionally, this work can also confirm the sign change in beam spin asymmetry and cross-section ratio due to isospin symmetry as predicted in [22] and observed in CLAS12 measurement [23].

1.4.2 Thesis Structure

The thesis is structured as follows:

- **Chapter 2** provides an overview of the experimental setup, including the Continuous Electron Beam Accelerator Facility (CEBAF) at Jefferson Lab and the 12 GeV Hall C upgrade. Key components such as the beamline, target, spectrometers, detectors, and data acquisition system are discussed.

- **Chapter 3** details the Hall C data analysis framework (hcana), outlining event reconstruction methods, experimental equipment performance, and particle identification techniques crucial for exclusive pion electroproduction analysis.

- **Chapter 4** describes the Hall C simulation package (SIMC), including event generation, spectrometer modeling, and resolution corrections. Background estimation in the Δ^0 region is also addressed.

- **Chapter 5** presents the physics results, including binning procedures, beam spin asymmetry measurements, and polarized cross-section extractions as functions of $-t$ and Q^2. Comparisons with existing Hall C and CLAS12 data are provided. Systematic uncertainty studies and potential future research directions are also discussed before concluding the thesis.

- **Appendices** provide supplementary material including final kinematic tables from the Kaon-LT experiment (updated version of tables in Section 2.7), a summary of detector calibrations (performed by other members of the collaboration) and additional figures from the background study (as discussed in Section 4.4).

Chapter 2

Experimental Setup

This chapter will delve into the experimental apparatus designed for conducting the commissioning experiments using the Continuous Electron Beam Accelerator Facility (CEBAF) at Jefferson Lab, focusing on the 12 GeV Hall C experimental setup. In the beginning, an overview of the accelerator is presented, followed by an introduction of the Hall C 12 GeV upgrade. Subsequently, the focus will shift to the discussion of key components necessary for experiments, including the beamline, target, and spectrometer systems, comprising both magnets and detector systems. Additionally, attention will be given to the configuration of the data acquisition system used for data collection. In the end, an outline of the Kaon-LT experiment will be provided.

2.1 Jefferson Lab

The discovery of quarks within the proton through a sequence of electron-proton scattering experiments conducted at the Stanford Linear Accelerator (SLAC) in the late 1960s, coupled with the emergence of a novel theory of strong interactions known as Quantum Chromodynamics in the early 1970s, spurred a myriad of inquiries surrounding the influence of quarks in nuclear forces [27, 28].

In 1994, a significant milestone was achieved as the first beam successfully reached experimental Hall C, marking the commencement of operations at the Continuous Electron Beam Accelerator Facility (CEBAF). The subsequent year witnessed CEBAF attaining its design energy of 4 GeV. Notably, by June 1998, a pivotal achievement occurred with the successful simultaneous delivery of the beam to all three experimental halls. Although initially designed to operate at 4 GeV, ongoing research and development efforts on Superconducting Radio Frequency (SRF) technology at Jefferson Lab allowed to exceed the original expectation, and the accelerator reached beam energies of nearly 6 GeV. This achievement was implemented from the year 2000 onward, allowed for a total beam current of up to 200 μA, combined across all experimental halls. The operational phase at 6 GeV concluded in Spring 2012 after the completion of 178 experiments in all three halls since 1994. [29, 30, 31].

The results from initial experiments at JLab significantly improved the understanding of hadron internal structure. These results motivated scientists to propose

Figure 2.1: An aerial view of Jefferson Lab showing two linear accelerators and experimental halls A, B, C in the foreground and D at the opposite end

the 12 GeV upgrade at CEBAF to enhance capabilities of the electron accelerator and all the experimental halls. The 12 GeV upgrade was approved by the US Department of Energy (DOE) in 2004. In addition to upgrades to the electron accelerator and existing experimental halls, a new experimental hall was added. After the upgrade, JLab has a total of four experimental halls, namely A, B, C and D. Fig. 2.1 shows the aerial view of the existing halls including the newest hall which is Hall D.

2.1.1 CEBAF 12 GeV Upgrade

The electron accelerator at JLab, illustrated in Fig. 2.2, is constructed based on state-of-the-art SRF technology. It stands out as one of the world's prominent particle accelerators, specifically designed for the in-depth investigation of quark structures

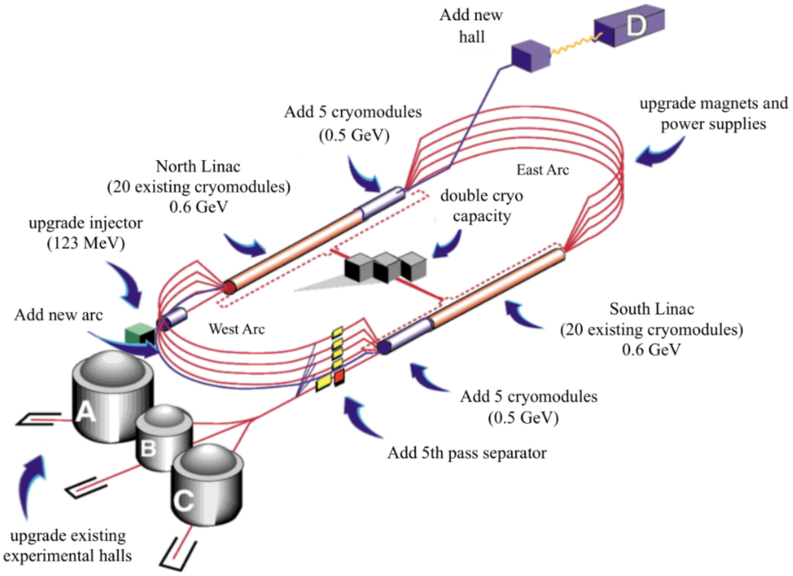

Figure 2.2: Schematic of CEBAF 12 GeV upgrade showing addition of extra cryomodules (sections of the electron accelerator composed of SRF acceleration cavities) and the newest experimental hall D [32].

within hadrons. The 12 GeV upgrade significantly improved its capabilities for advanced intermediate energy physics research.

The CEBAF accelerator uses a racetrack shaped design featuring two superconducting linear accelerators (LINACs) known as the north linac and south linac. These LINACs are interconnected by magnetic arcs situated on the east and west sides. Comprising niobium SRF cavities, each cavity possesses an active length of 50 cm and operates at a temperature of 2 K using liquid helium. These SRF cavities are organized in pairs, and four pairs are encapsulated in thermally insulated tanks referred to as cryo-modules. Both the north linac and south linac comprise 25 cryomodules each. Each cavity is energized by a 5 kilowatt (kW) klystron operating at 1497 MHz. This utilization of SRF cavities at low temperature enables continuous wave (CW) mode operation (macro structure electron beam is continuous) at JLab. The 2 arcs (east and west) consist of 5 layers of bending magnets which are stacked on top of each other. One layer for each pass the beam makes through these arcs, where Halls A, B, C can receive 1-5 pass electron beam with a maximum of up to 11 GeV beam energy (for 5 pass beam) and Hall D receives 5.5 pass beam which can reach a maximum beam energy up to 12 GeV. The gradient energy of the linacs is variable and can be tuned based on the requirements of the experiments.

The injector is positioned at the initiation of the north linac, comprising circularly polarized lasers along with 18 SRF cavities, equivalent to 2.25 cryo-modules. In this section, the beam undergoes an initial acceleration to 45 MeV before being injected into the north linac. Subsequently, the beam undergoes incremental accelerations of maximum of 2.2 GeV with each pass. The beam switch-yard (BSY), located at the termination of the west arc - south linac section, incorporates extraction and recombination magnets. Functioning at the conclusion of the acceleration process, the BSY is designed to extract and direct the beam to any of the 3 experimental Halls (A, B, or C) during any integral pass.

The CEBAF accelerator generates beams with bunch lengths of under 2 ps, achieved through the utilization of RF power in the resonating cavities. This allows high timing resolution for Hall C experiments (like Kaon-LT experiment) using a coincidence trigger. A combination of continuous wave mode of the accelerator and coincidence trigger allows precise identification of coincidence and background events as well as high signal-to-background ratio of the experimental rates. This coincidence time is critical for event selection in all coincidence Hall C experiments. During the Kaon-LT experiment, a distinctive operational configuration was adopted, wherein every sixth pulse was directed to Hall C, resulting in a pulse delivery rate of one pulse every 4 ns, equivalent to a beam frequency of 250 MHz. This delivery rate effectively means that Hall C was sharing the beam pulse with another hall to allow beam delivery to all four halls. The CW beam is seamlessly distributed to experimental halls through the BSY [31].

2.2 Hall C

Experimental Hall C at Jefferson Lab serves as a dedicated fixed-target, high-precision facility for probing hadron structure. Figure 2.3 provides an overview of Hall C, featuring the integration of the newly built Super High Momentum Spectrometer (SHMS) alongside the legacy High Momentum Spectrometer (HMS) from the 6 GeV era. The upgraded Hall C demonstrated efficient detector performance and particle identification capabilities for the newly introduced SHMS. In 2018, a group of experiments was executed to commission the advanced spectrometer and evaluate its full range of physics capabilities. These commissioning experiments, integral to the expansive 12 GeV physics program devised by the Hall C user community, delved into physics topics at kinematic regimes beyond the reach of CEBAF during the 6 GeV era.

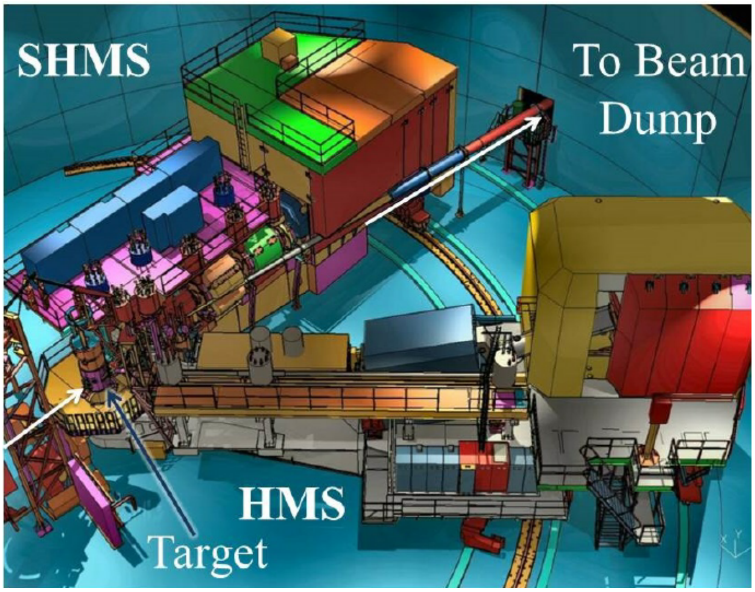

Figure 2.3: A CAD rendering of Experimental Hall C after the 12 GeV upgrade. The two spectrometers can rotate around a common pivot point using large casters on circular steel rails, as seen in the drawing [28].

2.2.1 Beamline

As the electron beam undergoes redirection toward the Hall C entrance via the BSY, a series of eight dipole magnets guide the beam within the hall arc, as shown

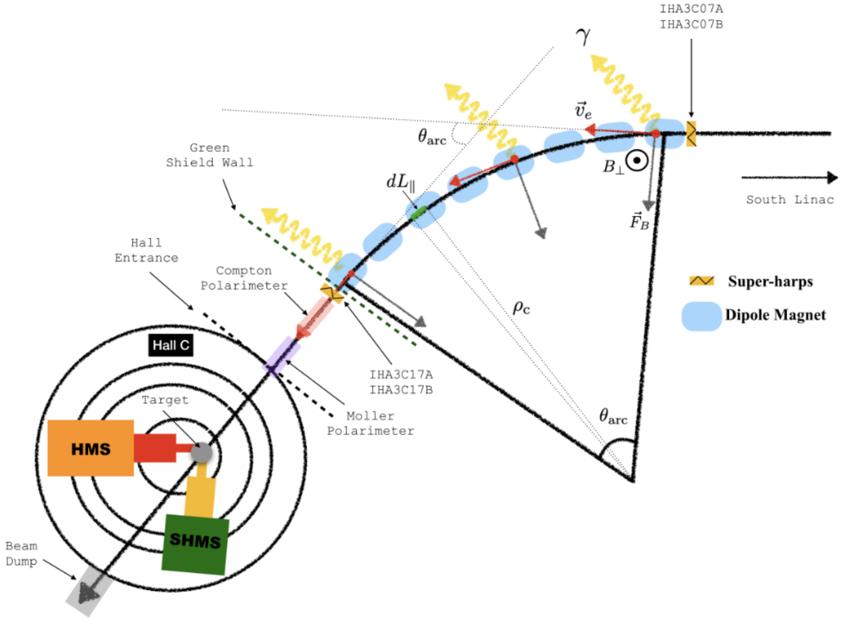

Figure 2.4: The Hall C arc showing super harps, dipole magnet and other relevant beamline components [34].

in Figure 2.4. A variety of different equipment, such as the Compton and Moller Polarimeters, are situated in this specific region [33].

Continuing its trajectory, the beam enters into the target chamber within Hall C, culminating at the beam dump situated at the terminal end of the hall. The beamline infrastructure in Hall C is equipped with essential components designed to monitor and manage the beam throughout its transit. These components consist of super harps (wire scanners), beam current monitors (BCMs), beam position monitors (BPMs), and beam rastering systems. Each of these elements plays a distinct yet

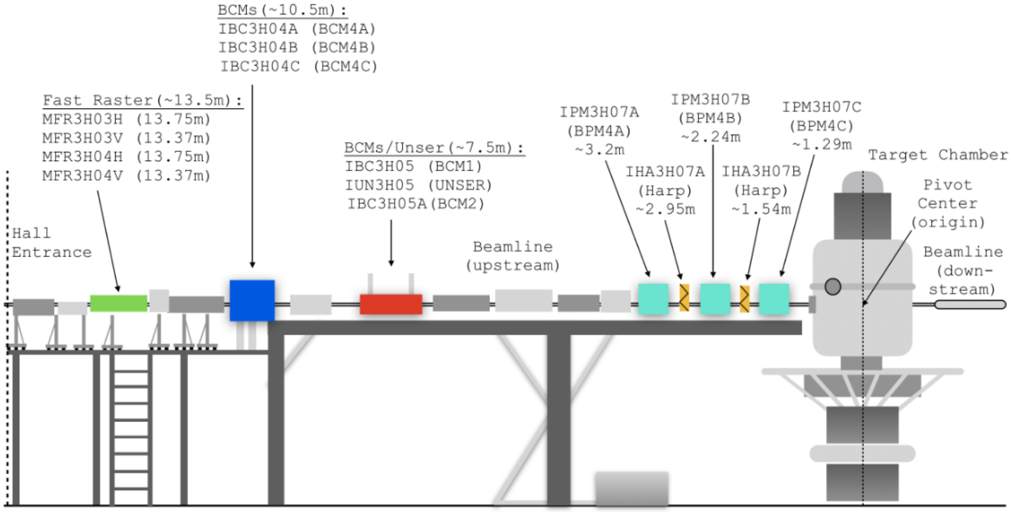

Figure 2.5: Hall C beamline showing elements upstream of the target chamber (from Hall C entrance to target chamber) [28].

interrelated role, ensuring the precise control, monitoring, and assessment of the electron beam as it navigates through the experimental setup within Hall C. Illustrated in Figures 2.5 and 2.6 is the spatial distribution of several key beamline components, located both upstream and downstream of the target chambers.

Upstream of the target chamber, specific components include the Fast Raster (FR), BPMs, BCMs, and super harps. Figure 2.5 provides an overview of the arrangement and location of the beamline constituents from the Hall C entrance to the target chamber. Since a large fraction of the electrons in each bunch do not interact or scatter within the target chamber, they are directed to the beam dump through downstream beamline. Figure 2.6 focuses on the beamline components extending

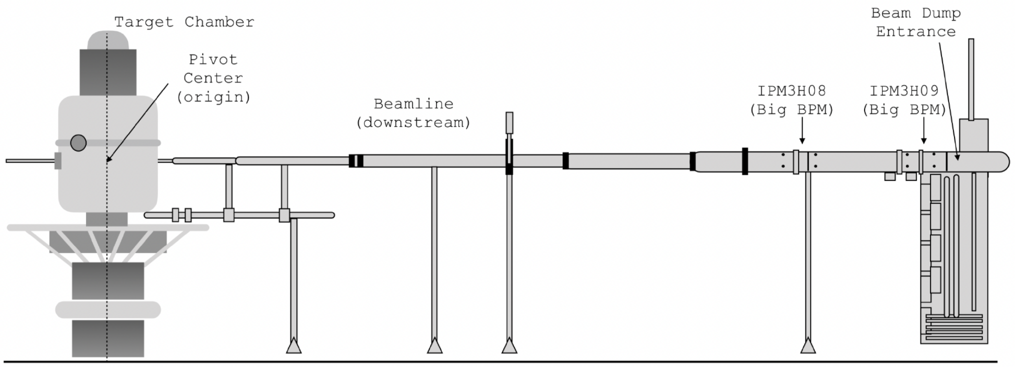

Figure 2.6: Hall C beamline showing elements downstream of the target chamber (from target chamber to beam dump) [28].

from the target chamber to the beam dump.

The spectrometers are rigidly attached to a common pivot and they can be rotated about it. The distances shown to the different beamline components are measured from the pivot center of the two spectrometers (the origin). The commonly used names are given in parentheses. The names given for FRs refer to the horizontally and vertically bending air-core magnets. The entire beam pipe downstream of the target chamber is ≈ 27.4 m long from the exit of the target chamber to the entrance of the beam dump, with two 1.5 m long removable sections of $24''$ diameter beam pipes. During the Kaon-LT experiment, a special narrow downstream beamline pipe was used to facilitate very small forward angle for the SHMS. The two big BPMs towards the beam dump are used to measure the beam position downstream of the target chamber.

2.2.2 ARC Energy Measurement

In the trajectory of the electron beam directed towards Hall C through the Hall C arc, as illustrated in Figure 2.4, a significant change in direction occurs. The Hall C arc has a single radius of curvature which allows precise measurement of beam momentum. The precise measurement of the electron beam's energy within Hall C is conducted using the magnets within the Hall C arc, effectively serving as a spectrometer [35].

During the energy measurement process, operators at the Machine Control Center implement a specific protocol. This involves the deactivation of all quadrupoles, which are focusing magnets, while exclusively employing the dipoles to steer the beam. This adjustment ensures that the electron beam adheres to the nominal central path, facilitating accurate energy measurements. The position and direction at the beginning and end of the arc's bend (34.3 °) are measured using the superharps. The beam energy can be determined from the electron momentum using the following relation:

$$p_e = \frac{e}{\theta_{arc}} \int BdI, \tag{2.12}$$

where

- e is the electron charge.

- θ_{arc} is the arc bend angle (determined to be 34.3° from the survey).

- B is the magnetic field in the dispersive elements.

- The field integral $\int BdI$ is determined by mapping the magnetic fields of the arc dipoles at the corresponding dipole current.

A precise measurement of beam energy is critical for every experiment in Hall C. During the Kaon-LT experiment, the central momentum of each spectrometer as

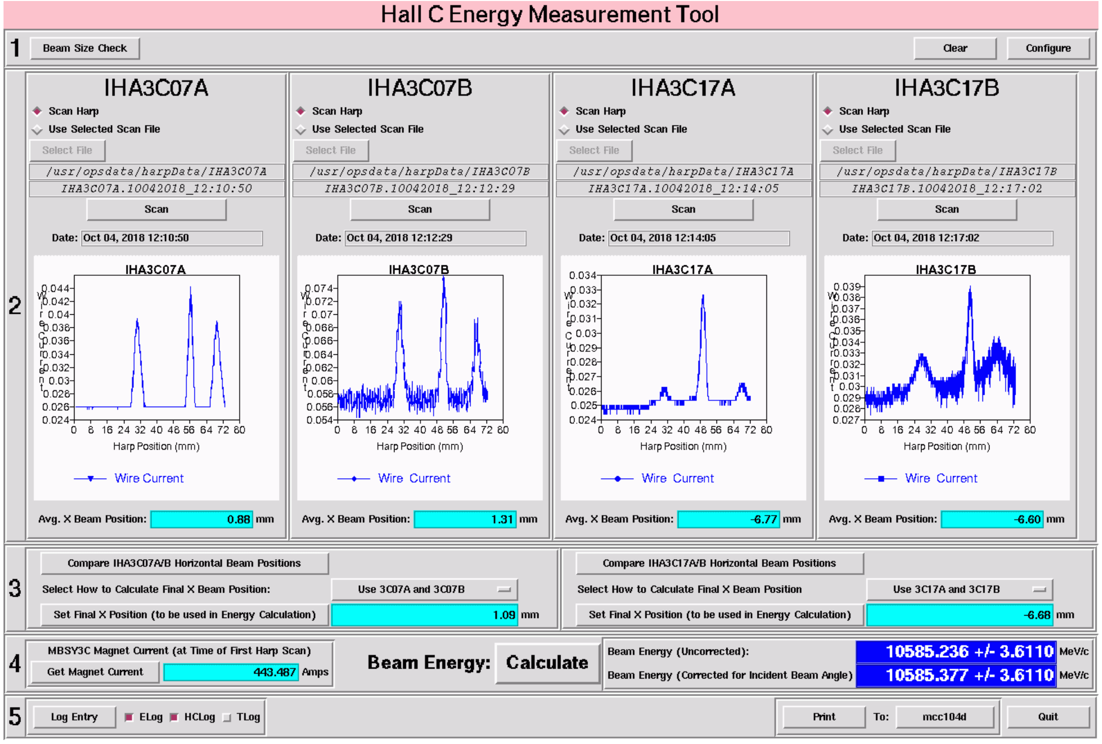

/usr/opsdata/harpData/IHA3C07A
IHA3C07A.10042018_12:10:50
Date: Oct 04, 2018 12:10:50
Avg. X Beam Position: 0.88 mm

/usr/opsdata/harpData/IHA3C07B
IHA3C07B.10042018_12:12:29
Date: Oct 04, 2018 12:12:29
Avg. X Beam Position: 1.31 mm

/usr/opsdata/harpData/IHA3C17A
IHA3C17A.10042018_12:14:05
Date: Oct 04, 2018 12:14:05
Avg. X Beam Position: -6.77 mm

/usr/opsdata/harpData/IHA3C17B
IHA3C17B.10042018_12:17:02
Date: Oct 04, 2018 12:17:02
Avg. X Beam Position: -6.60 mm

Select How to Calculate Final X Beam Position: Use 3C07A and 3C07B
Set Final X Position (to be used in Energy Calculation) 1.09 mm

Select How to Calculate Final X Beam Position Use 3C17A and 3C17B
Set Final X Position (to be used in Energy Calculation) -6.68 mm

MBSY3C Magnet Current (at Time of First Harp Scan) 443.487 Amps

Beam Energy (Uncorrected): 10585.236 +/- 3.6110 MeV/c
Beam Energy (Corrected for Incident Beam Angle) 10585.377 +/- 3.6110 MeV/c

☒ ELog ☒ HCLog ☐ TLog
To: mcc104d

Figure 2.7: An arc energy measurement taken during the Autumn 2018 run period of the Kaon-LT experiment. The different plots show beam position from BPMs and corrected beam energy value and uncertainity is used as incident beam energy.

well as kinematic quantities (such as Q^2, W and ϵ) were precisely calculated using the electron beam energy. Figure 2.7 show one of the beam energy measurement during the Kaon-LT experiment and Table 2.1 lists all the measured values during the different data taking periods. At higher energies, synchrotron radiation result in beam energy being slightly lower at the target.

Kaon-LT Run Period	Measured Beam Energy
Autumn 2018	10585.4 ± 3.6 MeV
Winter 2018	3834.8 ± 2.4 MeV
	4932.1 ± 2.6 MeV
Spring 2019	8208.8 ± 3.5 MeV
	6190.1 ± 3.0 MeV

Table 2.1: Different beam energy measurements for each run period of Kaon-LT experiment.

2.2.3 BPM

Figure 2.5 shows the placement of three Beam Position Monitors upstream of the target within Hall C, used for accurately measuring the beam position. After reaching the BPM cavities, the electron beam induces signals. The amplitude of these signals is inversely proportional to the distance between the beam and each antenna. The

BPMs, shown in Figure 2.8, are cylindrical cavity resonators featuring two pairs of antennae, allowing horizontal and vertical position measurements. These antennae accurately capture the $\approx$ 250 MHz structure of the beam, facilitating precise and real-time monitoring of the beam position both in Hall C and within the broader accelerator setup.

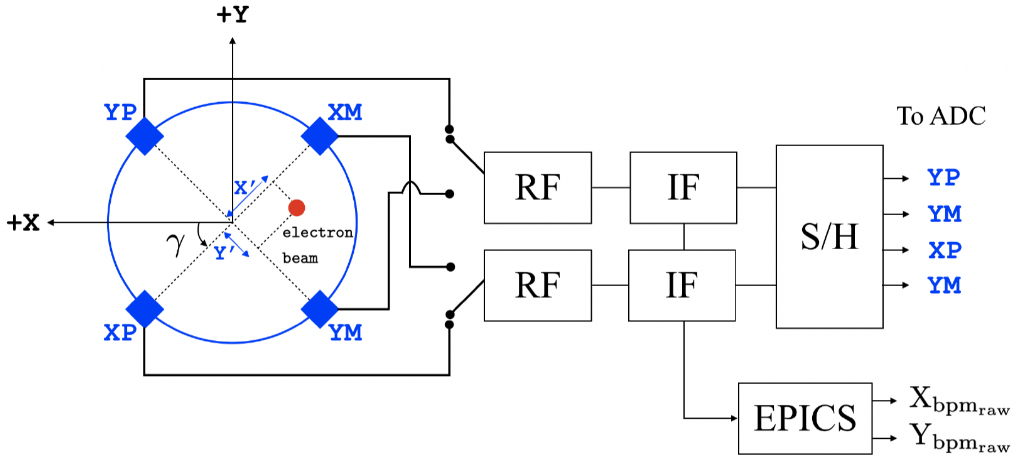

Figure 2.8: The schematic view of Beam Position Monitors in Hall C [28].

Using the standard difference over the sum method (the difference over the sum of the paired signals is converted into a position independent of current), these antennae signals are interpreted by the Experimental Physics and Industrial Control System (EPICS) readout chain to determine the raw beam positions. By using the Hall C Analysis Software (HCANA) system, the raw BPM positions are retrieved from EPICS and calibrated relative to the absolute beam position determined from the harp scans.

2.2.4 BCM

An accurate measurement of the beam charge is critical for cross-section measurements, as the data yield is normalized by the total incident charge on the target. The Beam Current Monitors play a pivotal role in this process, measuring the current of the electron beam as it travels through the beamline en route to the target. Multiple BCMs are installed for continuous monitoring of the beam current directed to Hall C. The primary instruments for this purpose include two BCMs and an adjacent Unser monitor (BCM1, BCM2, Unser) which are positioned approximately 7.5 m upstream of the target chamber. An additional set of three supplementary Beam Current Monitors (BCMs), denoted as BCM4A, BCM4B, and BCM4C, are positioned approximately 10.5 meters upstream of the target chamber. These supplementary BCMs operate concurrently with the standard pair (BCM1 and BCM2) to provide a comprehensive measurement of the beam current [36, 37, 38].

Each BCM comprises a cylindrical-shaped wave-guide, serving as a resonant cavity precisely tuned to the frequency of the electron beam. The geometric design of these cavities allows them to resonate with the TEM_{010} (Transverse Electromagnetic) mode of the electron beam pulse frequency. Here, TEM refers to the mode of propagation where electric and magnetic field lines are constrained to directions normal or transverse to the direction of propagation. The subscript 010 corresponds to the resonating mode of the electromagnetic wave generated within the superconducting

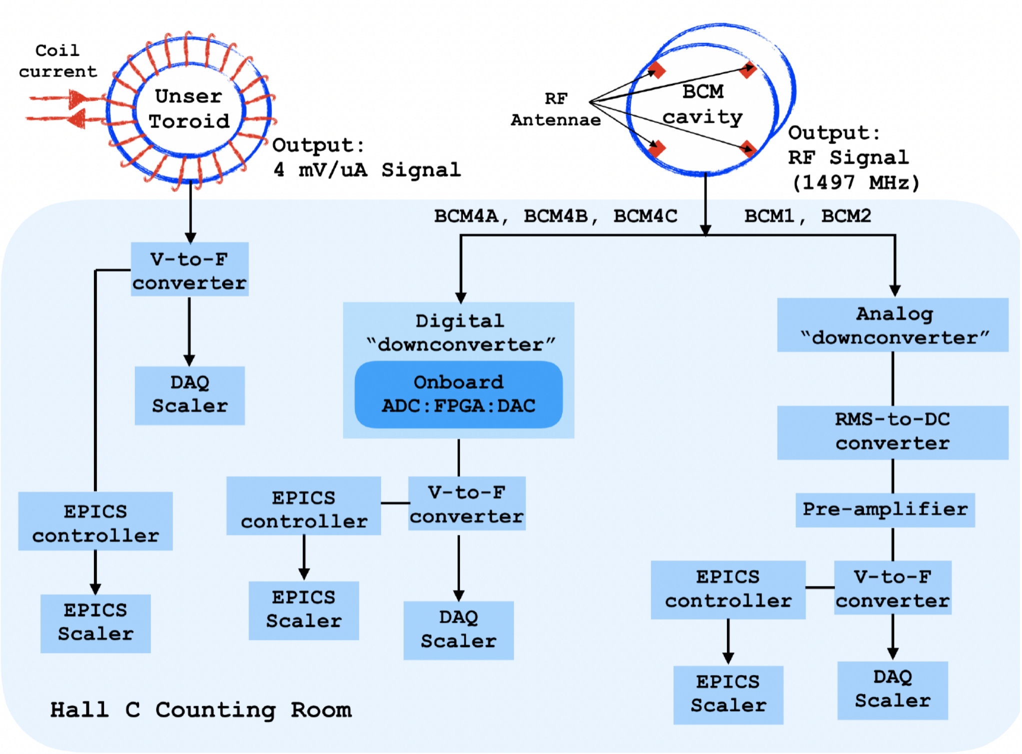

Figure 2.9: A schematic of the Hall C BCM and Unser electronics [28].

cavity. BCM1 and BCM2 share identical geometries and readout electronics. They use a down converter in tandem with a high precision Root Mean Square (RMS) to Direct Current (DC) converter [39].

BCMs exhibit reasonable gain stability over time, but require periodic calibration, which is done by using the Unser current monitoring device. The Unser monitor, shaped like a toroidal parametric DC current transformer, exhibits stable gain but experiences small drifts in offset over short time scales, rendering it unsuitable for run-to-run beam current measurements. In contrast, BCMs have a stable offset but less stable gain, necessitating calibration relative to the absolute beam current determined by the Unser. Calibration involves taking dedicated runs with periods of no beam to zero the Unser interspersed with beam periods at various currents (typically ranging from 10 μA to 70 μA in 10 μA steps). The gain of BCMs is then determined by comparing them to the Unser monitor. Calibration uncertainties are maintained below 0.5%, and the absolute uncertainty for charge measurements is considered approximately 1% [33].

Figure 2.9 depicts the Unser and BCM electronics in Hall C. The Unser's 4 mV/μA output signal is processed through a voltage-to-frequency (V-to-F) converter before being read out by a scaler. BCM1 and BCM2 use an analogue down-converter, which is then fed to an RMS-to-DC converter, amplified, and sent to the V-to-F converter before being recorded by the scaler. Similarly, in BCM4A, BCM4B, and BCM4C, RF signals undergo digital down-conversion and produce an analog signal using an on-board Digital-to-Analog Converter (DAC). This analog signal is sent to a V-to-F converter and, subsequently, to the scalers. A more detailed explanation of the electronics can be found in [28, 38] for further reference.

2.2.5 Raster

Situated approximately 13.5 m upstream of the target chamber near the Hall C entrance, a pair of fast raster magnets is permanently integrated into the Hall C beamline. These magnets consist of fast air-core dipoles positioned to enable horizontal or vertical beam steering. Employing 2×2 mm^2 square rasters, the raster plays an important role in achieving acceptable beam currents without jeopardizing the integrity of the target. Furthermore, it serves to mitigate the impact of localized boiling in the case of liquid targets. By using rastered beam (as shown in figure 2.10), the heating effects of the beam can be distributed over a larger target area, preventing the melting of solid targets and reducing the current dependence of cryogenic targets. During the Kaon-LT experiment, dedicated datasets were collected for both solid and cryogenic targets to assess the density dependence of cryogenic targets with varying beam current. This is discussed in detail in Section 3.7.

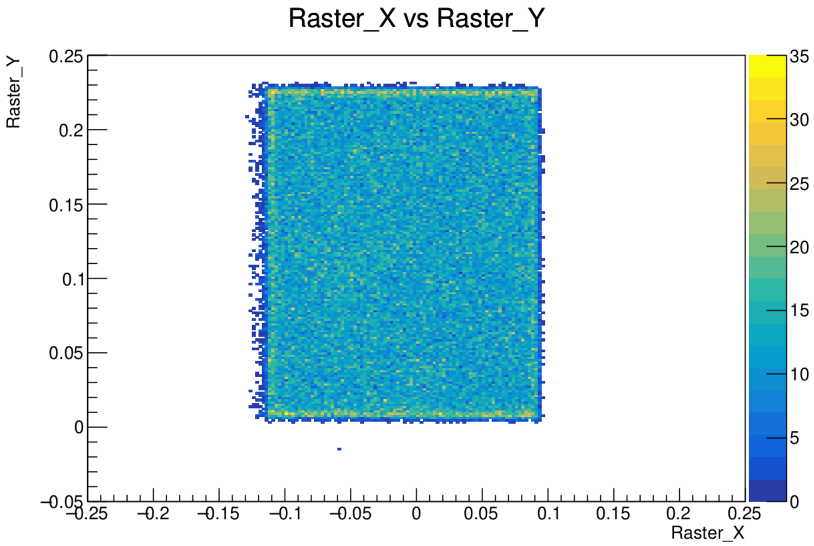

Figure 2.10: Hall C fast raster distribution from Kaon-LT Experiment. The color scale corresponds to counts.

2.2.6 Beam Polarization

The electron beam delivered to experimental Hall C is spin polarized. There were no dedicated beam polarization measurements during the Kaon-LT experiment. The polarization was instead measured via a Mott polarimeter at the injector to the accelerator (90±1%). The accelerator was tuned to deliver optimal beam polarization to Hall B and a calculation of the spin precession through the accelerator showed that Hall C received 99% of the source polarization during the first run period of the Kaon-LT experiment. These gave a result of $89^{+1}_{-3}\%$ longitudinal beam polarization to Hall C. An independent measurement of beam polarization in experimental Hall B during the same run period gave comparable results. The uncertainty in the beam polarization is calculated from the beam energy uncertainty and the LINAC gradient energy imbalance [40].

2.2.7 Coordinate System

There are different types of coordinate systems used in Hall C (as shown in 2.11).

- The **accelerator coordinate system** is a left handed coordinate system where the positive x-axis is pointed towards the right, the positive y-axis is pointed upwards to the ceiling and the positive z-axis is pointed forward to the target along the beamline.

- The **Hall C coordinate system** is right handed and it is a modified form of the accelerator coordinate system. The positive z-axis still points along the beamline in the forward direction to the beam dump. The positive x-axis points to the left and the positive y-axis points upwards to the ceiling.

- There is a **spectrometer coordinate system** for each spectrometer. This is right handed coordinate system with origin at the center of focal plane which is an imaginary plane between the two drift chambers. The positive z-axis is pointed along the direction of particle motion in each spectrometer towards the calorimeter. The x-axis is pointed downwards to the floor (i.e. in direction of positive δ which is the difference of particle momentum and spectrometer central momentum of the spectrometer) and the positive y-axis is perpendicular to both x and z axes (i.e. pointed to the left).

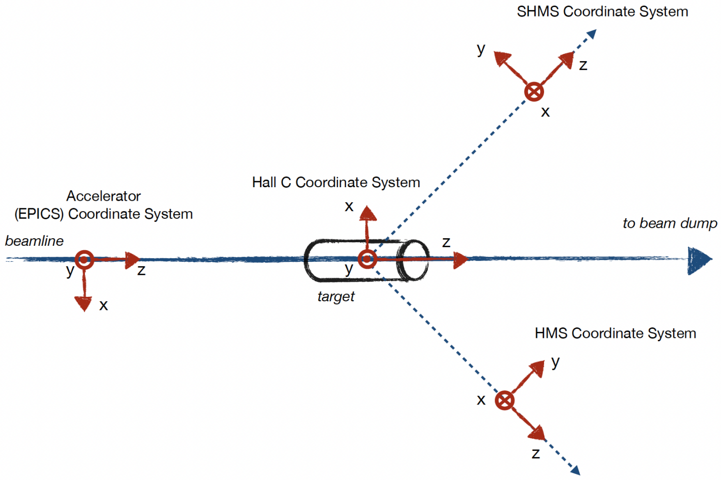

Figure 2.11: Different coordinate systems used in Hall C [34].

- The **target coordinate system** is similar to the spectrometer coordinate system as it reconstructs the path of the particle back to the target. These reconstructed target quantities can be calculated using the mass, charge, path length of the particle and the matrix elements of the magnets.

2.3 Target System

The Hall C target chamber is a large evacuated cylindrical aluminium tank in two stacked sections (Figure 2.12) that contains the solid and cryogenic targets (cryotargets) in a target ladder. As the electron beam undergoes scattering from the target, the resulting particles must traverse the target cell, pass through the chamber's exit window into the surrounding air, and then proceed through the spectrometer

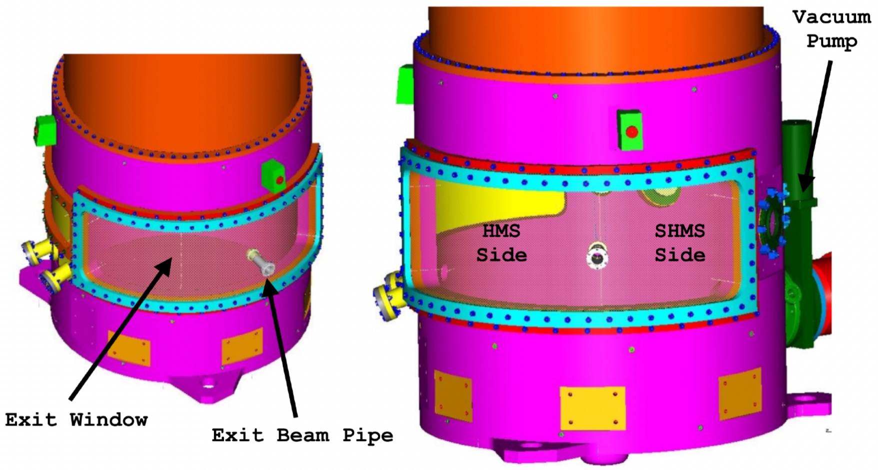

Figure 2.12: A CAD drawing of the Hall C Target Chamber design [28].

entrance window before entering the vacuum of the spectrometer. Concurrently, the un-scattered beam exits the chamber through a vacuum space, connecting to the exit beam pipe via a threaded compression flange. Additionally, the target chamber features various openings, including those for beam entry, two pumping ports, multiple view ports, and several spare ports. The view ports play a crucial role in conjunction with a remote TV camera and light, facilitating the observation of target motion and positioning in the counting room. In the standard configuration, both spectrometers share a single chamber exit window and both spectrometers' entrance window is actually very close to, but not in contact (or vacuum coupled) with the chamber window itself [28]. Table 2.2 lists the target chamber properties.

Parameter	Value
Thickness	2 inches
Inner Diameter	41 inches
Outer Diameter	45 inches
HMS Horizontal Angle	3.2° - 77.0°
SHMS Horizontal Angle	3.2° - 47.0°
Vertical Angle	± 17.3°
Pressure	$\approx\ 10^{-6}$ torr

Table 2.2: Properties of the Hall C Target Chamber [28].

2.3.1 Target Ladder

The solid and cryogenic targets are housed within a specialized target ladder, featuring a single-axis (vertical) motion system that facilitates the selection of the desired target. The target ladder includes three cryogenic target cells positioned above the solid targets. During the Kaon-LT experiment, the cryogenic target cells were configured as: Loop 1 as reserve liquid hydrogen cell (as a backup for active cryo-target), Loop 2 as active liquid hydrogen target (for physics data collection) and Loop 3 as inactive cell (not used in the experiment). The solid target were configured as: aluminium target for background subtraction in the physics data and various carbon targets for optics and beam position measurements. The targets are be moved out of the beam in order to avoid damage during the beam tuning process. The motion of the target ladder is remotely controlled through a dedicated target Graphical User Interface (GUI), as shown in Figure 2.13, located in the Counting Room. The target GUI screen provides a comprehensive overview of the experimental setup. The central white screen features a graphical representation of the targets, complete with an arrow indicating the specific target being impacted by the beam. Additionally, real-time updates on the beam current and the vacuum pressure within the target chamber are displayed at the top of this screen. Positioned on the extreme left of the GUI is a control panel designed for precise manipulation of the target ladder. On the right side of the white screen, two additional panels offer live feedback on critical parameters such as information on the coolant supply from the End Station Refrigerator (ESR), pressure and temperature of each cell. There was at least one target change for each kinematic setting during the data taking of this experiment.

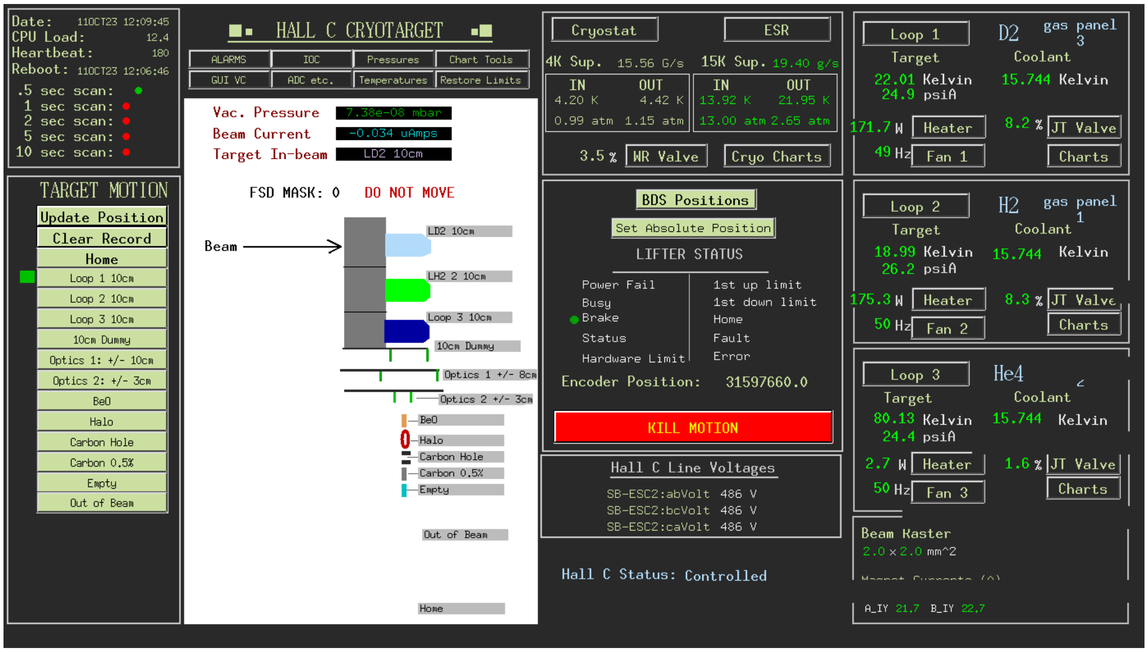

Date: 11OCT23 12:09:45
CPU Load: 12.4
Heartbeat: 180
Reboot: 11OCT23 12:06:46
.5 sec scan: ●
1 sec scan: ●
2 sec scan: ●
5 sec scan: ●
10 sec scan: ●

Vac. Pressure 7.38e-08 mbar
Beam Current -0.034 uAmps
Target In-beam LD2 10cm

FSD MASK: 0 DO NOT MOVE

4K Sup. 15.56 G/s 15K Sup. 19.40 g/s

IN	OUT	IN	OUT
4.20 K	4.42 K	13.92 K	21.95 K
0.99 atm	1.15 atm	13.00 atm	2.65 atm

3.5 % WR Valve

Encoder Position: 31597660.0

Hall C Line Voltages
SB-ESC2:abVolt 486 V
SB-ESC2:bcVolt 486 V
SB-ESC2:caVolt 486 V

Hall C Status: Controlled

Loop 1 D2 gas panel 3
Target 22.01 Kelvin 24.9 psiA
Coolant 15.744 Kelvin
171.7 W Heater
49 Hz Fan 1
8.2 % JT Valve

Loop 2 H2 gas panel 1
Target 18.99 Kelvin 26.2 psiA
Coolant 15.744 Kelvin
175.3 W Heater
50 Hz Fan 2
8.3 % JT Valve

Loop 3 He4
Target 80.13 Kelvin 24.4 psiA
Coolant 15.744 Kelvin
2.7 W Heater
50 Hz Fan 3
1.6 % JT Valve

Beam Raster
2.0 x 2.0 mm^2
A_IY 21.7 B_IY 22.7

Figure 2.13: Hall C Target GUI screen during the Kaon-LT experiment.

2.3.2 Solid Targets

- **Optics-1:** The optics target comprises carbon foils positioned at $z = -10,\ 0,\ 10$ cm along the beam axis (where $z = 0$ corresponds of the center of the target), serving the purpose of conducting studies on spectrometer optics optimization. Despite extending beyond the typical target length employed in Hall C, these foils play a crucial role in optics reconstruction across the full target length.

- **Aluminium Dummy (10 cm):** Comprising aluminium foils affixed to distinct frames at $z = \pm 5$ cm, aligning with the entrance and exit windows of the cryogenic target, the dummy target serves the purpose of collecting data dedicated for background subtraction related to the genuine aluminium cryo-target windows. It's important to highlight that the dummy target is 4.86 times thicker than the real cryo-target windows, resulting in more background statistics in a shorter duration of precious beam time. This is corrected (by a normalizing factor of 0.206), during the offline data analysis, before the background subtraction.

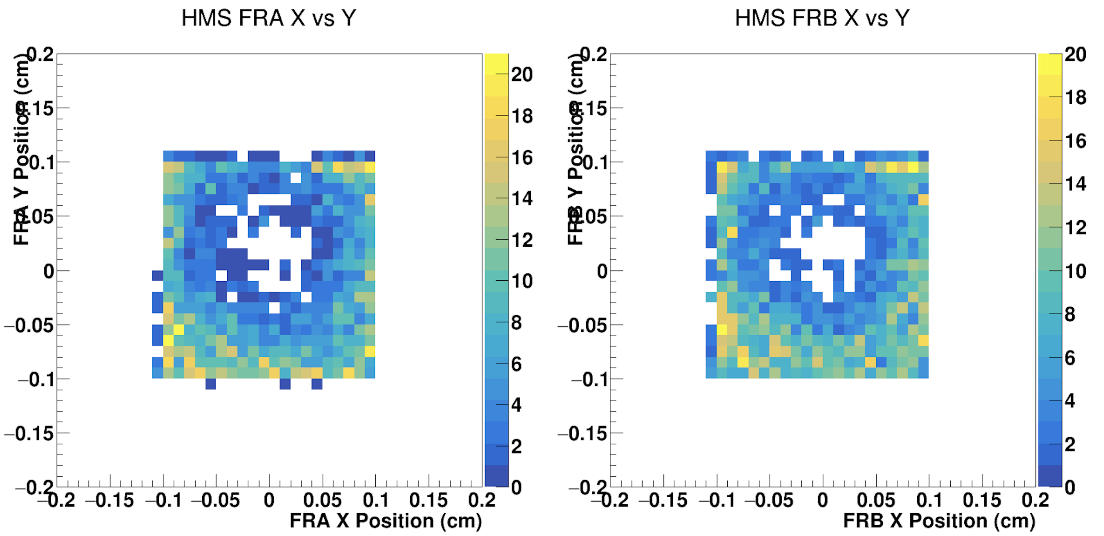

Figure 2.14: Carbon hole check during the Kaon-LT experiment shows the raster pattern for FR-A (left) and FR-B (right) raster magnets.

- **Carbon Hole:** The carbon hole target is composed of a thin carbon foil featuring a central hole with a diameter of 2 mm. Using a rastered beam of at least 2×2 mm^2, this target allows the precise beam alignment at the target. As the beam traverses the hole, interactions occur at the edges, leading to electron re-scattering, which can be detected by either spectrometer. The recorded (x,y) raster values, corresponding to detected particles, form a distinctive raster pattern incorporating the central hole, as illustrated in Figure 2.14.

2.3.3 Cryogenic Targets

A schematic of the Hall C target loop is shown in Figure 2.15 and the properties of the cryo-targets are presented in Table 2.3.

- **Liquid Hydrogen (10 cm):** The cryogenic liquid hydrogen (LH_2) is kept at a temperature of $T(LH_2) = 19 \pm 0.1$ K ($\approx$ 25 psia). LH_2 freezing and boiling points are $T(F) = 13.8$ K and $T(B) = 22.1$ K, respectively. A 2×2 mm^2 raster is used to minimize density reduction at high beam currents.

- **Liquid Deuterium (10 cm):** The cryogenic liquid deuterium (LD_2) is kept at a temperature of $T(LD_2) = 22 \pm 0.1$ K ($\approx$ 23 psia). LD_2 freezing and boiling points are $T(F) = 18.7$ K and $T(B) = 25.3$ K, respectively. A 2×2 mm^2 raster is used to minimize density reduction at high beam currents.

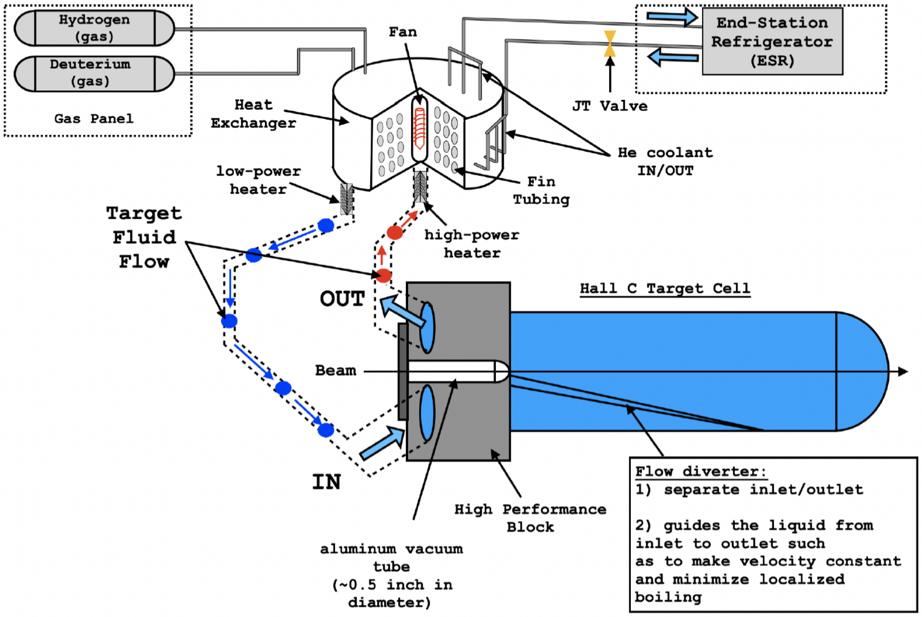

Figure 2.15: Hall C cryogenic target loop layout for the Kaon-LT Experiment [33].

Target	Thickness (mm)	Entrance (mm)	Exit (mm)
Loop 1 (10 cm)	100 ± 0.26	0.104 ± 0.0025	0.133 ± 0.0096 Tip 0.162 ± 0.014 Wall
Loop 2 (10 cm)	100 ± 0.26	0.150 ± 0.011	0.191 ± 0.019 Tip 0.219 ± 0.018 Wall
Loop 3 (10 cm)	100 ± 0.26	0.130 ± 0.012	0.188 ± 0.013 Tip 0.184 ± 0.017 Wall

Table 2.3: Properties of the Hall C cryo-targets during the Kaon-LT experiment [41]

2.4 Spectrometers

In Hall C, the primary experimental apparatus comprises a pair of magnetic spectrometers which are designed for conducting high-precision cross-section measurements at high luminosity. These spectrometers incorporate pivot-mounted bearings, enabling swift and remote rotation. Each spectrometer comprises a sequence of magneto-optical elements, including quadrupoles and dipoles, followed by a set of particle detectors housed within a shielded detector hut. These optical elements facilitate the transport of scattered particles from the target chamber to the particle detectors. Subsequently, the tracks are reconstructed at the focal plane and translated back to the target [42].

Each spectrometer is supported by a rotatable carriage, ensuring the alignment of optical elements and detectors relative to each other and the target. This support structure moves on steel wheels along steel rails, allowing for spectrometer rotation. The remote control of rotation is facilitated through the spectrometer control screens in the Counting Room. Central angles are determined with the assistance of cameras and scribed floor marks positioned at surveyed locations toward the rear end of each spectrometer, monitored remotely from TV screens in the Counting Room.

A significant component of the Hall C 12 GeV upgrade is the introduction of the Super High Momentum Spectrometer, replacing the original Short Orbit Spectrometer (SOS) that accompanied the HMS. The SHMS is engineered to achieve a

Parameter	HMS	SHMS
Central Momentum (P)	0.4 – 7.4 (GeV/c)	2 – 11 (GeV/c)
Momentum Acceptance (δ)	±8%	−10% – +20%
Scattering Angle (θ)	10.5° - 90°	5.5° - 40°
Horizontal Angle Acceptance	±32 mrad	±18 mrad
Vertical Angle Acceptance	±85 mrad	±50 mrad
Solid Angle Acceptance	8.1 msr	> 4 msr
Horizontal Angle resolution	0.8 mrad	0.5 – 1.2 mrad
Vertical Angle resolution	1.0 mrad	0.3 – 1.1 mrad
Target resolution	0.3 cm	0.1 – 0.3 cm
Max. Flux within Acceptance	≈ 5 MHz	≈ 5 MHz

Table 2.4: Demonstrated performance of the HMS and design specifications for the SHMS [28].

maximum central momentum of 11 GeV/c, aligning with the maximum beam energy delivered to Hall C. The SHMS can be rotated to small forward central angles, reaching down to 5.5°. It operates at a high luminosity of 10^{39} $\mathrm{cm}^{-2}\mathrm{s}^{-1}$, featuring asymmetric momentum acceptance ($-10\% < \frac{\Delta P}{P} < +20\%$), measuring the percentage deviation of particle momentum relative to the spectrometer's central momentum. For an in-depth understanding of the HMS performance parameters and

SHMS design specifications, refer to Table 2.4.

2.4.1 Magnet Systems

The optical components of the spectrometers consist of a sequence of superconducting magnets designed to direct scattered particles towards a detector stack. To maintain the superconducting temperatures of the magnet coils, a continuous supply of liquid helium (^{4}He) at a temperature of 4.5 K is delivered from the End Station Refrigerator (ESR) to Hall C. This cryogenic supply is distributed to each spectrometer through flexible transfer lines originating from a main distribution box located above the pivot, integrated into each spectrometer's cryogenics network. Located on the spectrometer support structure adjacent to the magnets, the magnet power supplies ensure uninterrupted high current supply to the magnet coils. These power supplies undergo water-cooling at a constant flow rate, which can be monitored by a water flow meter situated on the electronic boxes near the pivot. Operation and monitoring of the magnet cryogenics, power supplies, and spectrometer rotation controls are executed remotely through the magnet control screens in the Hall C Counting Room [28].

Table 2.5 presents a summary of the design parameters of the spectrometer magnets. Each spectrometer is engineered to provide point-to-point focusing (Q1, Q2, Q3) and vertical momentum dispersion (D). The first quadrupole (Q1) is used to

Magnet	Type	EFL (m)	Aperture (cm)	P (GeV/c)	Current (A)	Field T/m	Energy (MJ)
HMS Q1	Cold Fe	1.867	40	7.4	1012	7.148	0.335
HMS Q2	Cold Fe	2.104	60	7.4	1023	6.167	1.59
HMS Q3	Cold Fe	2.104	60	7.4	1023	6.167	1.59
HMS D	Warm Fe	5.122	40	7.4	3000	2.073 T	0.79
SHMS HB	C	0.752	14.5 × 18	11	3930	2.56 T	0.2
SHMS Q1	Cold Fe	1.86	40	11	2460	7.9	0.382
SHMS Q2	$cos(2\theta)$	1.64	60	11	3630	11.8	7.6
SHMS Q3	$cos(2\theta)$	1.64	60	11	2480	7.9	3.4
SHMS D	$cos(\theta)$	2.85	60	11	3270	3.9 T	13.7

Table 2.5: Spectrometer magnets design parameters

focus charged particles in the horizontal axis. This is followed by second quadrupole (Q2) which serves as a vertical focusing magnet. This vertical focusing results in defocusing in the horizontal direction which is corrected the final quadrupole (Q3) which refocuses the charge particles in the horizontal axis. The quadrupoles are important for the angle acceptance of the spectrometer. Finally, the dipole (D) is used to disperse the charged particles vertically, giving rise to the momentum acceptance of the spectrometer. After passing through each magnet, the charged particles form an hour glass distribution focusing on a curved plane (known as focal plane) located between the two drift chambers. Moreover, the polarity of the spectrometer magnets can be configured to transport either positively or negatively charged particles. The central momentum is also set individually for each magnet using a field setting program that employs a current-to-field map associated with a central momentum for each magnet. Refer to [43] for the comprehensive operational guidelines of the spectrometer magnets.

2.4.2 HMS Magnets

The optical components of the HMS consist of a specific configuration known as (QQQD), involving three quadrupoles (Q1, Q2, Q3) and a dipole (D) magnet. These elements work in tandem to guide scattered particles into a sequence of particle detectors housed within a detector hut (refer to Figure 2.16). The quadrupoles focus the collimated particles into the dipole, which in turn vertically bends the central momentum particles by 25°, directing them into the detector stack.

The HMS is capable of detecting particles with central momentum ranging from $0.4 - 7.4$ GeV/c and offers the flexibility of rotation from 10.5° - 90°. The minimum and maximum angles are constrained by administrative, software, and hardware limits, contingent on the beamline configuration and Hall obstructions during the experiment. A special downstream beamline was installed during the Kaon-LT experiment,

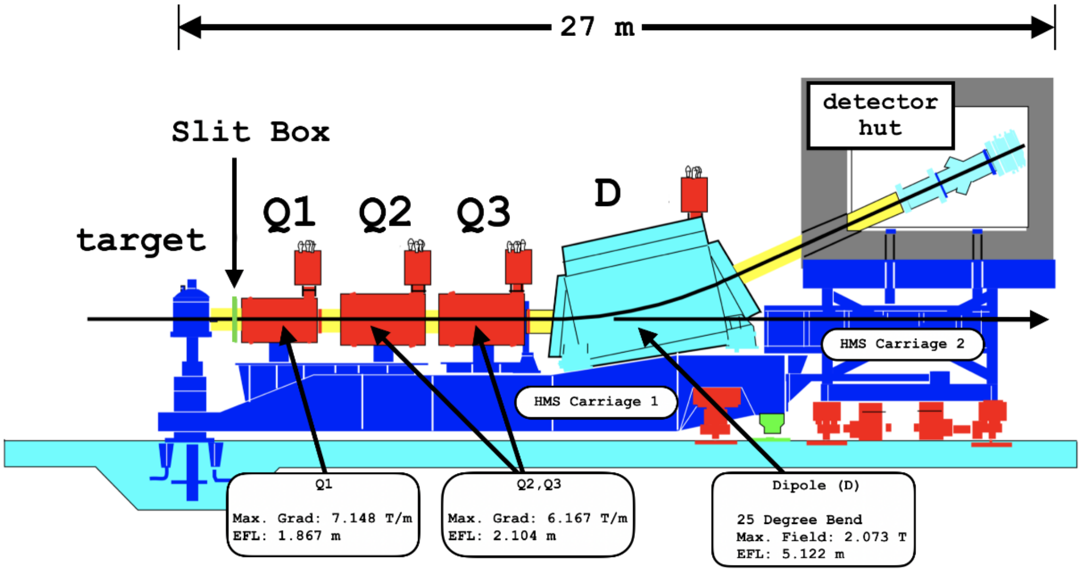

Figure 2.16: High Momentum Spectrometer (HMS) side view [33].

which allowed data taking at small opening angle (between two spectrometers) and forward angle for SHMS. The support structure for the spectrometer magnets and shield hut, housing detectors, consists of two separate but attached carriages. These carriages ensure the alignment of detectors and magnets with each other and the target.

Although the HMS is a well-understood spectrometer from the 6 GeV era, it underwent minor modifications to meet the experimental demands of the 12 GeV era, necessitating a re-commissioning process. Specifically, the NMR probe employed for precise field regulation of the HMS dipole was replaced and located to a different spot than before. Additionally, the old HMS drift chambers were replaced with a new design akin to the SHMS drift chambers. The Kaon-LT experiment required the operation of the HMS central momentum above approximately 4 GeV/c, where saturation effects in the dipole and quadrupole magnets were anticipated. Given that very few experiments in the 6 GeV era required HMS central momenta exceeding 4 GeV/c, special runs involving hydrogen elastic scattering and carbon data were conducted during the experiment. The data from these runs were crucial for the re-optimization of the HMS reconstruction optics.

2.4.3 SHMS Magnets

Much like the HMS, the SHMS incorporates an arrangement of three quadrupoles (Q1, Q2, Q3) and a dipole (D) magnet within its optical elements to direct scattered particles towards particle detectors located within a shielded hut. Notably, the SHMS introduces an additional dipole magnet (d) positioned between the target chamber and the first quadrupole, referred to as the Horizontal Bender (HB). The magnets are configured in a (dQQQD) optics arrangement (refer to Figure 2.17).

The HB serves the purpose of horizontally bending the scattered particles, matching the SHMS central momentum by 3° away from the beamline and towards the collimator before entering Q1. To achieve this horizontal bend, the optical axis of the HB is oriented 3° closer to the beamline compared to the optical axis of the rest of the spectrometer components (collimator, Q1, Q2, Q3, D, detectors). Equipped with the

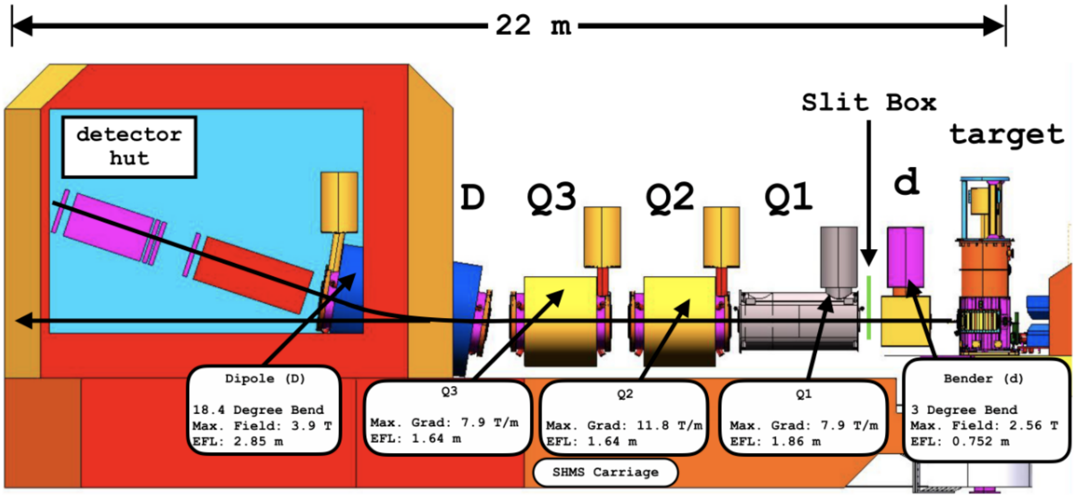

Figure 2.17: Super High Momentum Spectrometer (SHMS) side view [33].

HB, the SHMS can detect particles at angles that would have been otherwise inaccessible due to obstructions from the quadrupole magnets and shield house along the beamline. This property of SHMS allowed data collection over the full azimuthal angle ϕ and, more importantly, the access to low $-t$ region for meson electroproduction reaction which is critical for the Kaon-LT experiment.

As the particles are horizontally bent towards the collimator and enter Q1, they pass through the remaining quadrupoles (Q2, Q3) and into the dipole (D), where central-momentum particles are vertically bent by 18.4° into the detector stack. The SHMS is capable of detecting particles with central momentum ranging from $0.2-11$ GeV/c and can be rotated from a central angle of 8.5° up to 40°. Due to the 3-degree bend by the HB, the central-ray particles detected at the hut actually scatters from the target 3° less than the hut, resulting in the SHMS's full angular coverage spanning from 5.5° to 40°.

Given that the SHMS is a new addition to the spectrometer lineup, substantial efforts during the commissioning run period were dedicated to comprehending and optimizing the magnetic optics, as well as commissioning the particle detectors. A number of these studies are described in detail in the next chapter.

2.5 Focal Plane Detectors

Each spectrometer consists of a similar array of particle detectors, located within a shielded hut. The detector package comprises a pair of drift chambers (DC1 and DC2) dedicated to precise track reconstruction, two sets of hodoscope planes for particle triggering, a calorimeter facilitating electron-hadron separation, and a gas and aerogel Cherenkov (only in the SHMS) for additional particle identification.

In the HMS configuration (refer to Figure 2.18), particles enter the detector hut through a cylindrical vacuum vessel extending from the dipole exit window to upstream of DC1. Upon exiting the vacuum vessel, particles traverse the drift chamber pair, followed sequentially by an initial pair of XY hodoscope planes, a Heavy Gas Cherenkov (HGC), a subsequent pair of XY hodoscope planes, and culminating with a preshower and shower counters constituting the calorimeter detector.

For the SHMS (see Figure 2.19), particles entering the detector hut traverse a vacuum vessel (akin to HMS) which extends from the entrance window to the exit

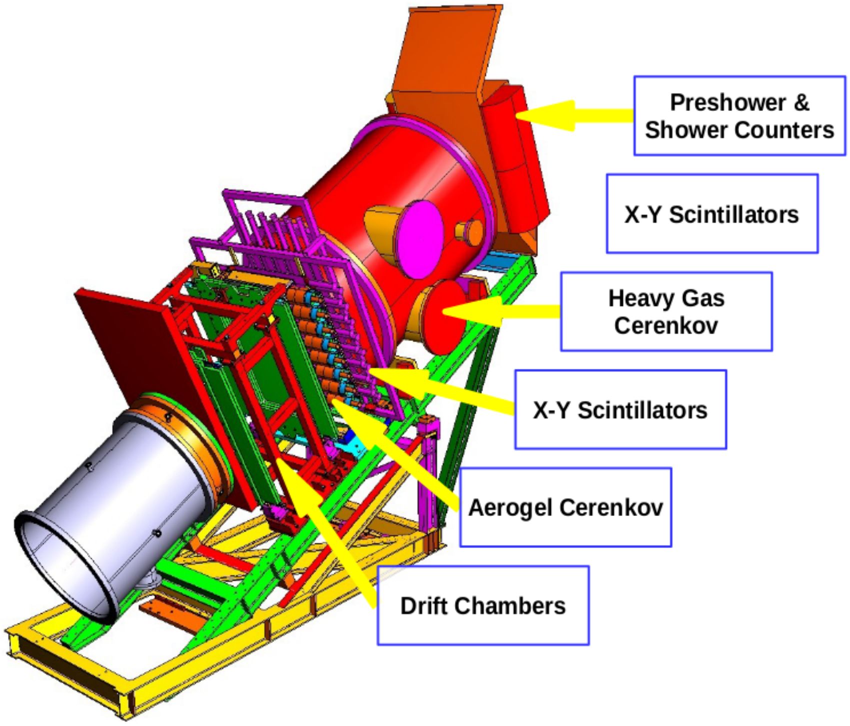

Figure 2.18: High Momentum Spectrometer (HMS) detector stack [33].

window, partially protruding into the hut. The vacuum extension pipe, contingent on experimental needs for particle identification, can be substituted with the Noble Gas Cherenkov (NGC) at higher spectrometer momenta, minimizing the impact of multiple scattering effects. Upon exiting the vacuum vessel (or NGC, depending on the experiment configuration), particles sequentially pass through a pair of drift chambers, followed by a pair of XY hodoscope planes, a Heavy Gas Cherenkov, an aerogel Cherenkov, a subsequent pair of XY hodoscope planes, and ultimately, the preshower and shower counters forming the calorimeter detector. During the Kaon-LT Experiment, the NGC detector was not used in the SHMS detector stack because

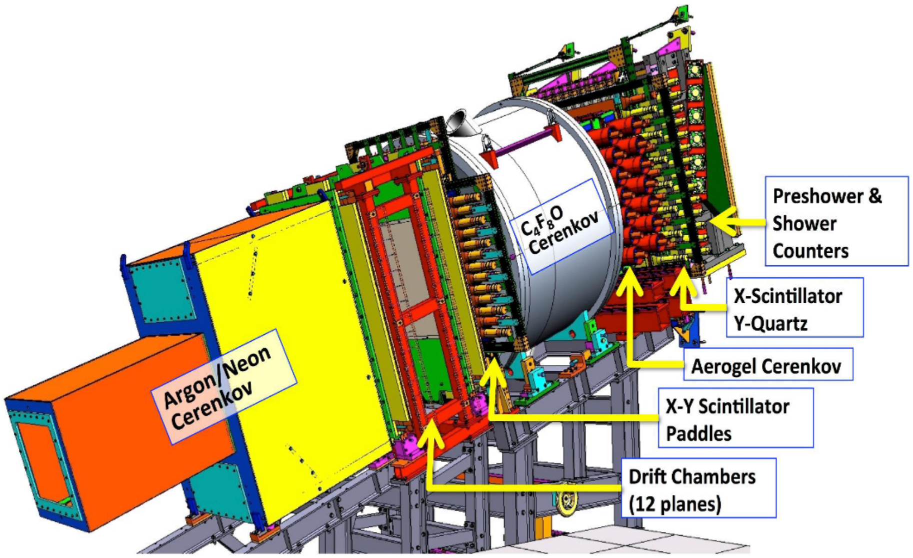

Figure 2.19: Super High Momentum Spectrometer (SHMS) detector stack [33].

data with negative polarity was not taken and high confidence $e' - \pi^-$ separation was not needed.

2.5.1 Drift Chambers

The design of the drift chambers is a shared feature in both the HMS and SHMS, each spectrometer is equipped with two chambers mounted on an aluminium frame and positioned approximately 80 cm apart (see Figure 2.20). The DC layout in both spectrometers is similar, but their dimensions are different. Within each chamber, configurations consist of 6 anode (wire) planes and 8 cathode planes, with a middle plane facilitating the mounting of 16-channel amplifier discriminator cards for sense wire readout. The arrangement of DC1 and DC2 is defined by an “imaginary” focal plane, chosen to coincide with the spectrometer focal point (see Figure 2.20). The wire planes in each chamber are designed for left/right ambiguity resolution (precise position resolution), enabling a 180° rotation of un-primed wire planes about the z-axis.

These wire planes incorporate alternating field and sense wires, with sense wires made of 20 μm gold-plated tungsten and field wires made of copper-plated beryllium (100 μm thickness in HMS and 80 μm in SHMS). The sense wire numbering is determined by the direction of the perpendicular vector, pointing towards increasing wire numbers (see Figure 2.21). Operational functionality involves a gas mixture (50:50

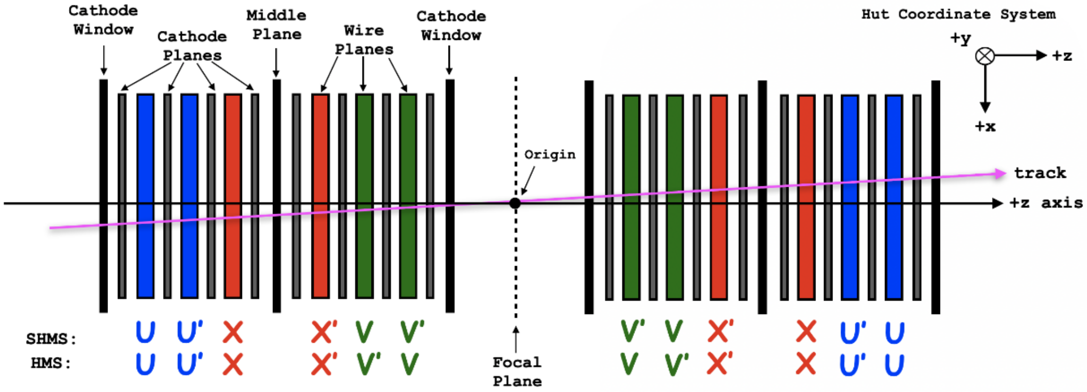

Figure 2.20: Side view of the plane orientation for the DC1 (left) where the colored planes represent the wire planes, and DC2 (right) which is identical in design to DC1 rotated by 180° about the x-axis (vertical) forming a mirror image along the z-axis [33].

argon/ethane) in each chamber, where charged particles ionize argon gas atoms, generating an electron avalanche. Ethane is used as quenching gas which allows stable operation over a wide range of momenta and reduces dead time. The cathode planes and field wires are maintained at a negative potential relative to the sense wires, establishing an electric field with field lines pointing away from the sense wires. The design and operational considerations of the drift chambers contribute to their role in

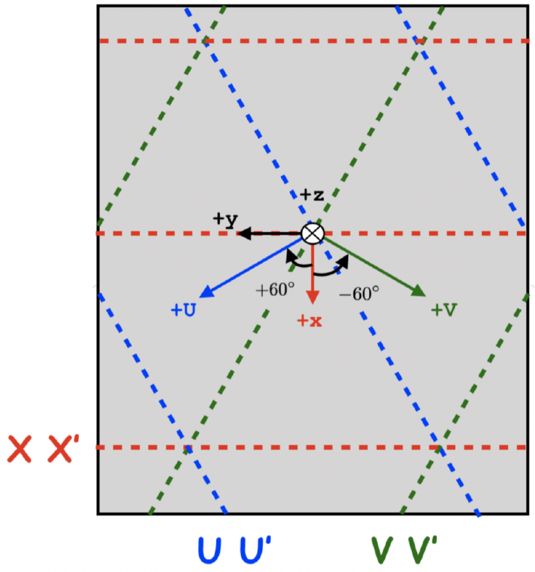

Figure 2.21: Front view of the wire (dashed) orientations for each plane, indicated by representative sense wires of different colors, where the $+z-axis$ (particle direction) is into the page. The wires in each plane are superimposed onto a single plane in this figure for convenience and their orientation is defined by the vector normal to the wire [33].

precise track reconstruction and particle identification within the experimental setup as described in Section 3.5.1.

2.5.2 Hodoscopes

The spectrometers are each outfitted with two pairs of scintillator arrays, forming hodoscope planes that are separated by a distance of approximately 2.2 m. Within each pair, segmentation along the dispersive (x-axis) and non-dispersive (y-axis) directions is achieved through long rectangular elements, comprising either plastic scintillator paddles or quartz bars, each equipped with photomultiplier tubes (PMTs) at both ends. The plastic scintillating materials employed are BC-404 from Saint-Gobain

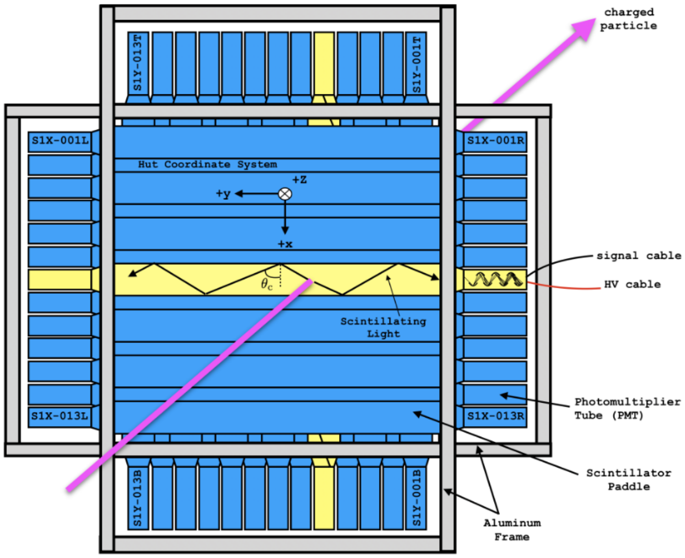

Figure 2.22: Front view of the SHMS S1X (front) and S1Y (back) hodoscope planes [33].

Crystals for the HMS and RP-408 from Rexon Corporation for the first three planes of the SHMS (as shown in Figure 3.11). The final plane in the SHMS, known as the quartz plane, is constructed using Corning HPFS 7980 Fused Silica (quartz) bars. To eliminate potential gaps between adjacent elements and prevent undetected particle passage, the paddles/bars are slightly overlapped by a few millimeters in each plane. Detailed dimensions for each paddle in every hodoscope plane for both spectrometers are summarized in Table 2.6.

The fast-timing properties of plastic scintillators make the hodoscope detector

Plane	Thickness (mm)	Width (cm)	Length (cm)	No. of Elements
HMS 1X	2.12	8.0	75.5	16
HMS 1Y	2.12	8.0	75.5	10
HMS 2X	2.12	8.0	75.5	10
HMS 2Y	2.12	8.0	75.5	10
SHMS 1X	5	8.0	100	13
SHMS 1Y	5	8.0	100	13
SHMS 2X	5	10.0	110	14
SHMS 2Y	25	5.5	125	21

Table 2.6: Summary of hodoscopes paddle dimensions for each plane.

particularly suitable for particle triggering, especially after the 12 GeV energy upgrade, where particle rates significantly increase. The inclusion of the quartz plane in the SHMS detector package serves the dual purpose of time-of-flight measurement and particle identification. This is crucial for particle tracking at higher rates where background levels are expected to be elevated. Despite both plastic scintillators and quartz emitting light due to charged particle interactions, the mechanisms differ. In a scintillator, charged particles excite molecules in the material, causing them to emit scintillation photons through fluorescence. The photons travel to the scintillator paddle's end, where a PMT detects them, producing photoelectrons via the photoelectric effect. These electrons create an electron avalanche towards the PMT's anode, generating a measurable analog signal sent to the Counting Room for further processing (see Figure 3.11).

As light propagates through the scintillator material, the potential for light loss due to partial reflection exists at boundaries. To mitigate this, scintillators are wrapped in highly reflective aluminum foil and multiple layers of Tedlar (HMS) or electrical tape (SHMS) to ensure light tightness. In contrast to plastic scintillators, the radiation produced in the quartz plane relies on the Cherenkov effect, a topic to be explored further in the subsequent detector section.

2.5.3 Cherenkovs

At elevated particle momenta ($\geq$ 3 GeV/c), the efficacy of the hodoscope Time-of-Flight (TOF) method for distinguishing between different particles diminishes significantly. This limitation stems from the relationship $\Delta t \approx 1/p^2$, where Δt represents the hodoscope time difference between the first and second pair of planes, and p denotes the particle momentum. Consequently, at higher particle momenta, the identification of individual particles becomes challenging due to the minute time differences between particles of varying masses. To address this challenge, the incorporation of supplementary particle identification detectors becomes imperative. The Hall C spectrometers feature a suite of threshold Cherenkov particle detectors, reliant on the Cherenkov effect, a phenomenon occurring when a charged particle traverses a transparent medium at a velocity exceeding the speed of light in that medium (c/n, where n is the index of refraction of the material). This results in the emission of Cherenkov radiation in a conical pattern around the particle's trajectory (refer to Figure 2.23). In the Cherenkov effect, the electromagnetic disturbance (light) generated by the charged particle's passage is akin to the sound waves emitted by a supersonic jet. As the charged particle outpaces the spherical waves it emits, a conical shape is formed, as described by the relation:

$$cos(\theta_c) = \frac{1}{n\beta} \tag{2.13}$$

where $\beta = v/c$ is the ratio of the velocity (v) of the charged particle to the speed of light in vacuum (c) and $n = c/v$ is the index of refraction of the medium, where v is the speed of light in the medium. Alternatively, $\beta = p/\sqrt{m^2c^4 + p^2c^2}$ where m is the particle mass. Since the charged particle must travel faster than light in the medium for Cherenkov light to be emitted, one requires $v > c/n \rightarrow n > 1/\beta$ which can be expressed in terms of momentum as:

$$n > \frac{\sqrt{m^2c^4 + p^2c^2}}{p} \tag{2.14}$$

From this inequality, the index of refraction of the medium can be adjusted accordingly such that at a fixed momentum, the mass of the particle will determine whether or not Cherenkov radiation will be produced.

Both the gas and aerogel threshold Cherenkov detectors in Hall C utilize this basic inequality for particle identification. In addition, for the gas Cherenkovs, the quantity $(n - 1)$ is proportional to the gas pressure (provided the pressure is well below the vapour pressure of the gas), which can be adjusted to change the index of refraction and hence select the desired particle mass that will trigger the Cherenkov effect. Below is a brief description of each Cherenkov detector.

- **Gas Cherenkov:** Positioned between the front and rear hodoscope planes, each spectrometer is equipped with a Gas Cherenkov detector containing a gas held at a specific pressure, tailored to the experimental requirements. To

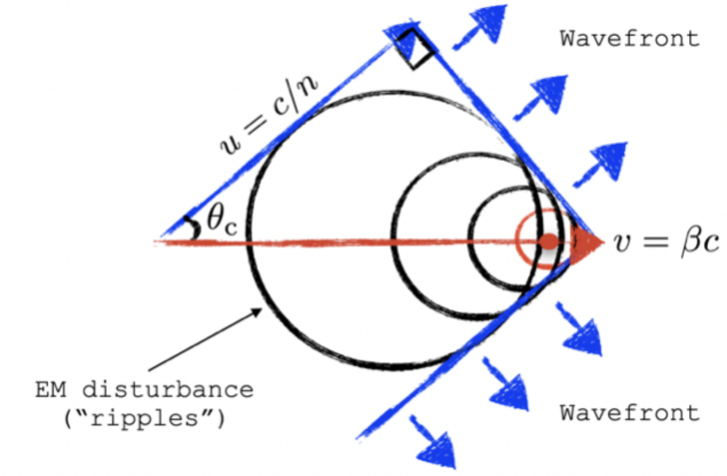

Figure 2.23: Cartoon of the Cherenkov effect. The charged particle (red) traverses a medium faster than the speed of light (blue) in that medium, producing a conical light wavefront [33].

enhance detection efficiency, the detector incorporates mirrors mounted and oriented to reflect and focus the Cherenkov light towards the photomultiplier tubes (PMTs). The HMS Cherenkov configuration features a 1.5-meter-long cylindrical tank housing two spherical mirrors that concentrate the Cherenkov light onto two PMTs. The operational versatility of this detector extends to functioning as an e/π discriminator, the tank is filled with C_4F_{10} or N_2 gas, at variable operating pressures dictated by the experiment. In contrast, the SHMS Heavy Gas Cherenkov (Fig. 2.24) comprises a 1.3-meter-long cylindrical tank (1.88 m in diameter) with four mirrors directing light onto four PMTs. Filled with C_4F_{10} or C_4F_8O gas, functionally equivalent, this detector operates as an

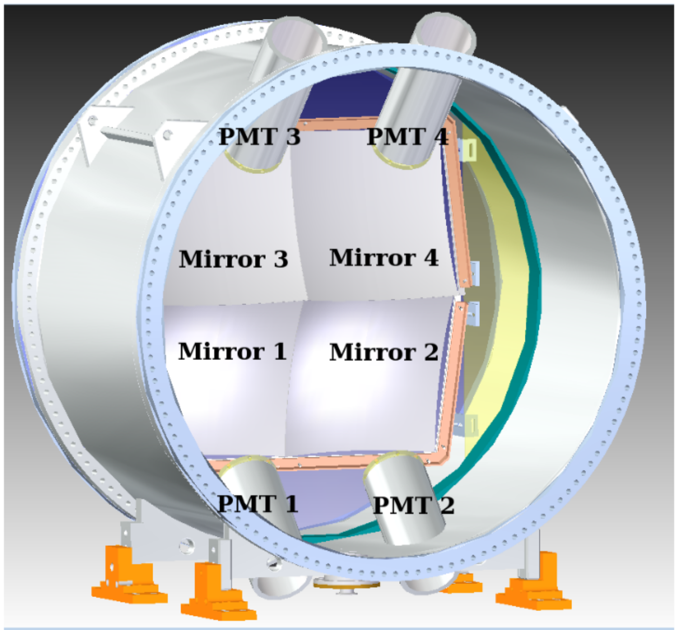

Figure 2.24: CAD rendering of the SHMS Heavy Gas Cherenkov detector [28].

e/π or π/K discriminator, with the specific discrimination dependent on the gas pressure employed. During the Kaon-LT experiment, the HMS gas Cherenkov used C_4F_{10} at 0.48 atm pressure. The SHMS HGC used the same gas mixture with a higher pressure of 0.9 atm.

- **Aerogel Cherenkov:** Integral to the physics investigations conducted at Hall C is the imperative for precise $p/\pi/K$ separation. To achieve robust particle identification, the SHMS is equipped with an aerogel Cherenkov detector. In contrast to the gas Cherenkov, this detector utilizes silica aerogel, a transparent and highly porous material characterized by a refractive index typically intermediate between that of gases and liquids. The design of the aerogel detector in each spectrometer shares similarities, comprising an aerogel tray succeeded by a light diffusion box featuring highly reflective inner boundaries. As a charged particle traverses the aerogel material, certain particles emit Cherenkov light based on the refractive index. This emitted light travels into the diffusion box, where it undergoes reflection at the box's boundaries and is directed into an array of photomultiplier tubes (PMTs) mounted on each side. The analog signal from the light collected by the PMTs is transmitted to the Counting Room for subsequent signal processing [44]. Table 2.7 summarizes the threshold momenta for different particles in each aerogel tray and Figure 3.10 shows a CAD diagram of the SHMS aerogel Cherenkov.

Particle	P_{Th} GeV/c $n = 1.011$	P_{Th} GeV/c $n = 1.015$	P_{Th} GeV/c $n = 1.020$	P_{Th} GeV/c $n = 1.030$
π	0.935	0.803	0.692	0.565
K	3.315	2.840	2.453	2.000
p	6.307	5.379	4.667	3.802

Table 2.7: Threshold momenta for different hadrons for each aerogel tray [44].

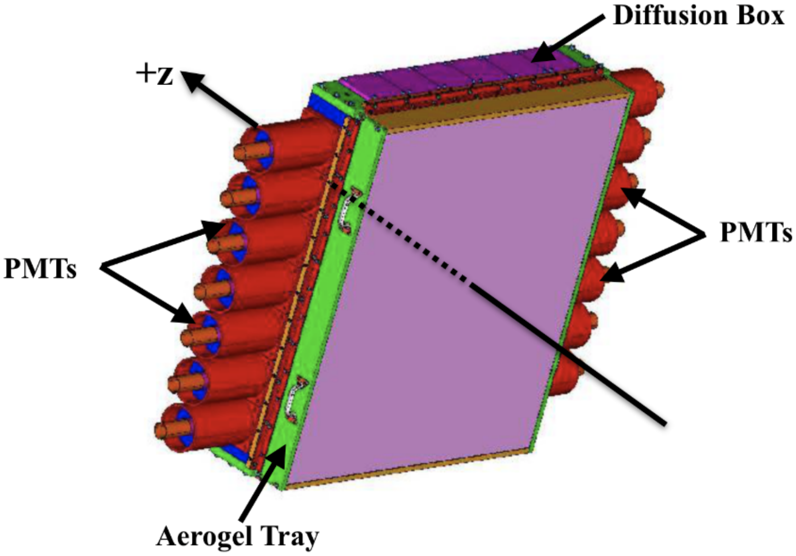

Figure 2.25: CAD rendering of the SHMS aerogel Cherenkov detector [44].

2.5.4 Calorimeters

The electromagnetic (EM) calorimeter in each spectrometer primarily serves the purpose of electron-hadron discrimination, complementing the gas Cherenkov detectors to enhance electron identification and suppress hadrons more effectively. Positioned at the end of the detector stack, these calorimeters facilitate a destructive measurement of the projectile particle's energy. The projectile energy measurement relies on the detection of Cherenkov radiation, primarily emitted from electromagnetic showers generated through bremsstrahlung and pair production processes. As electrons traverse the calorimeter, they undergo deceleration by the calorimeter radiator, emitting bremsstrahlung photons that decay into (e^+e^-) pairs via pair production.

These pairs subsequently radiate additional bremsstrahlung photons, initiating a cascade reaction leading to an electromagnetic shower until most or all of the initial electron energy is deposited in the calorimeter.

Figure 2.26 illustrates a single electron with an initial energy, E_o, entering the calorimeter radiator material, triggering a particle cascade. The horizontal axis, defined as a multiple of one radiation length (X_0 [g/cm^2]), reflects the decreasing energy of the cascade along the particle trajectory. The radiation length is the mean distance over which a high-energy electron loses all but $1/e$ of its initial energy due to bremsstrahlung radiation. To ensure effective absorption of the incident projectile

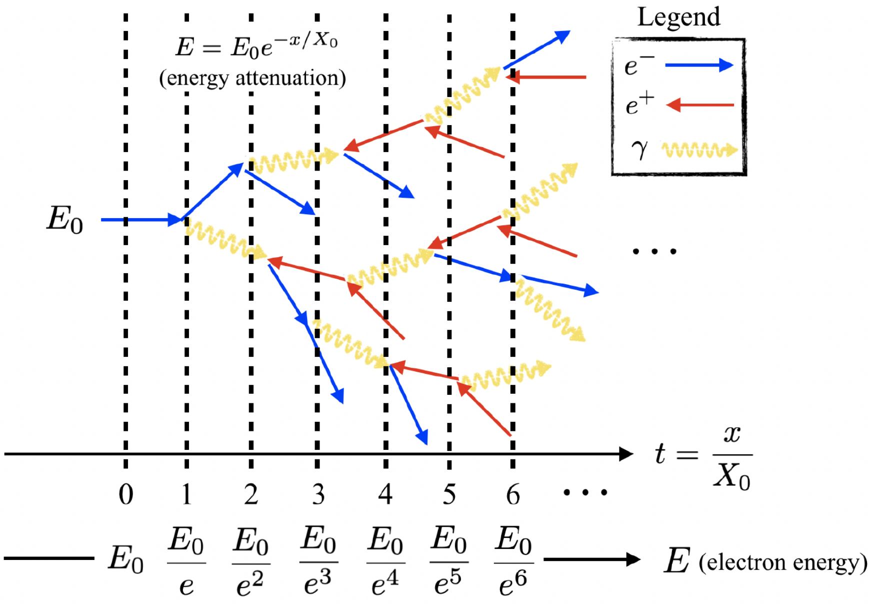

Figure 2.26: Typical electromagnetic shower cascade in a calorimeter [33].

energy in the radiator material, the Hall C calorimeters consist of several stacked layers of thick lead glass blocks tilted slightly lower relative to the spectrometer central ray. The original HMS calorimeter (see Figure 2.27) commissioned in 1994 remains in use, comprising 52 TF-1 lead glass modules in four layers, with each block measuring $10 \times 10 \times 70$ cm^3. The calorimeter, with a total of ≈ 14.6 radiation lengths, effectively absorbs most of the electron projectile energy. The total energy deposited is read out by PMTs coupled at both ends of the first two layers and at one end on the last two layers.

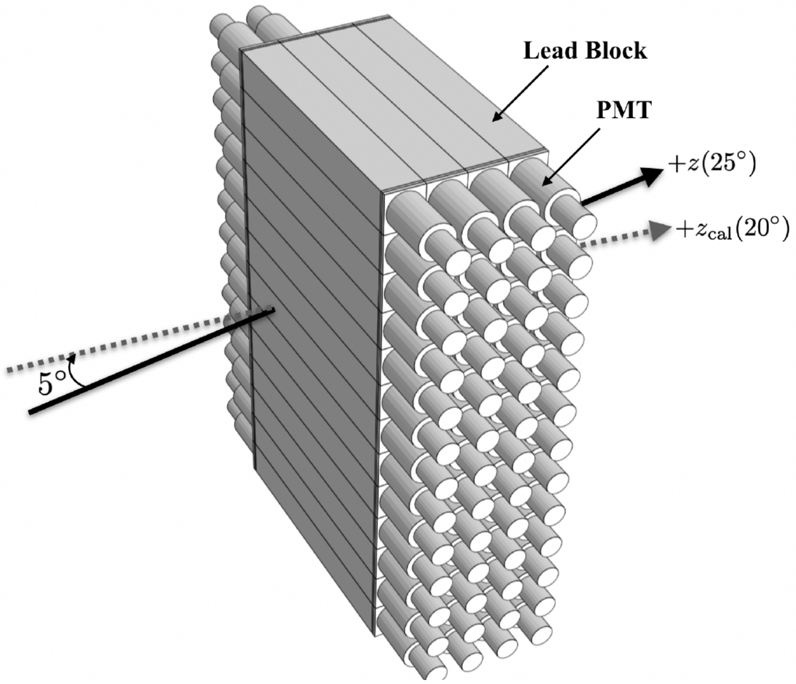

Figure 2.27: HMS electromagnetic calorimeter. The entire detector is tilted vertically by 5° lower relative to the central ray of the spectrometer hut [33].

The SHMS calorimeter (see Figure 2.28) incorporates TF-1 and F-101 type lead glass modules assembled into preshower and shower counters. The pre-shower blocks, obtained from the decommissioned SOS calorimeter, consist of 28 modules stacked in two adjacent columns, each coupled to a PMT at one end. In contrast, the shower counter blocks are sourced from the decommissioned HERMES calorimeter and consist of 224 modules, each measuring $8.9 \times 8.9 \times 50$ cm^3, coupled to a PMT towards the long end of the block. The general configuration, ≈ 18 radiation lengths deep, ensures effective absorption of EM showers from the highest energetic projectiles (≈ 10 GeV). The pre-shower counter, only 3.6 radiation lengths thick, is placed before the shower to enhance particle identification by detecting the early onset of EM showers.

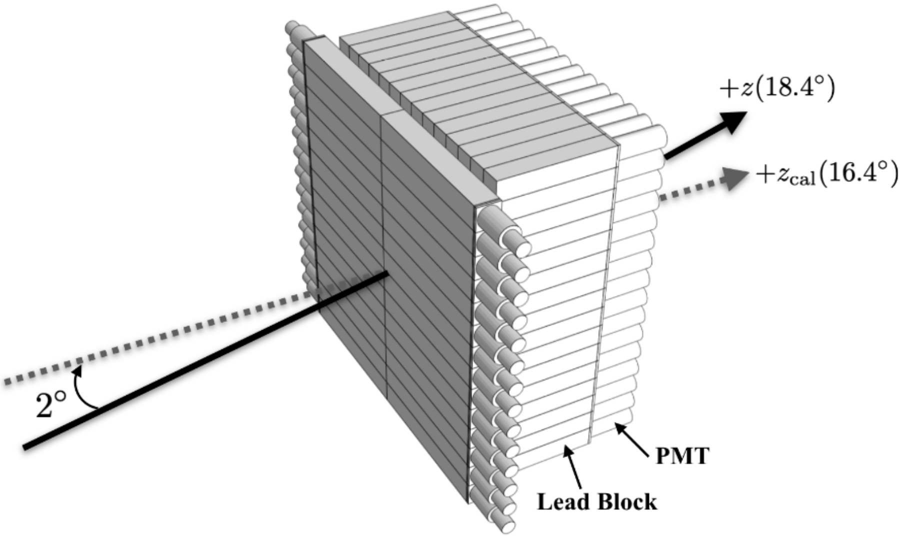

Figure 2.28: SHMS electromagnetic calorimeter. The entire detector is tilted vertically by 2° lower relative to the central ray of the spectrometer hut [33].

2.6 Data Acquisition and Trigger System

The Hall C data acquisition consists of a set of NIM electronics to create and process event triggers, while event readout is handled by dedicated equipment. The hardware trigger system plays a pivotal role in the data acquisition process, distinguishing real physics events from background noise. It efficiently reduces the high event rates and minimizes computer dead time while preserving optimal trigger efficiency. Signals from detectors, such as hodoscope PMTs, are readout and converted into digital form using fast analog-to-digital converters (FADCs) and time-to-digital converters (TDCs). For calorimeters and Cherenkov detectors, FADC250 modules with 16 ADC channels, operating at a 4 ns sampling period, handle signal digitization. In contrast, discriminated signals from the drift chambers are processed by CAEN V1190A TDCs, which feature 128 channels and provide a resolution of 100 ps. The discriminated signals are also sent to scaler counters that log the number of detected events. After digitization, the analog signals are stored in modules and buffered by Read-Out Controllers (ROCs), which temporarily hold the data before transferring it to the main data acquisition system (DAQ). Most ADC and TDC modules are read by ROCs housed in the Hall C Counting House Electronics Room, with the exception of the HMS/SHMS drift chamber TDCs and SHMS shower ADCs, which are processed by ROCs in their respective detector huts. The Trigger Interface (TI) module then consolidates the digitized signals and scaler data from the ROCs, forwarding them to the trigger logic for further analysis and verification against set trigger conditions.

2.6.1 HMS Trigger

The HMS single arm pre-trigger is formed from the standard hodoscopes' discriminated signals and a combination of other detector's discriminated signals as required by the experiment. The standard and other experiment-specific discriminated detector signals are sent to a P/S Model 755 NIM logic unit to form a final single-arm pre-trigger (hHODO 3/4, hELREAL, hELCLEAN). A copy of every discriminated detector signals (shown in red in Figure 2.29) is sent to scalers/TDCs (not shown). The final pre-triggers are sent to the front-end of the TI module in ROC 01, which can receive up to 6 individual pre-triggers. A copy of the accepted trigger (Level 1 or L1 Accept) is sent via fiber optics cables to all the ROCs associated with the HMS for data readout by all fADC/TDC modules. A copy of certain final pre-triggers are also OR'ed and are ultimately distributed to all ROCs with fADC/TDC modules to function as a reference time associated with the L1 Accept. The reference time is subtracted from every channel in every fADC/TDC module on an event-by-event basis to reduce intrinsic jitter and achieve the design resolution of the module. To guarantee that every event has an associated reference time, the HMS standard pre-trigger (hHODO-3/4) is OR'ed with the hELREAL pre-trigger to guarantee a reference time in the rare case where the hHODO 3/4 fails due to trigger inefficiency which is very small. The Kaon-LT experiment used HMS ELREAL trigger for selecting electrons.

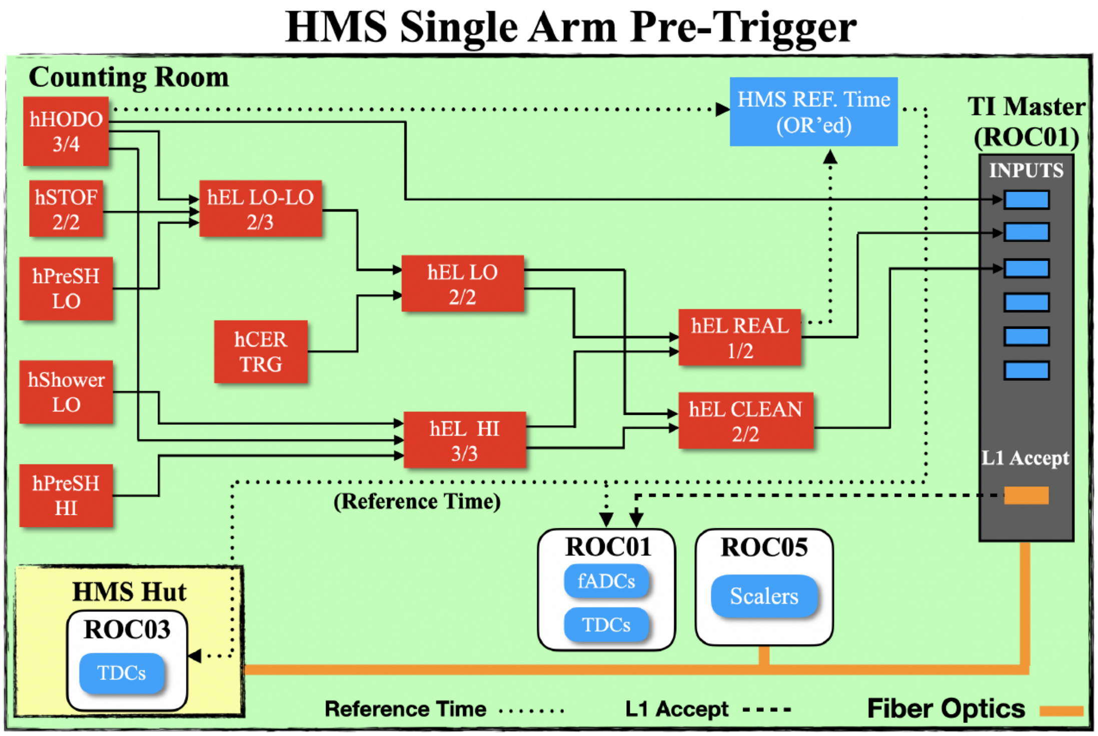

Figure 2.29: HMS single arm pre-trigger electronics diagram [33].

2.6.2 SHMS Trigger

The three planes (X1, Y1, X2) of scintillator arrays and the quartz plane (Y2) form part of the standard SHMS trigger configuration (see Fig. 2.30). Additional particle detectors may also be incorporated into the SHMS trigger as required by different experiments. The NGC and calorimeter triggers are used for e/π discrimination, whereas the HGC and aerogel Cherenkov triggers are used for $e/\pi/p$ and $\pi/K/p$ discrimination, respectively, depending on the gas pressure and aerogel material used. The SHMS single arm trigger is formed exactly as the HMS single arm trigger, with the exception of the detector's pre-triggers involved which depend on the experiment. The Kaon-LT experiment used SHMS-3/4 trigger for selecting positively charged hadrons and ELREAL trigger for selecting electrons during calibration data (as discussed in Section 2.7.1).

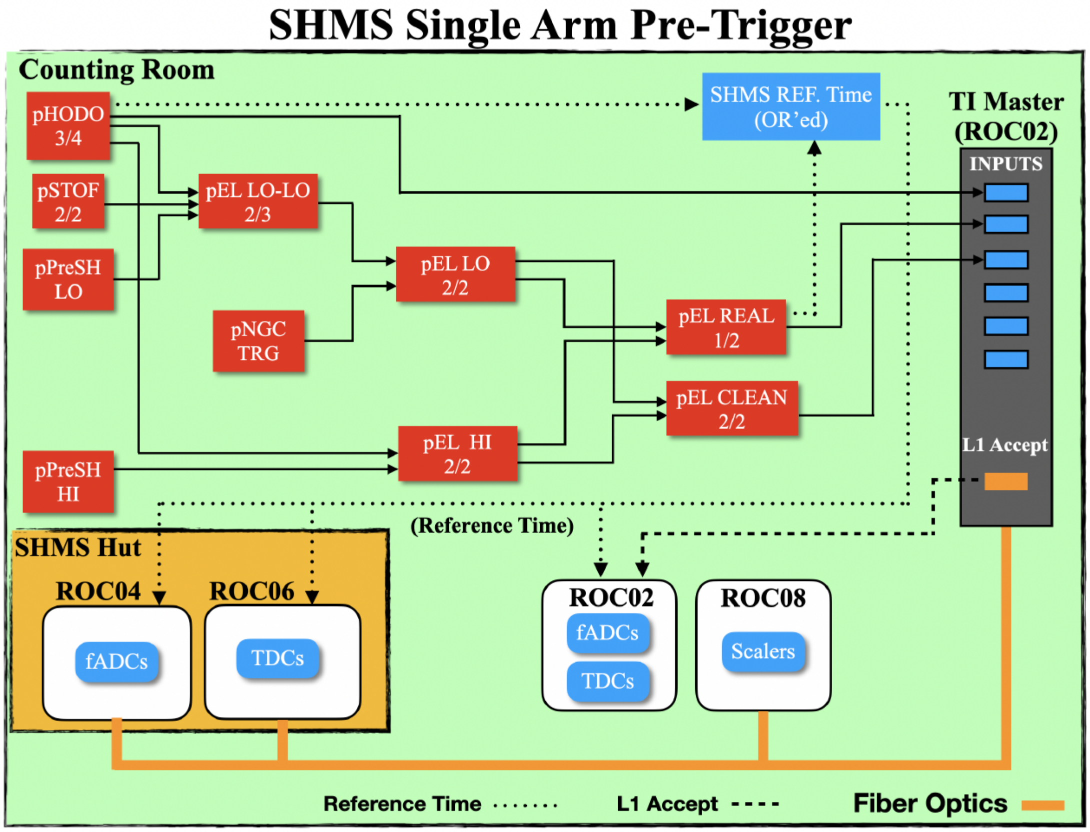

Figure 2.30: SHMS single arm pre-trigger electronics diagram [33].

2.6.3 Coincidence Trigger

In coincidence mode (see Fig. 2.31), the HMS and SHMS pre-triggers are sent to a NIM logic module where the first spectrometer pre-trigger that arrives will open a coincidence time window during which the second spectrometer pre-trigger may or may not arrive in that time. This will determine whether two spectrometers' pre-triggers are correlated with the event originating at the target. If the coincidence

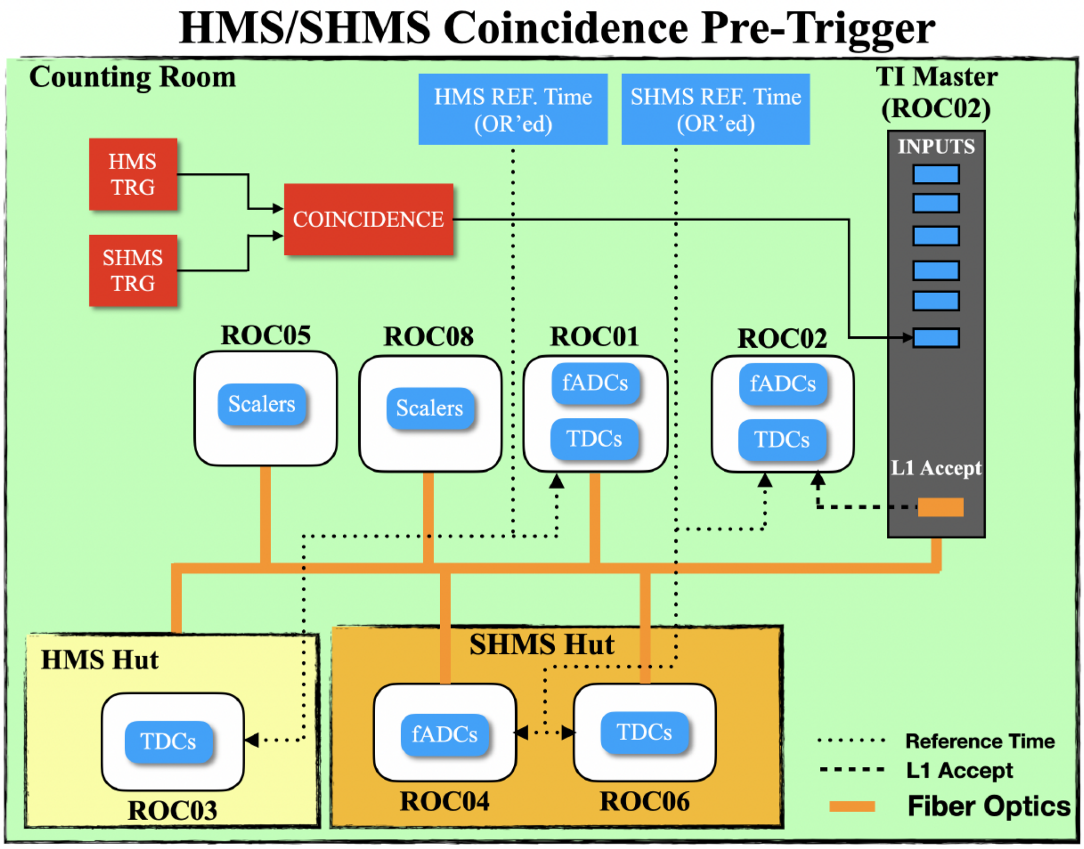

Figure 2.31: Coincidence trigger electronics diagram [33].

pre-trigger is formed, a copy is sent to scalers/TDCs, while another copy is sent to the front-end of the TI module in ROC 02 which acts as the Trigger Master (TM) in coincidence mode. Once the TM accepts the coincidence trigger, multiple copies of the L1 Accept are distributed to all HMS and SHMS ROCs (except ROC 02) via fiber optics cables in all crates for data readout. An additional copy of the L1 Accept is also sent to the front-end of the TDCs in ROC 02. Multiple copies of the HMS/SHMS pre-triggers (reference times) are also distributed to their respective spectrometer ROCs with fADC/TDC modules to function as a reference time associated with the coincidence trigger.

2.6.4 EDTM Trigger

The Electronic Dead Time Monitor (EDTM) system serves to quantify the total dead time of the DAQ system. This method involves introducing controlled pulses with a fixed frequency as close as feasible to the detectors constituting the trigger. While the ideal scenario would be to inject EDTM pulses at the detector level in the hut, where both the actual physics and EDTM signals pass through the same electronics, practical considerations dictate the injection at the trigger logic level in the Counting Room.

The EDTM, by design, functions as a legitimate trigger according to the electronics and readout systems. As the EDTM is somewhat intrusive to the trigger

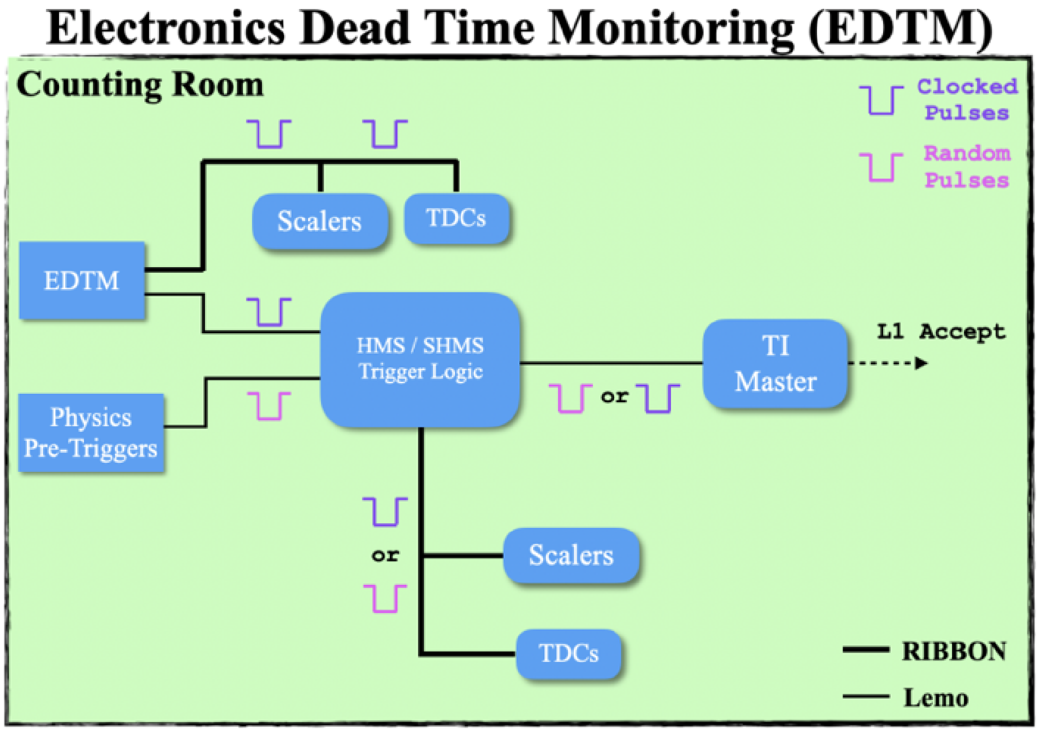

Figure 2.32: EDTM electronics diagram [33].

electronics, its frequency is carefully chosen to be small enough to minimize the likelihood of impeding genuine physics triggers yet large enough to accumulate sufficient statistics for a precise dead time measurement throughout a run. In Figure 2.32, a simplified diagram illustrates the distribution of EDTM signals through the trigger electronics. The EDTM logic signals (depicted in purple) are injected into the trigger logic, where they interact with physics pre-triggers (illustrated in magenta). A separate copy of the EDTM is directed to scalers/TDCs for incorporation into the dead time calculation. If the EDTM successfully reaches the front-end of the Trigger

Interface (TI) module and obtains acceptance (L1 Accept), it effectively measures both electronics and computer dead time.

2.7 Kaon-LT Experiment (E12-09-011)

The Kaon-LT experiment (E12-09-011) [45], one of the commissioning experiments after 12 GeV upgrade in Hall C, collected data during Autumn 2018 - Spring 2019. This experiment was originally designed to study the exclusive Kaon electroproduction reaction, $p(e, e'K^+)\Lambda$. Since the SHMS used a open trigger of a positively charged hadron, all the physics data include a number of different processes. All of these data are known as physics data. During the physics data taking, dedicated data were taken on the aluminium target at each experimental configuration. These data are then used to subtract the contribution of aluminium walls around the liquid hydrogen target. In addition to physics data, a large amount of calibration data was collected. These data allowed numerous studies to understand the performance of electron beam, targets, spectrometer magnets and detectors.

2.7.1 Calibration Datasets

The calibration data were taken at different kinematics to cover a wide range of physics data. These data mainly consist of simple elastic scattering reactions taken with different configurations. In the elastic reaction, the electron beam interacts with a proton target (in liquid hydrogen target) and the final state consists of a scattered electron and proton as shown in Fig. 2.33. There are two types of elastic scattering reactions, which provide independent measurements for the performance of a variety of experimental apparatus. The singles elastics scattering reaction $p(e, e')p$ allows the study of electron reconstruction and efficiency in each spectrometer independently. In this reaction, scattered electrons transport through one of the spectrometers in Hall C whereas protons are not detected directly and are instead reconstructed through conservation of energy and momentum. These data are taken using singles triggers for each spectrometer.

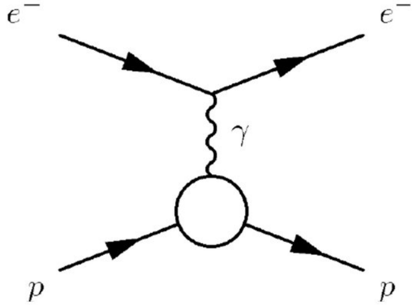

Figure 2.33: Feynman diagram for the e-p elastic scattering reaction.

The other elastic scattering reaction is known as elastic coincidence (or coin) reaction, where an electron is scattered from the proton target and both the scattered electron and proton are detected in the HMS and SHMS respectively within the resolution coincidence time. During the Kaon-LT experiment, data for the elastic scattering reaction were taken at comparable kinematics using same trigger and detector configuration as used in physics data. The cross-section of this reaction has already been measured to a very high precision and reproducing that cross-section accurately will lead to improved understanding of all the spectrometer acceptance, offsets and detector performance. This is known as Heep elastic coin study, referring to the reaction, $H(e, e'\, p)$. Table 2.8 shows all the Heep coin data taken during the the Kaon-LT experiment. The kinematics settings listed are before experimental offsets. A detailed description of Heep coin study is provided in Chapter 4.

E_b (GeV)	$Q^2(GeV^2)$	P_{SHMS} (GeV/c)	P_{HMS} (GeV/c)	$\theta_{SHMS}(^\circ)$	$\theta_{HMS}(^\circ)$
10.585	7.3	4.840	6.590	26.14	18.84
8.209	6.5	4.672	4.371	23.99	25.78
6.190	4.8	3.486	3.571	28.56	27.27
4.932	3.4	2.583	3.124	33.50	27.15
3.835	3.4	2.583	2.026	29.30	38.60

Table 2.8: Kinematic settings for all Heep coin data from the Kaon-LT experiment.

Luminosity data is another type of singles calibration data which allowed the study of rate dependent effects (tracking, DAQ live times, liquid target boiling etc) using scattered electrons in each spectrometer. These data were collected using Deep Inelastic Scattering kinematics, which provide data spread across the entire focal plane. A wide range of beam currents are used to allow study of rate dependent effects. There were separate data collected using a liquid hydrogen target and solid carbon target. The carbon target doesn't exhibit boiling, therefore these data are used to study electron live time and tracking for both spectrometers. The boiling effects for the liquid hydrogen target are then studied and a correction factor is calculated. A detailed description of the luminosity study is provided in Chapter 3. The focal plane detectors are calibrated using the physics data and this work was completed by other members of the collaboration. A detailed description of focal plane detector calibration is available in Appendix B.

2.7.2 Physics Kinematics

During the Kaon-LT experiment, the physics data were collected at a wide range of kinematics (Q^2, W). For each kinematic setting, data were collected at two values of ϵ (using different electron beam energies). For the high ϵ data, there were three SHMS angle settings corresponding to rge center setting (parallel to the q-vector) and three degrees either side for left and right setting. This configuration allows full azimuthal angle (ϕ) coverage. For the low ϵ setting, there were two SHMS angles settings corresponding to the center setting and left setting. The right setting is inaccessible because of the experimental constraints (the SHMS would run into beamline for most of the lower angle settings listed in Table 2.9). Fig. 2.34 shows the t and ϕ coverage for one of the kinematic settings from the high ϵ data.

In addition to the exclusive kaon electroproduction reaction, the experiment also gathered high statistics exclusive $p(e, e'\pi^+)n$ reaction data, as it is one of the background reactions for exclusive kaons. This is because the pion exclusive electroproduction reaction cross-section is $\approx 10\times$ higher than the kaon exclusive electroproduction

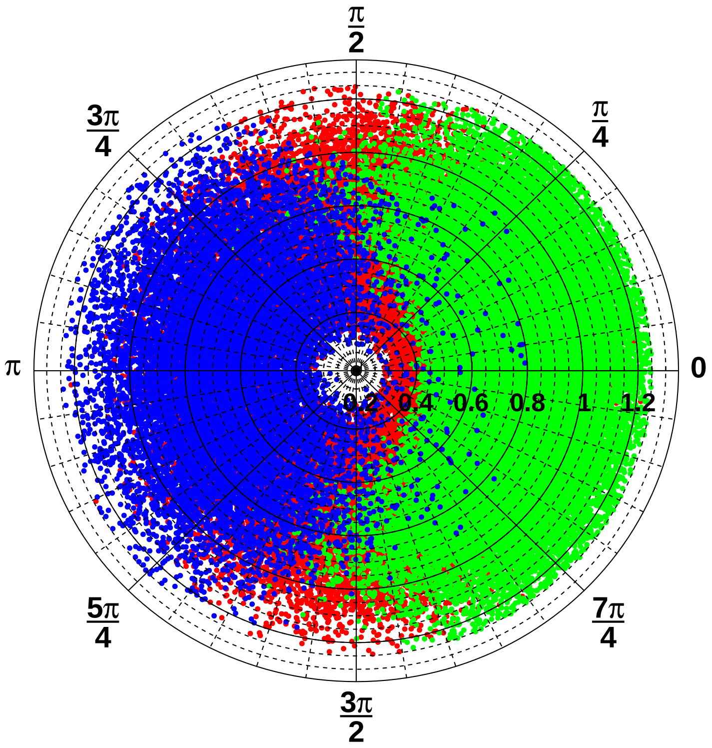

Figure 2.34: A two dimensional distribution of $-t$ (radial axis) and ϕ (azimuthal axis) for $Q^2 = 4.4$ GeV^2. The three colors correspond to three SHMS ϕ settings. The blue data correspond to SHMS left setting, red data correspond to SHMS center setting and green data correspond to SHMS right data.

reaction cross-section. This thesis is focused on studying the pion exclusive reaction at $Q^2 > 2.0\ GeV^2$ for both $p(e, e^{'}\pi^{+})n$ and $p(e, e^{'}\pi^{+})\Delta^{0}$. The data were collected at two values of ϵ while keeping the other kinematics constant. This is done by taking data at different beam energies. Table 2.9 lists all the data collected during the Kaon-LT experiment. The kinematic settings listed are before experimental offsets. The data gathered at 10.6 GeV corresponds to high ϵ, whereas 6.2 and 8.2 GeV corresponds to low ϵ at the same kinematics. For the beam spin asymmetry analysis, only the 10.6 GeV data were analyzed because only these data have a full azimuthal coverage needed for the determination of the beam spin asymmetry.

E_b(GeV)	ϵ	P_{HMS}	θ_{HMS}	P_{SHMS}	θ^{center}_{SHMS}	θ^{left}_{SHMS}	θ^{right}_{SHMS}
$Q^2 = 5.5$ (GeV^2), W = 3.02 (GeV)							
10.585	0.53	3,266	23.00	6.842	9.56	12.56	6.56
8.209	0.18	0.962	49.31	6.755	6.20	8.50	-
$Q^2 = 4.4$ (GeV^2), W = 2.74 (GeV)							
10.585	0.72	4.712	17.08	5.389	12.81	15.81	9.81
8.209	0.48	2.328	27.77	5.389	10.01	13.01	-
$Q^2 = 3.0$ (GeV^2), W = 2.32 (GeV)							
10.585	0.88	6.590	11.90	3.486	18.18	21.18	15.18
6.190	0.57	2.185	27.25	3.486	13.28	16.28	-
$Q^2 = 3.0$ (GeV^2), W = 3.14 (GeV)							
10.585	0.67	4.204	14.91	6.053	9.42	12.42	6.5
8.209	0.39	1.821	25.89	6.053	6.91	9.91	-
$Q^2 = 2.1$ (GeV^2), W = 2.95 (GeV)							
10.585	0.79	5.292	11.15	4.983	10.74	13.74	7.74
6.190	0.25	0.888	36.15	4.983	6.20	8.48	-
$Q^2 = 0.5$ (GeV^2), W = 2.40 (GeV)							
4.932	0.70	2.066	12.71	2.583	8.86	11.86	6.00
3.835	0.45	0.968	21.14	2.583	6.79	9.79	-

Table 2.9: Detailed breakdown of Kaon-LT kinematics settings

Chapter 3

Data Analysis

The data collected during the Kaon-LT experiment is analyzed by using the Hall C analyzer (hcana) [46] and CERN ROOT [47] which is a software framework developed by CERN for nuclear and particle physics. The ROOT framework consists of a set of libraries and tools that enable analysis of large datasets. This chapter gives a brief introduction of the Hall C data analysis framework, a description of event reconstruction via track, position, angle and momentum reconstruction. This is followed by a detailed outline of calculation of correction factors including live times and efficiencies. The rate dependent luminosity study (performed by members of our collaboration) is described for completeness. Finally, the event selection and particle identification method is outlined focusing on the exclusive pion electroproduction reaction.

3.1 Overview of Hall C Analyzer

The Hall C analysis software [46] is an object-oriented C++ package which is based on the Hall A analysis software "podd" [48]. The hcana software provides access to CERN ROOT's [47] analysis and visualization capabilities, along with specialized classes tailored for Hall C detectors and physics analyses. The event decoder in hcana is fully compatible with the CODA raw data event format. It also enables users to access spectrometer, detector, and physics analysis results through "global" variables. hcana can access and analyse scaler and EPICS data, in addition to spectrometer data. The raw data files are processed, or "replayed", using hcana in conjunction with the Hall C replay directory. This directory contains a framework specifically designed to assist with event reconstruction in the Hall C spectrometers, ultimately generating the final ROOT file format. The Hall C replay directory includes various configuration files, which store parameters related to detectors, spectrometers, beams, and targets. It also contains definition files that specify which global variables or blocks of variables will be written to a ROOT file and which histograms should be saved in the ROOT file. Details about the Hall C replay infrastructure are available in [33]. After the replay process is completed, the data stored in the ROOT files and/or report files can be utilized for further analysis.

3.2 Event Reconstruction

In order to measure the meson electroproduction cross-section, the vertex reconstruction of scattered particles in both spectrometers is needed. This is a multi-step process in the Hall C analysis framework (hcana). This starts with the hit information from drift chambers. The tracks are reconstructed by combining these hits through an algorithm. The spatial and momentum quantities are reconstructed for the good tracks using particle identification and timing information. The focal plane quantities are then reconstructed for good tracks. Finally, the target quantities are reconstructed by transporting focal plane quantities back to the target using matrix transformation.

3.2.1 Track reconstruction

Each spectrometer consists of a pair of chambers with six planes of wires in each chamber (as shown in Fig. 2.20). Tracks are identified in the drift chambers through a complex algorithm. First, a hit is detected as a signal from the drift time in the sense wires. Hits in unlike planes are combined to create a combo. A cluster of combos is then combined, which is known as spacepoint. Combos within a specific radius are considered to be one spacepoint. Spacepoints from different planes are then combined to form a stub. The stubs from two chambers are linked together to form a track. Events with more than one track require a golden track selection. A golden track is the best track in a multi-track event which can selected through one of the following methods:

- χ^2 **Minimization:** This is the simplest method for the selection of golden tracks. This is a statistical process where χ^2 of each track is calculated using the known quantities from track reconstruction and the track with lowest χ^2 is selected as a golden track.
- **Scintillator Method:** In this method, additional information from hodoscope planes is used for the golden track selection. For events with more than one track, the S2Y plane is checked and the track with the closest hit in this plane is selected. In the case of no hit in S2Y, the track with closest hit in the S2X hodoscope plane is used. If there is still more than one track, the golden track is selected by χ^2 minimization.
- **Prune Method:** This is the most sophisticated method for the golden track selection. In this method, pruning cuts are applied on reconstructed target quantities (X'_{tar}, Y'_{tar}, Y_{tar}), momentum spread (δ) and the check on the particle exiting the final dipole (dipoleexit), Time-of-Flight of particles (ToF), the speed of particles (β), hit in second pair of hodoscope planes (S2X+S2Y), number of PMT hits for each track, number of degrees of freedom (dof) on track χ^2 and focal plane time relative to nominal time. The track with lowest values for these

quantities is then selected as the golden track. If there is still more than one track then χ^2 minimization is used.

3.2.2 Focal Plane reconstruction

The focal plane is a virtual plane located between the two drift chambers. The focusing magnets in each spectrometer are configured to focus the scattered particles to this focal plane. The focal plane quantities are reconstructed from the track position information. The X_{fp} and Y_{fp} are vertical and horizontal positions respectively perpendicular to the direction of motion of particles. The $X_{fp}^{'}$ and $Y_{fp}^{'}$ are the vertical and horizontal slopes (dx/dy and dy/dz) of the tracks.

3.2.3 Momentum and Target reconstruction

After the track reconstruction and focal plane reconstruction, the next step is to reconstruct the target quantities. These quantities are calculated using the focal plane variables and the path length of the particle from the focal plane back to the target chamber. It is important to mention that the target variables for each spectrometer are calculated separately. The X_{tar} is the out of plane position calculated from beam position measurements whereas $(X_{tar}^{'}, Y_{tar}, Y_{tar}^{'}, \delta)$ are calculated by transporting $(X_{fp}, X_{fp}^{'}, Y_{fp}, Y_{fp}^{'}, X_{tar})$ using an optical matrix (M). The $X_{tar}^{'}$ is the out-of-plane scattering angle, $Y_{tar}^{'}$ and Y_{tar} are in-plane scattering angle and position respectively. δ is the fractional momentum deviation from the central momentum which can be calculated as follows:

$$\delta = \frac{P_{particle} - P_{central}}{P_{central}} \times 100 \qquad (3.15)$$

3.3 Particle Identification (PID)

An important part of data analysis is to precisely select specific particles in each spectrometer. A detailed study has been done for particle identification in each spectrometer for all Kaon-LT data to select exclusive pion electroproduction data. The acceptance range is selected based on global cuts (cuts to select well understood phase space for each spectrometer) for each spectrometer in Hall C. These cuts were determined after a dedicated study completed during the commissioning of HMS-SHMS installation in Hall C. More details are available in [33]. An accurate particle identification is critical for detector efficiencies and yield calculations.

3.3.1 Electron ID

In the HMS, electrons are selected using the gas Cherenkov and electromagnetic calorimeter. At lower momentum, the π^- background is larger, so the Cherenkov is more important for eliminating the pions. At larger momentum, where pions will start to fire the Cherenkov, the pion fraction is smaller and calorimeter is more important for pion background suppression. This can be observed through a two dimensional distribution of normalized HMS calorimeter energy and number of photoelectrons in the gas Cherenkov as shown in Fig. 3.1. Table 3.1 lists both acceptance and particle ID cuts used for electron selection.

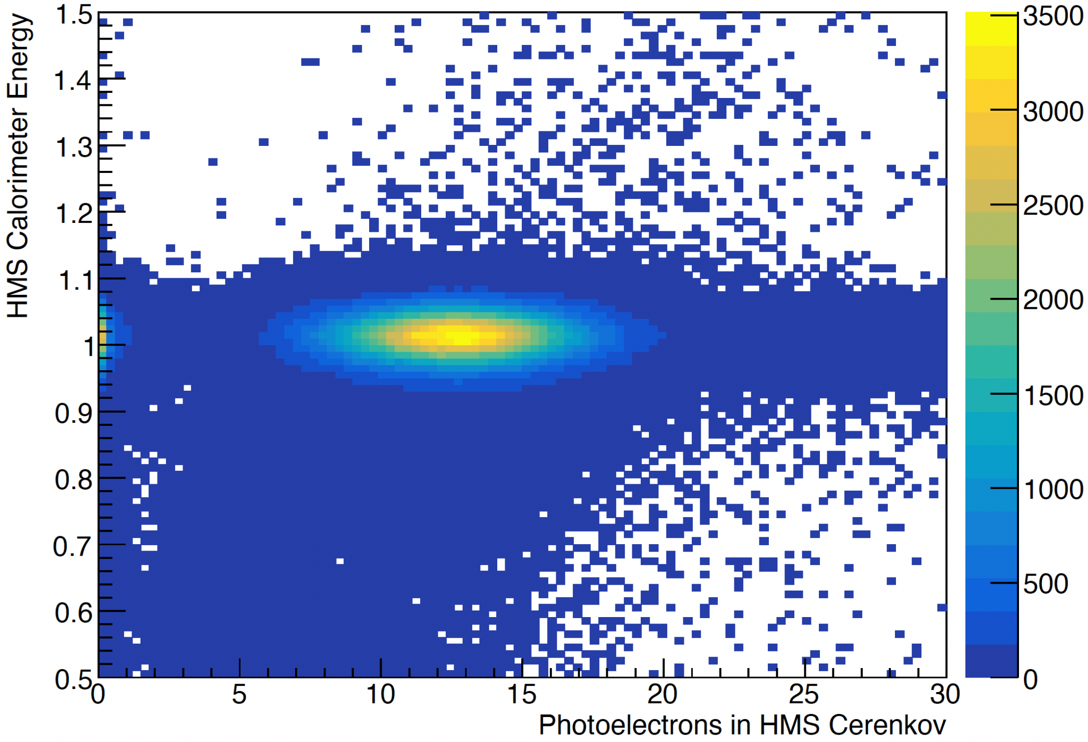

Figure 3.1: Distribution for particle identification of electrons in the HMS for the Kaon-LT experiment. The large number of events in the middle correspond to electrons, whereas the small number of events in the bottom left correspond to π^-.

Cut Type	Cut value
Acceptance (X'_{fp})	$-0.08 < H.gtr.th < 0.08$
Acceptance (Y'_{fp})	$-0.045 < H.gtr.ph < 0.045$
Acceptance (δ)	$-8 < H.gtr.dp < 8$
PID (Gas Cherenkov)	$H.cer.npeSum > 2.0$
PID (Calorimeter)	$H.cal.etottracknorm > 0.7$

Table 3.1: Cuts used for electron selection in the HMS in Kaon-LT experiment.

3.3.2 Pion ID

In the SHMS, pions are selected using the heavy gas Cherenkov and aerogel Cherenkov. These two detectors are threshold Cherenkov detectors and they are configured to have pions producing Cherenkov light signals in both detectors as described in Section 2.5.3. A two dimensional distribution of number of photoelectrons in the heavy gas Cherenkov and aerogel Cherenkov can be seen in Fig. 3.2. For the $p(e, e'\pi^+)n$ reaction, a cut on the aerogel Cherenkov is sufficient because the neutron missing mass distribution has minimal background from other processes (as discussed in Section 3.8.2) and Λ or Σ baryon events from the kaon electroproduction reaction do not contaminate the pion sample. This eliminates any loss of events from inefficiency of the heavy gas Cherenkov and therefore reduces systematic uncertainties.

On the other hand, cuts on both detectors are needed to select a clean sample of pions for the $p(e,e^{'}\pi^{+})\Delta^{0}$ reaction. This eliminates contamination from the exclusive kaon electroproduction reactions which populate the same missing mass region as Δ^{0} events. Table 3.2 lists both acceptance and particle ID cuts used for pion selection.

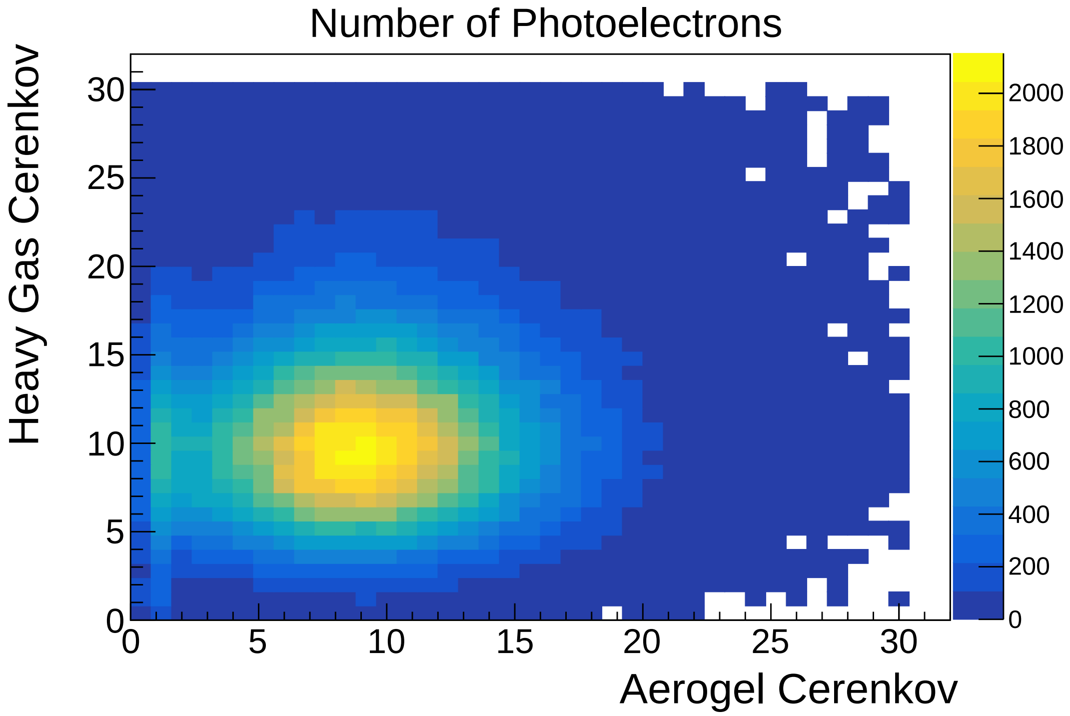

Figure 3.2: Distribution of number of photoelectrons from Heavy Gas Cherenkov and Aerogel Cherenkov for pions selection in the SHMS for the Kaon-LT experiment. The large number of events at NPE > 2.0 correspond to π^{+} events.

Cut Type	Cut value
Acceptance (X'_{fp})	$abs\|P.gtr.th\| \ < \ 0.06$
Acceptance (Y'_{fp})	$abs\|P.gtr.ph\| \ < \ 0.04$
Acceptance (δ)	$-10 \ < \ P.gtr.dp \ < \ 20$
PID (Aerogel)	$P.aero.npeSum \ > \ 3.0$
PID (Heavy Gas)	$P.hgcer.npeSum \ > \ 2.0$

Table 3.2: Cuts used for pion selection in the SHMS in the Kaon-LT experiment.

3.4 Live Times

The CPU live time is the time in which DAQ is actively recording data and this should be high in order to record all of the physics data. The electronic dead time monitor (EDTM) is a measure of the total live time (CPU live time as well as electronic live time) as discussed in Section 2.6.4. The CPU live time and the EDTM live time are given by:

$$\text{CPU Live Time} = \frac{\text{No. of COIN triggers Recorded}}{\text{No. of COIN triggers Received}} \tag{3.16}$$

where COIN is a coincidence trigger as described in Section 2.6.3.

$$\text{EDTM Live Time} = \frac{\text{No. of EDTM triggers Recorded}}{\text{No. of EDTM triggers Sent}} \tag{3.17}$$

The EDTM system was only installed as part of the 12 GeV upgrade of Hall C and the reliability of this system needs to be established before using this for the normalization of the experimental yields. A simple way to do this is by comparing the EDTM live times with the CPU live times over a wide range of trigger rates. We expect the electronic live time (ELT) to be very high, so if the EDTM live time and the CPULT are both accurate measures of the true DAQ livetime, they should track each other very closely.

Figures 3.3 and 3.4 show the comparison between the two live times. It can be seen that both live times drop significantly after 2 kHz. This is due to the data

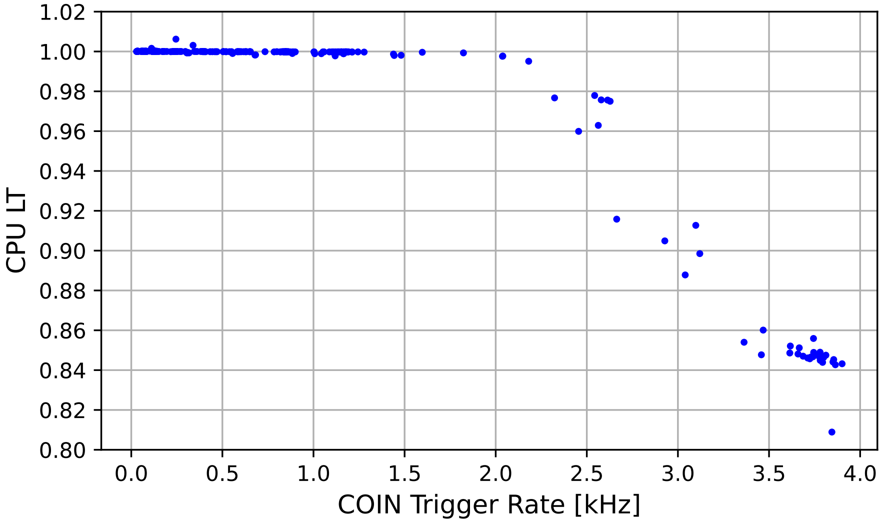

Figure 3.3: Measurement of CPU live time with respect to the coincidence trigger rate during the Kaon-LT experiment.

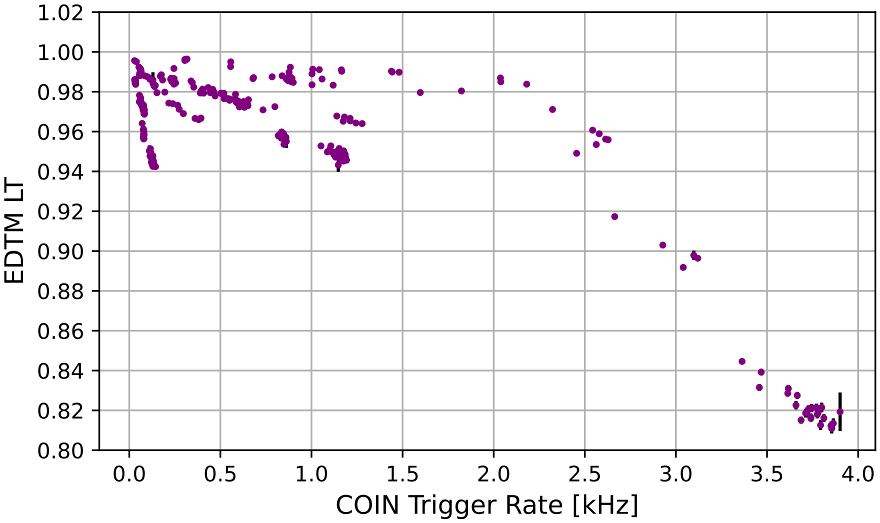

Figure 3.4: Measurement of EDTM live time with respect to the coincidence trigger rate during the Kaon-LT experiment.

buffer being filled, resulting in the DAQ being busy and therefore losing events as rate increases. This follows the expected trend based on the DAQ properties. At lower rate, the CPU live time is high and stable. On the other hand, the EDTM live time shows multiple trends at lower rate and gives lower values of live time. This implies that the EDTM may not be reliable for the commissioning experiments. A possible source for this unreliability can be the configuration of EDTM triggers which were manually set by the shift takers and the number of EDTM triggers sent into the DAQ varied for each dataset. Additionally, EDTM cab give incorrect values for datasets where the beam-off period was large. These results helped in improving the EDTM systems for later experiments in Hall C and the EDTM trigger rate was subsequently automated in the DAQ system. To estimate the total live time in Kaon-LT experiment, an alternate method was used. In this method, electronic dead time is estimated using the total DAQ rate for each run and the hodoscope pre-trigger gate width (fixed at 55 ns) as follows:

$$\mathrm{ELT_{total}} = \mathrm{ELT_{HMS}} \times \mathrm{ELT_{SHMS}} \tag{3.18}$$

where

$$\mathrm{ELT_{HMS}} = 1 - (55\ \mathrm{ns} \times \mathrm{HMS\ rate}) \tag{3.19}$$

$$\mathrm{ELT_{SHMS}} = 1 - (55\ \mathrm{ns} \times \mathrm{SHMS\ rate}) \tag{3.20}$$

The total live time is then calculated by multiplying the CPU live time and electronic live time as follows:

$$\mathrm{TLT} = \mathrm{ELT} \times \mathrm{CPULT} \tag{3.21}$$

3.5 Detector Efficiencies

Each detector in both spectrometers has a specific role in the experiment. These detectors are designed to enable high precision measurements and should give high efficiency over a wide range of experiment conditions. However, there are still some inefficiencies in each detector. In particular, the SHMS focal plane detectors are brand new and are exposed to demanding conditions (high rates and multiple particle types).

Kaon-LT was a commissioning experiment and significant work has been done to understand and commission the focal plane detectors. A dedicated efficiency study for each detector in both spectrometers was performed to estimate the correction factors. These correction factors can later be used to normalize the experimental yield.

3.5.1 Tracking Efficiency

The tracking efficiency is defined as the ratio of tracks found in drift chambers (tracking detector) and the track candidates from all the other detectors as shown in Eq. 3.22. First, a track candidate is defined by using other detectors (hodoscopes, PID detectors) and then a check was done to confirm that the track passed through the two drift chambers.

$$\epsilon_{tracking} = \frac{N_{Did}}{N_{Should}} \tag{3.22}$$

where

$$N_{Did} = N_{Should} \,\&\, N_{Trk} \tag{3.23}$$

and

$$N_{Should} = N_{Trig} \,\&\, N_{PID}. \tag{3.24}$$

Here

- N_{Trig} → No. of Triggered events

- N_{PID} → No. of events after PID cuts

- N_{Trk} → No. of events with tracks in Drift Chamber

As discussed in Section 3.2.1, track reconstruction is done using a number of parameters. A detailed track parameter optimization study was performed to improve the track identification parameters. Fig. 3.5 shows one of the parameters which has the most effect on the tracking efficiency. This track parameter restricts the maximum number of hits in each chamber per event in the track finding algorithm. Previously, this number was set to 25 hits in each chamber, but results indicated that increasing the limit to 35 hits in each chamber greatly improves the tracking efficiency (by 2-8%),

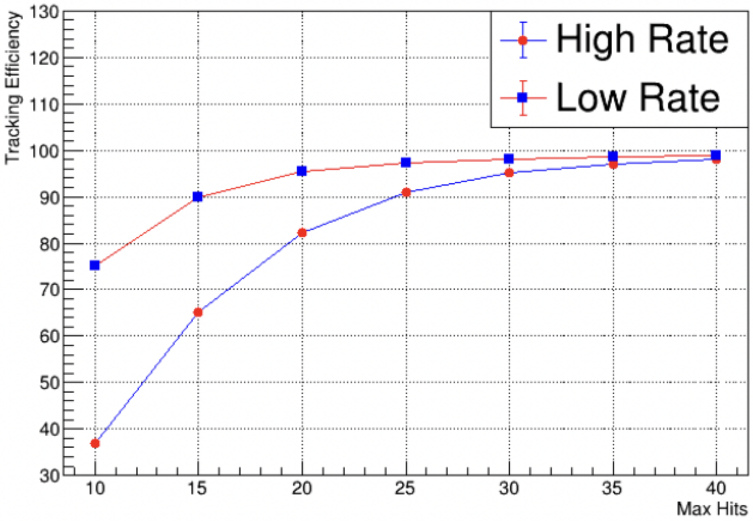

Figure 3.5: Measurement of SHMS tracking efficiency with respect to maximum hits parameter in the drift chambers for two run numbers with low and high rate at same kinematics.

especially for high rate runs. The other variable that was optimized is the criterion to select the radius of a cluster of hits (spacepoint). This variable was previously set to 1.2 cm for each chamber, but now it has been improved to 0.9 cm for each chamber restricting to a smaller spacepoint. This improvement is complementary to the modification of maximum hits, as a higher number of hits result in more spacepoints and therefore require a smaller radius. During the track parameter optimisation study, tests were performed for each track selection parameter, but only these two parameters were found to improve the tracking efficiency. A detailed description of all track parameters and comparison of old and new values can be found in [49].

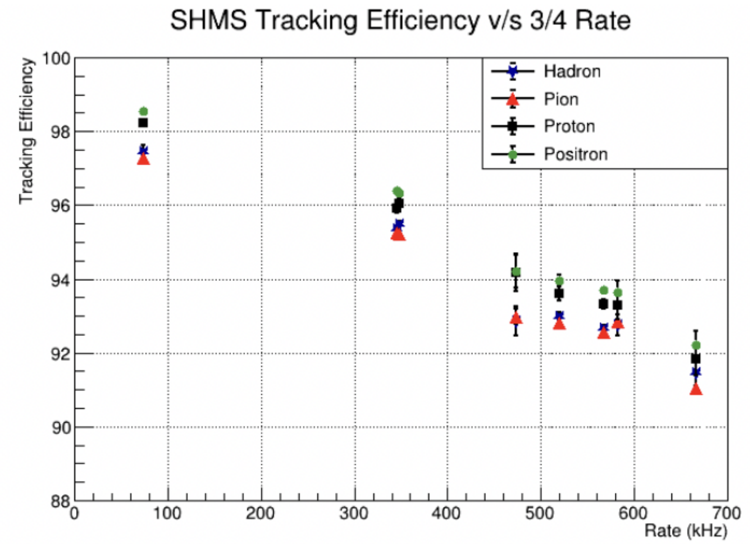

Figure 3.6: Measurement of SHMS tracking efficiency before track parameter optimization with respect to the 3/4 trigger rate for a current scan during the Kaon-LT experiment.

Fig. 3.6 shows the tracking efficiency with respect to trigger rate at a specific kinematics before any optimisation. It can be observed that the tracking efficiency drops 9.5% for 1 MHz change in rate (SHMS 3/4 trigger rate) for each particle type. Different particles are selected using tight particle identification (PID) selection criteria from different focal plane detectors in the SHMS. Fig. 3.7 shows the results after the track parameter optimization study. It can be concluded that the tracking efficiency has been improved for all particle types, especially in high rate runs. The efficiency slope shows only a 2.5% drop for a 1 MHz rate change with the new track parameters. The final step in this study is to verify that there is no rate dependence on the normalized yield from tracking efficiency. This is done in the luminosity study,

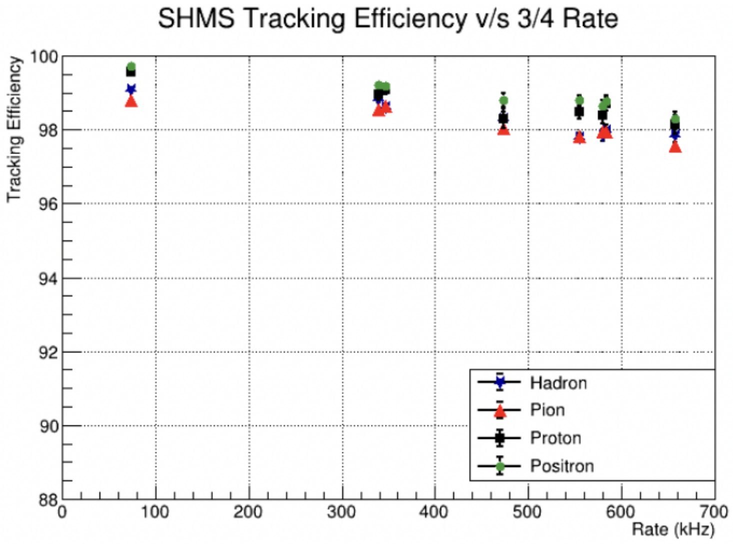

Figure 3.7: Measurement of SHMS tracking efficiency after track parameter optimization with respect to the 3/4 trigger rate for the same dataset.

which is described in the next section. The tracking efficiency for pions in the SHMS is then calculated for all data collected during the Kaon-LT experiment.

Fig. 3.8 shows the final pion tracking efficiency with respect to SHMS trigger rate. It can be observed that the efficiency has larger scatter, as well as 2% drop, as compared at higher rates in Fig. 3.7. The scatter is due to the background rate (particles other than π^+) changing with spectrometer central momentum and angle. The overall drop in efficiency is due to the change in particle selection criteria from

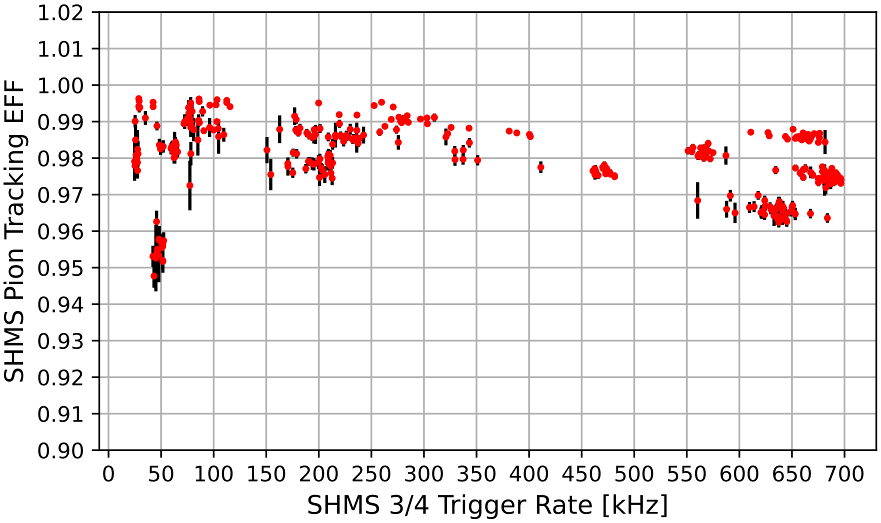

Figure 3.8: Final results of SHMS tracking efficiency with respect to trigger rate for high energy data collected during Kaon-LT experiment. The different efficiency values at similar rates is due to change in experimental conditions (spectrometer angle, signal-to-background rates).

different detectors. The PID cuts used for this tracking efficiency are wider than the tight cuts used during the track parameter optimization study. These selection criteria are identical to the selection cuts used for physics analysis as described in Section 3.3.

The tracking efficiency for electrons in the HMS follows the same procedure as used for pions in the SHMS. The rates in HMS are significantly lower than the rates in the SHMS, because the HMS cannot access as small angles as the SHMS. In addition, the signal-to-background ratio is high in the HMS due to accurate electron identification. This means that the electron tracking efficiency doesn't require a dedicated track

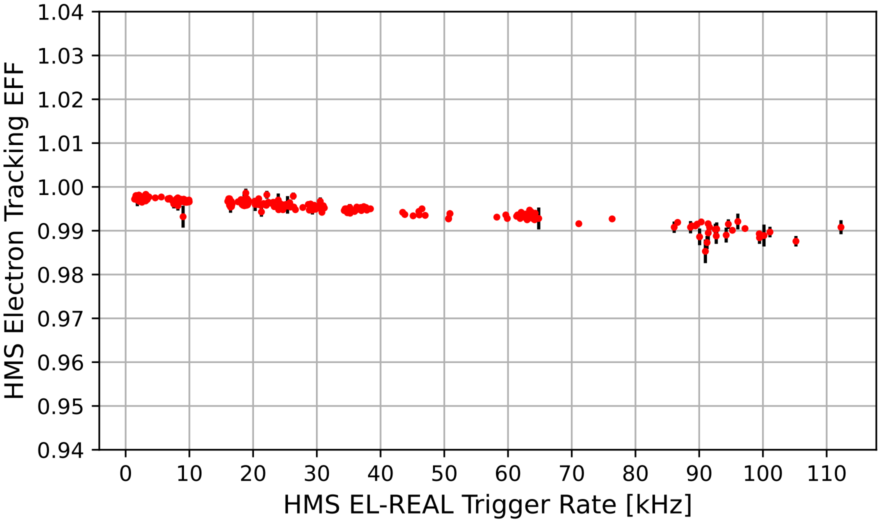

Figure 3.9: Final results of HMS electron tracking efficiency with respect to trigger rate for high energy data collected during Kaon-LT experiment.

parameter optimization study. Fig. 3.9 shows the electron tracking efficiency for high energy (10.6 GeV) physics data collected during Kaon-LT experiment with respect to trigger rate. It can be observed that the electron tracking efficiency is high and stable over a wide range of rates. Both pion and electron tracking efficiency are used to normalize experimental yields on a run-by-run basis. However, this efficiency cancels out in the ratio for the polarized cross-section calculated through beam spin asymmetry provided the rate difference in two helicities is small.

3.5.2 Hodoscope Efficiency

As described in Section 2.6, the trigger system in Hall C relies on hodoscopes in both spectrometers. This means in order to determine a trigger efficiency, an estimate of hodoscope efficiency is required. During the Kaon-LT experiment, the SHMS used hodoscope- 3/4 trigger and HMS used ELREAL trigger. Since the calorimeter efficiency is independently determined for the HMS, the combination of 3/4 hodoscope efficiency and PID detectors' (Cherenkov and calorimeter) efficiency will provide a trigger efficiency. The single hodoscope plane efficiency in both spectrometers uses an analogous procedure. This efficiency is calculated as follows:

$$\epsilon_{Hodo} = \frac{\mathrm{N_{Tracks}} \ \& \ \mathrm{N_{scin}}}{\mathrm{N_{Tracks}}} \tag{3.25}$$

where

- N_{Tracks} corresponds to number of events with good tracks.

- N_{scin} corresponds to number of events with hits in a given hodoscope plane.

Once efficiency for each hodoscope plane is determined, the 3/4 efficiency is calculated via probability.

Figures 3.10 and 3.11 shows the hodoscope 3/4 efficiency for HMS and SHMS with respect to singles trigger rate. The results for both spectrometers show similar trends as the tracking efficiency. The HMS 3/4 hodoscope efficiency is very stable and high over a wide range of trigger rates, similar to the HMS electron tracking efficiency, due to low background rates in the HMS. On the other hand, the SHMS hodoscope 3/4

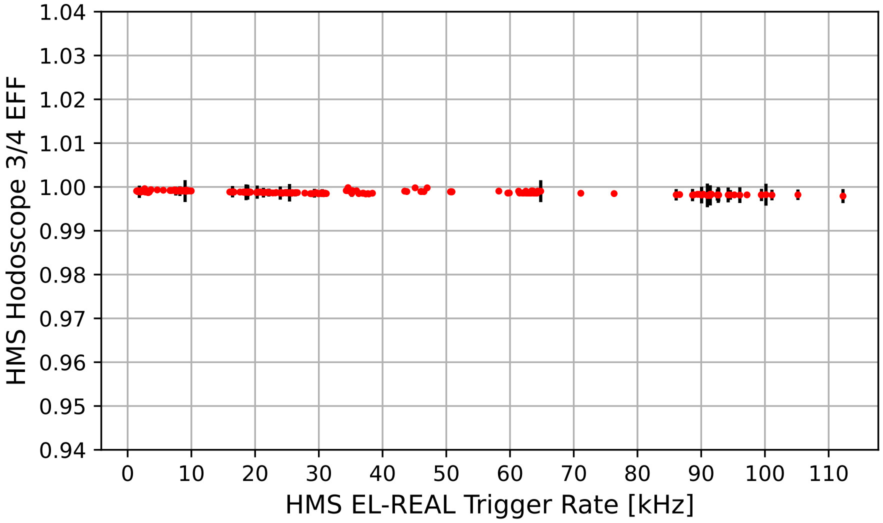

Figure 3.10: Measurement of HMS hodoscope efficiency with respect to the trigger rate for high energy data collected during Kaon-LT experiment.

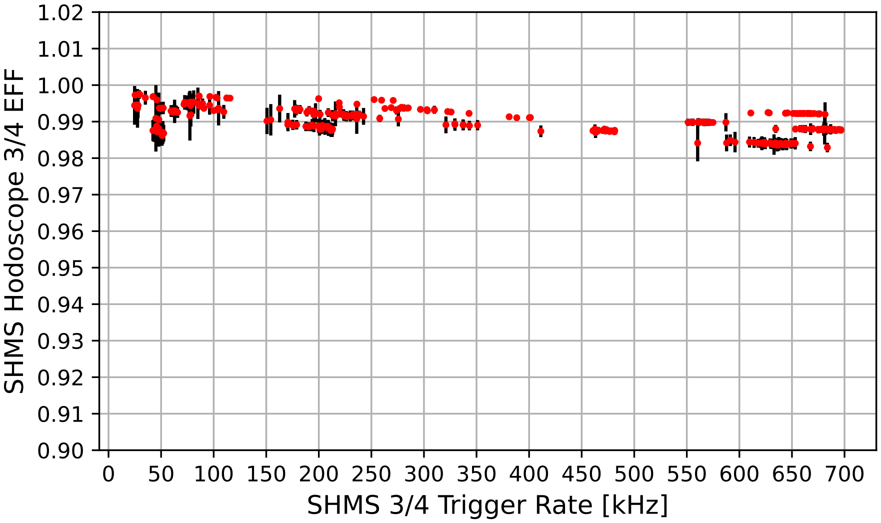

Figure 3.11: Measurement of SHMS hodoscope efficiency with respect to the trigger rate for high energy data collected during Kaon-LT experiment.

efficiency shows a small scatter (2%) similar to that of the pion tracking efficiency. The quartz plane in the SHMS is the source of the scatter and overall lower hodoscope efficiency because the particles below the Cherenkov threshold in the quartz plane do not produce any signal.

3.5.3 Cherenkov Efficiency

The threshold Cherenkov detectors are the main particle identification (PID) detectors in each spectrometer. For the efficiency study in each of HMS and SHMS, cuts are placed on the other PID detectors to define a particle type and then the

Cherenkov is checked to see if it also sees the same particle type. In the SHMS, the aerogel Cherenkov is used to separate mesons (pions and kaons) from the protons. As described in Section 2.5.3, Kaon-LT used different aerogel trays based on specific kinematics. Each aerogel tray has a different index of refraction, which means that the threshold momentum is different to produce Cherenkov light. The aerogel efficiency for pions is calculated as follows:

$$\epsilon_{Cherenkov} = \frac{N_{Did}}{N_{Should}} \tag{3.26}$$

where

$$N_{Did} = N_{Should} \,\&\, N_{Cherenkov} \tag{3.27}$$

and

$$N_{Should} = N_{Trig^{Trk}} \,\&\, N_{Accept} \,\&\, N_{PID}. \tag{3.28}$$

Here

- N_{Trig}^{Trk} → No. of Triggered events with good tracks
- N_{Accept} → No. of events after acceptance cuts (listed in Table 3.2)
- N_{PID} → No. of events after PID cuts from other detectors
- $N_{Cherenkov}$ → No. of events with Cherenkov light signal above the cut value in Table 3.2

Fig. 3.12 shows the aerogel efficiency for pions in SHMS over a wide range of data. It can be observed that this efficiency is very stable and high. The heavy gas Cherenkov is the other particle identification detector in the SHMS. The efficiency calculation for this detector is a bit more complicated because there is an inefficient region in the middle. This is caused by the curved nature of the four mirrors (see Fig. 2.24). The level of complexity increased as the size of inefficient region changed between different run periods of Kaon-LT experiment as the mirror alignment was

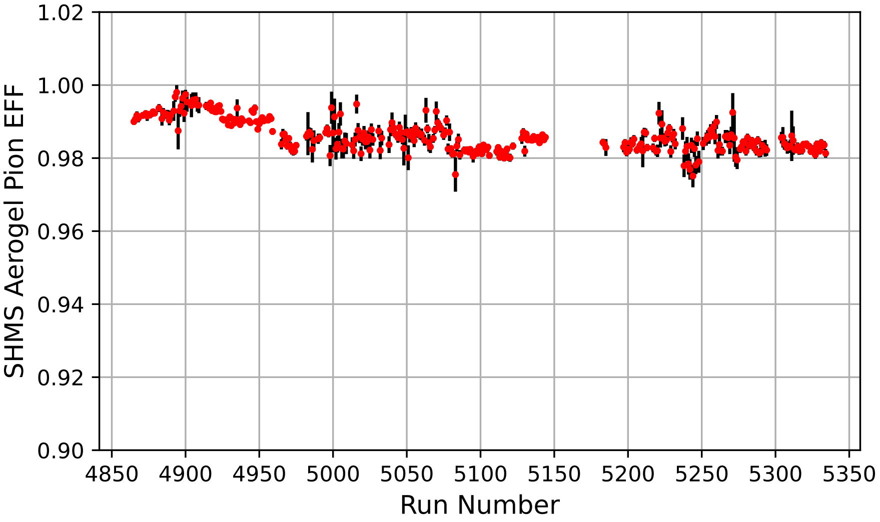

Figure 3.12: Measurement of SHMS aerogel efficiency for pions with respect to run numbers for high energy data collected during Kaon-LT experiment. The scatter in the plot is an experimental effect caused by different aerogel trays used during the experiment.

adjusted in January 2019. A multi-region efficiency study was conducted by other members of the collaboration for the HGC in the SHMS. During this study, the detector was divided into different regions based on the inefficient region. The central region, where efficiency was below 70%, was excluded from the physics analysis and the efficiency from remaining regions is used to correct the experimental yield. More details for this study are available in [50].

In the HMS, the main particle identification detectors are the gas Cherenkov detector and the calorimeter detector. Both of these detectors are used to select electrons. The gas Cherenkov efficiency in HMS used a similar procedure as used in the aerogel Cherenkov in the SHMS because the HMS gas Cherenkov has only two mirrors and does not have any inefficient region. During the efficiency study from physics data, it was observed that there's a momentum dependent π^- background as described in Section 3.3. This contamination resulted in a low apparent gas Cherenkov efficiency for electrons in the HMS. To avoid complications from the pion contamination, this efficiency was determined using an alternate dataset known as elastic singles data. This is given by reaction $p(e,e')p$, where electrons are scattered from the hydrogen target and only scattered electrons are detected in the final state. By placing a constraint on the reconstructed proton mass, the possibility of contributions from pions was eliminated. As described in Section 2.5.3, the threshold gas Cherenkov in HMS was configured with fixed gas mixture and pressure. The threshold momentum for

π^- to produce Cherenkov light in HMS was 4 GeV/c, therefore only those elastic singles data were used where the HMS momentum was below 4 GeV/c. Additionally, the dataset was selected to have high $e - \pi^-$ ratio and comparable momentum and angles to the physics data. The efficiency study was performed for six different elastic singles settings.

Fig. 3.13 shows results for the HMS gas Cherenkov electron efficiency from elastic singles dataset collected between 2-4 GeV/c momenta. It can be observed that the efficiency is stable over the specified momentum range. The actual efficiency value is 2% lower than expected value ($> 99\%$). This is because of a light leak in HMS gas Cherenkov during the commissioning experiments data taking. This was a known

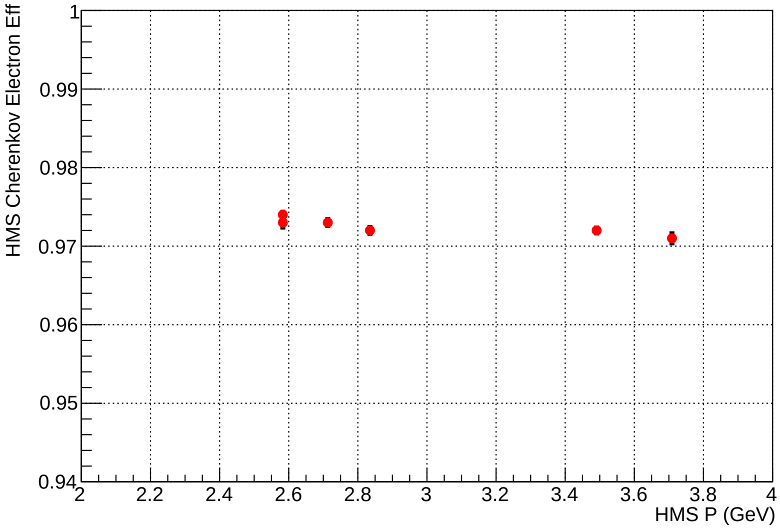

Figure 3.13: Measurement of HMS Gas Cherenkov efficiency for electrons with respect to HMS central momentum (P) from elastic singles data during Kaon-LT experiment

problem and was independently observed by other experiments as well [34]. The light leak was fixed after the completion of commissioning experiments. After the completion of this study, a fixed correction of 0.973 ± 0.001 was determined by taking the average of each efficiency and used for normalization of experimental yields. The uncertainty includes both statistical and systematic uncertainties. The statistical uncertainty is really small (≈ 0.0003) due to moderate singles rate in the HMS and the systematic uncertainty is determined using the standard deviation. It is important to mention that all Cherenkov efficiencies cancel in the ratio for the polarized cross-section calculated through the beam spin asymmetry.

3.5.4 Calorimeter Efficiency

Both spectrometers are equipped with electromagnetic calorimeters which are located at the ends of the respective detector stacks as explained in Section 2.5.4. The calorimeter is used to measure the energy of electromagnetic particles. During the Kaon-LT experiment, the HMS was used as electron arm and the SHMS was used as hadron arm. Therefore, the efficiency of calorimeter in the SHMS is not studied since hadrons do not induce significant electromagnetic showers in the calorimeter. This means the calorimeter efficiency study was only performed for the HMS. Similar to the gas Cherenkov, the calorimeter in the HMS is exposed to a large π^- background in most of the physics data. This background cannot be removed by the gas Cherenkov as π^- produce Cherenkov light above the threshold. Therefore, the calorimeter efficiency study for electrons was also conducted on the same elastic singles settings which were used for gas Cherenkov. The calorimeter efficiency was calculated as follows:

$$\epsilon_{Calorimeter} = \frac{N_{Did}}{N_{Should}} \tag{3.29}$$

where

$$N_{Did} = N_{Should} \,\&\, N_{Calorimeter} \tag{3.30}$$

and

$$N_{Should} = N_{Trig^{Trk}} \,\&\, N_{Accept} \,\&\, N_{Cherenkov}. \tag{3.31}$$

Here

- N_{Accept} → No. of events after acceptance cuts (listed in Table 3.1)
- $N_{Cherenkov}$ → No. of events with Cherenkov light above the cut value in Table 3.1
- $N_{Calorimeter}$ → No. of events with calorimeter normalized energy above the cut value in Table 3.1

Fig. 3.14 shows the results from the efficiency study. It can be observed that the efficiency is very stable and high over the range of HMS central momentum. After this study, a single correction number was extracted to be 0.996 ± 0.001. The

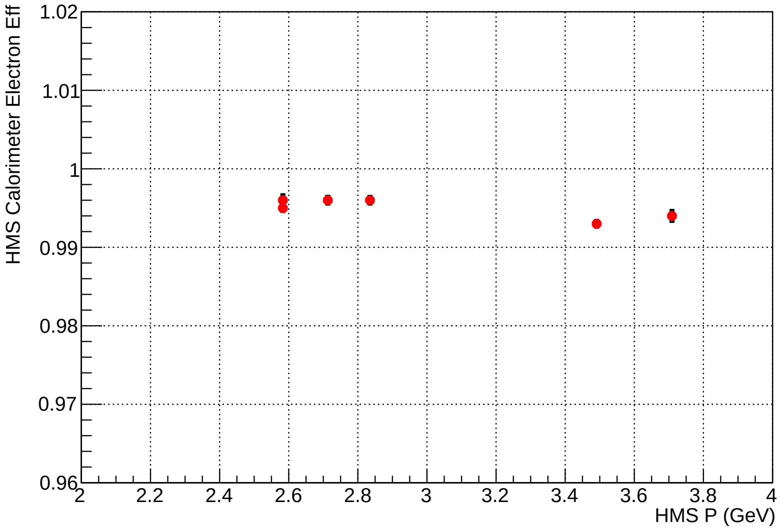

Figure 3.14: Measurement of HMS calorimeter efficiency for electrons with respect to HMS central momentum (P) from elastic singles data collected during the Kaon-LT experiment.

uncertainty for this efficiency also includes both statistical and systematic uncertainty. This correction factor is then used to correct all experimental yields. Similar to other correction factors, this also cancels in the ratio for the measurement of polarized cross-section through beam spin asymmetry.

3.6 Uncertainties

Both live times and detector efficiencies are calculated with a statistical uncertainty for each run using a binomial error calculation given by:

$$\Delta\epsilon \;=\; \sqrt{\frac{N_{Did}.N_{Should} \;-\; N_{Did}^{2}}{N_{Should}^{3}}} \tag{3.32}$$

where N_{Did} and N_{Should} are the same as described in Section 3.5.

3.7 Luminosity Study

The experimental cross-section measurement requires a careful estimation of different correction factors and systematic uncertainties. The Kaon-LT data are taken over a wide range of kinematics, including different beam energies, different spectrometer angle and momenta, different targets as well as different beam currents. This gives rise to a number rate dependent corrections. A dedicated study was performed (by other members of our collaboration) to understand these rate dependencies, known as the luminosity study. The luminosity data were primarily collected using a carbon target, due to high melting point (3550 °C), and the singles trigger in each spectrometer. Both spectrometers are set at negative polarity to detect electrons. The beam current was varied to study the rate dependencies. The luminosity studies are divided into three steps.

The first step was to study the normalized yield of scalers data as shown in Eq. 3.33. The scalers are hardware counters which record the number of pulses from the pre-triggers. These counters do not save any detector responses (e.g number of photo-electrons in the Cherenkov) and therefore, do not need to be corrected for CPU live time and tracking efficiency. The next step is to look at the untracked normalized yield as shown in Eq. 3.34. These are recorded events in which no track selection is done, and additional normalization factor of total live time (TLT) is applied for each individual spectrometer. The total live time is calculated using the method as described in Section 3.4. The final step is calculation of the tracked yield (i.e. events in which only good tracks are found to be included) is shown in Eq. 3.35, where the tracking efficiency is also used in the normalization along with the total live time and total charge. These three steps are completed on the same luminosity data to help in isolating the rate dependent effects arising from beam (step 1), DAQ (step 2) and detectors (step 3).

$$Yield_{scaler} = \frac{N_{scaler}}{Q_{tot}} \tag{3.33}$$

$$Yield_{notrack} = \frac{N_{notrack}}{Q_{tot} \times \epsilon_{TLT}} \tag{3.34}$$

$$Yield_{track} = \frac{N_{track}}{Q_{tot} \times \epsilon_{TLT} \times \epsilon_{tracking}} \tag{3.35}$$

Here

- Q_{tot} is the total charge collected in each run
- N_{scaler} correspond to number of scaler counts from pre-trigger (excluding EDTM triggers)

- $N_{notrack}$ correspond to events selected using coarse tracked quantities (as described in Section 3.2.1)

- N_{track} correspond to events selected using PID cuts after golden track selection (as described in Section 3.3)

- ϵ_{TLT} correspond to the total live time for each run

- $\epsilon_{tracking}$ correspond to the tracking efficiency for each run

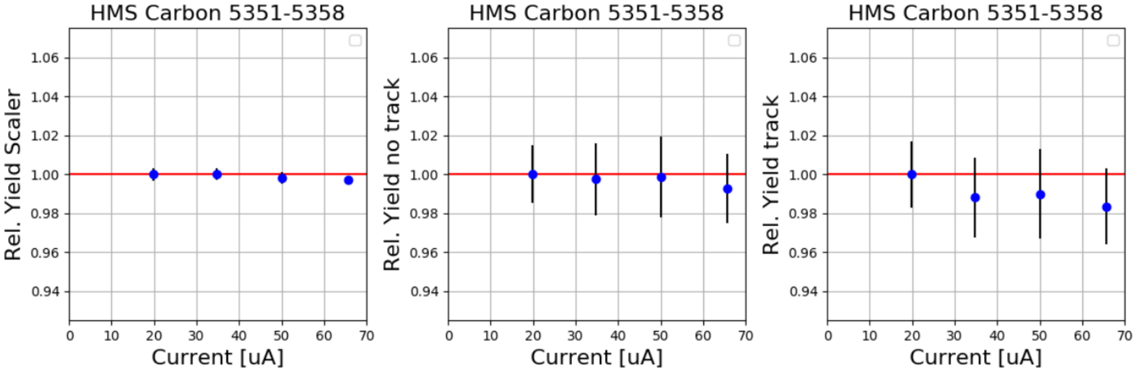

Figure 3.15: Luminosity studies results for carbon target with scaler yield (left), no-track yield (center) and track yield (right) from single luminosity data using HMS spectrometer [51].

The relative yield is calculated by scaling the normalized yield to the value obtained when extrapolating to zero beam current or rate. It is expected that the relative yield should be approximately equal to 1 regardless of the rate (or beam current) for carbon target. As seen in Fig. 3.15, the luminosity studies show very

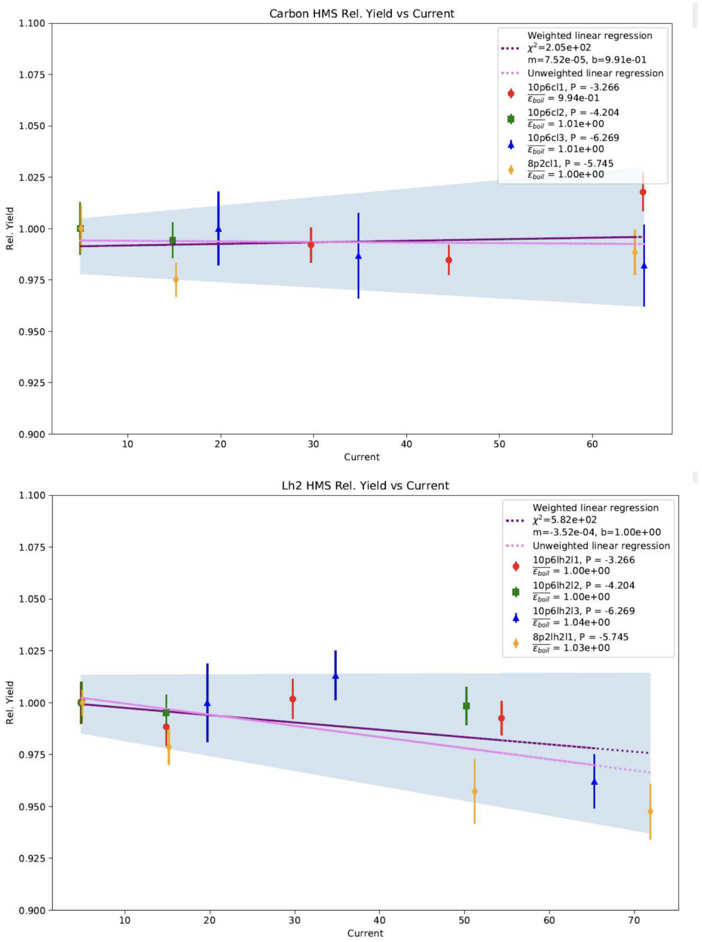

Figure 3.16: Final results from luminosity study after combining data from multiple beam energies for carbon target (top) and LH_2 target (bottom) over a range of current. Each kinematic setting was independently analyzed and scaled to 1 at zero current before combining together to extract an overall boiling correction factor for carbon (0.2% ± 4%) and LH_2 (7.9% ± 2%) [51]. The shaded region corresponds to the uncertainty of the linear fit.

stable yields for each of the three steps. The tracked yield shows a small trend that is statistically insignificant. The individual luminosity study results from each beam energy are then combined to study the relative yield stability over a wide range of beam currents. The slope of the combined relative yield with respect to current gives the boiling factor of the target. This slope is zero within the error for carbon target. This confirms that all the correction factors are precisely applied. It also gives confidence to the procedure used to determine boiling correction for liquid target (LH_2). Fig. 3.16 shows the final results for both carbon and LH_2 target boiling studies. This correction is then used to normalize the yields from the physics data. In the polarized cross-section measured through beam spin asymmetry, this factor cancels in the ratio. More details can be found in [51].

3.8 Physics Event Selection

After the selection of electrons in HMS and pions in SHMS (as described in Section 3.3), the next step is to select events for the pion electroproduction reaction. This event selection is done in two steps, where the first step is to identify electrons and pions from same beam bunch through coincidence time, and second step is to reconstruct the third final state particle through missing mass reconstruction. The data taken using empty aluminum target are analyzed in the same way as the LH_2 target physics data and the normalized yields of aluminum data are then subtracted from the physics data to remove contributions from the aluminum walls of the LH_2 target.

3.8.1 Coincidence Time

The Coincidence time is determined using the pre-trigger times from the SHMS and HMS:

$$\text{Coincidence Time} \;=\; \text{HMS Time} \;-\; \text{SHMS Time} \tag{3.36}$$

The coincidence time is corrected for particle type using time of flight for electrons (HMS) and pions (SHMS) and the variation of particle momentum between $-\delta$ and $+\delta$. This correction is done using the mass of particle and individual path lengths of each event in the spectrometer, as determined from the tracking and spectrometer reconstruction information. A detailed study was done to check the stability of coincidence time (details can be found in [52]). In order to center the coincidence time at zero, an offset is applied separately for each run to the coincidence time distribution. It can be seen in Figure 3.17 that the coincidence time distribution has good resolution and the prompt coincidence peak is e and π originating from the same beam burst. A random coincidence is subtracted from the prompt peak by taking average of six random peaks (3 on each side). The 4 ns beam structure described in Section 2.1.1 is clearly visible. Table 3.3 lists the cuts used for prompt and random peaks selection.

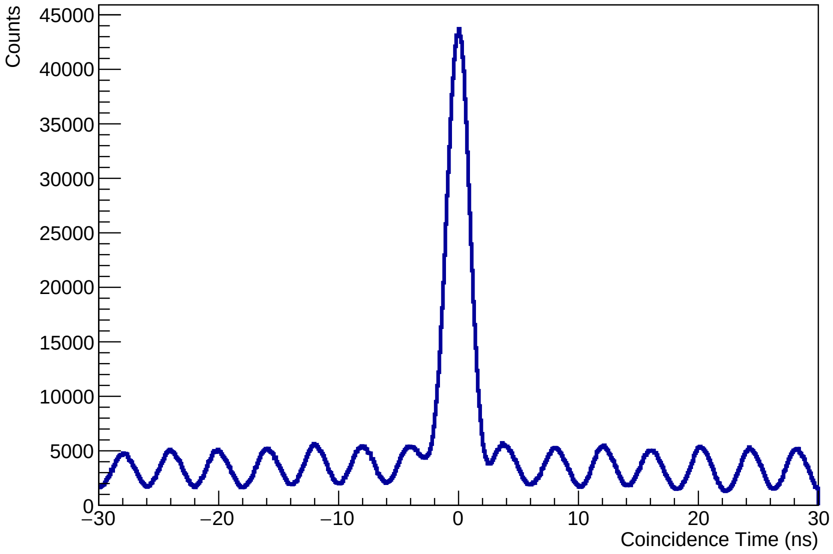

Figure 3.17: Coincidence time distribution for electron-pion from Kaon-LT data ($Q^2 = 2.1$, $W = 2.95$). The large peak in the middle corresponds to the real coincidence events (signal selection) and small peaks on either side correspond to the random coincidence events (used for random background subtraction).

Coincidence Time variable	Prompt Peak Selection	Random Peak Selection
CTime.ePiCoinTime.ROC1	± 2.25	$11.25 - 24.75$ (right) $-24.75 - -11.25$ (left)

Table 3.3: Coincidence time cuts used for prompt peak and random peak selection for $e\ \pi^+$ event selection in Kaon-LT experiment.

3.8.2 Missing Mass Reconstruction

In Hall C, the third particle, in this study, is not directly detected in any of the detectors because this particle has very low momentum and is electrically neutral, making it impractical to place detectors in the corresponding locations. In the exclusive pion electroproduction reaction, this particle is either a neutron or a Δ^0. In order to select the third particle, the missing mass distribution is plotted for the reaction in study. Missing mass is calculated by subtracting the four momenta of final state detected particles (electrons and pions) from the four momenta of initial state particles (electron beam and target protons) as shown in Eq. 3.37.

$$M_{miss} = \sqrt{(E_{beam} + m_p - E_{e'} - E_{\pi^+})^2 - (\vec{p_e} - \vec{p_{e'}} - \vec{p_{\pi^+}})^2} \tag{3.37}$$

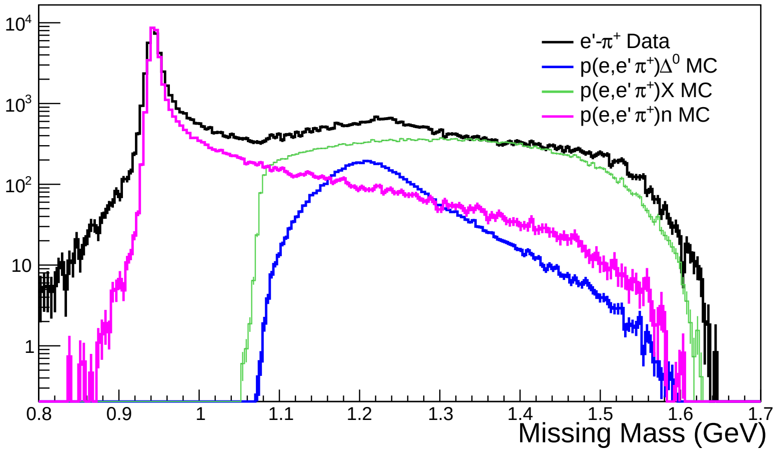

Figure 3.18: Missing mass distribution for exclusive pion electroproduction reaction from Kaon-LT experiment. The y-axis on the plot is log scale.

Figure 3.18 shows the missing mass distribution for the exclusive pion electroproduction reaction after applying the particle identification and event selection cuts. It can be observed that the missing mass distribution has no background from the kaon exclusive electroproduction reaction or the u-channel processes with proton in the SHMS (due to the lack of peaks from the $p(e, e'K^{+})\Lambda/\Sigma^{0}$ and $p(e, e'p)\omega$ reactions). This confirms that the non-pion contamination after particle ID and event selection is very small. Different pion processes contribute to the data distribution in the figure. A detailed study of missing mass region is performed using Monte-Carlo simulation which is described in the next chapter.

Chapter 4

Simulation

This chapter gives a brief introduction of the Hall C simulation package for coincidence experiments (SIMC), a description of SIMC event generation, spectrometer models and different physics reactions. The study of the elastic scattering reaction and kinematic offsets (performed by members of the collaboration) is described for completeness. Additionally, the simulation resolution correction study is outlined in detail. Finally, a missing mass study is described, focusing on the procedure of background estimation in Δ^0 region and a number of checks performed to verify the reliability of the fitting procedure for different physics processes.

4.1 SIMC Overview

SIMC [53, 54] is the standard Monte Carlo simulation used for Hall C coincidence reactions. Originally developed in Fortran for the analysis of SLAC $(e, e'p)$ experiments and known as SIMULATE, the code underwent modifications throughout the mid to late 1990s to incorporate the HMS and SOS spectrometer models, replacing the SLAC ones. These modifications continued into the 2000s and early 2010s, expanding to include models like the new SHMS. Over time, SIMC has evolved to account for particle decay, ionization energy loss, radiative effects, multiple scattering, simple rules for final state interactions, and Coulomb corrections. Its scope has broadened to simulate various reactions, including elastic, quasi-elastic, and meson electroproduction. Since the Hall C spectrometers have narrow acceptance, SIMC is written to simulate one reaction at a time. Each contributing process to a given setting is run separately and then added together for comparison to the experimental data.

In practice, SIMC generates events uniformly along the beam direction through the target, filling the kinematic phase space (x', y', δ) to ensure full spectrometer acceptance while considering the outlined interaction mechanisms. The vertex coordinates are determined by the target size, position, raster size, and beam spot size. Although the phase space covers 100% acceptance, geometric cuts may be applied to align with the spectrometer model or detector design constraints as described in

Section 3.3.2. These generated events are then passed through spectrometer models that simulate the magnetic optics and apertures. Valid events are those that pass all apertures and cross the necessary simulated detectors, and their trajectories are fitted in the focal plane before being propagated back to the target (as described in Section 3.3.3) for corrections in energy loss (for the tracking through the focal plane and other materials) and fast raster. At this point, all relevant physics quantities are calculated. While SIMC can simulate the magnetic optics and check trajectories, it is important to mention that detectors in SIMC do not provide hardware responses (like PMT signals or Cherenkov internal detector geometry), thus individual detector inefficiencies are excluded. Rather, in SIMC, particles are tracked through the detector materials and undergo scattering and energy loss before a simulated trigger decision is made. SIMC is a weighted simulation framework, where each event is weighted by a model cross section, normalized for target thickness and beam charge, radiative processes, and a Jacobian for conversions between lab and center of mass coordinates, as well as a second Jacobian for spherical and spectrometer coordinates.

4.2 Event Generation

In SIMC, events are randomly generated, in a uniform distribution, over a wider than experimental phase space of energy and acceptance for the incident electron beam. The final state scattered particles are generated around the predefined central momenta and angles (X'_{tar} and Y'_{tar}). The four momenta for the entire reaction is conserved and the acceptance varies for different physics reactions. Events are only recorded if they successfully transport to the detector hut and impinge on all the relevant detectors in each spectrometer. The scattered particles pass through the modeled spectrometer acceptance while accounting for interactions like ionization energy loss and multiple scattering. In SIMC, the pion electroproduction reaction cross-section is adopted from the experimental cross-section as described in Chapter 1. A detailed description of this available in [55].

4.2.1 Spectrometer Models

The spectrometers in SIMC, modeled using COSY Infinity [56], use a detailed set of forward matrix elements. After the generation of angles and momenta at the vertex, each particle is transported through the spectrometer magnetic fields. This is done by using the forward optics matrix elements which transport the particle's position, direction and fractional momentum. The focal plane acceptance, detector acceptance, momentum spread and the target quantities are calculated in same way as the experimental data. The backward optics matrix elements are needed to reconstruct the target quantities, just as is done for the experimental data. For the cross-section models for different meson electro-production reaction processes, SIMC uses a global fit of the existing experimental data. A detailed description is available in [36].

4.3 Elastic Scattering Reaction $H(e, e'p)$

As discussed in Section 2.7.1, the e-p elastic scattering reaction is a simple process that can be studied in Hall C. The cross-section of this reaction has been measured to very high precision from other experiments, therefore it can be used to understand many of the experimental systematics. This is done by reproducing the known cross-section accurately. The elastic cross-section model in SIMC is based on the existing world data. The Heep coincidence data allows the study of offsets on the experimental kinematics (spectrometer angles and momentum). Additionally, the accuracy of momentum and angle acceptance, detector efficiencies and DAQ live times are verified by comparing the normalized yields and event distributions between data and simulation.

4.3.1 Kinematic Offset

The spectrometers in Hall C are configured to select particles of specific momentum and angle. The desired central momentum is achieved by carefully tuning the current of quadrupoles and dipole in each spectrometer resulting in a specific magnetic field. The polarity of the magnets dictates the charge of the particles. During data taking, the particles have a spread of momentum around the central momentum in each spectrometer. The spectrometers are physically moved to detect particles at specific scattering angles. The measured values of spectrometer momenta and angles can be inaccurate due to the imperfect knowledge of the location of spectrometers (vertical and horizontal angle offsets) and magnetic fields (momenta and energy offsets). This results in inaccurate reconstruction of the final state particles. Since the cross-sections are calculated by comparing the normalized yields from the experimental data and the simulations, it is really important to accurately measure all the kinematic quantities. This can be done by determining offsets for spectrometer momenta, angles and the incident electron beam energy. These offsets are determined by using Heep coincidence data. The Heep coincidence reaction is a two body process where all incident and final state particles are directly detected. The e-p elastic cross section falls steeply with momentum transfer, so knowledge of the experimental kinematics is critical for reproducing known cross-section to high precision. A comparison of components of missing momentum, missing energy and invariant mass is studied between experimental data and simulation. Fig. 4.1 shows the comparison of the experimental data and simulation before applying any offsets. The missing energy and momentum can be defined from the conservation of energy and momentum between the incident electron (e) and the scattered electron ($e^{'}$) and proton ($p^{'}$) as follows:

$$E_m \ = \ E_e \ + \ m_p - \ E_{e'} \ - \ E_{p'} \tag{4.38}$$

$$\vec{P_m} = \vec{P_e} - \vec{P_{e'}} - \vec{P_{p'}} \tag{4.39}$$

The kinematic offsets are determined using the Heepcheck program [57] which was originally written for the Hall C coincidence experiments during 6 GeV era. This

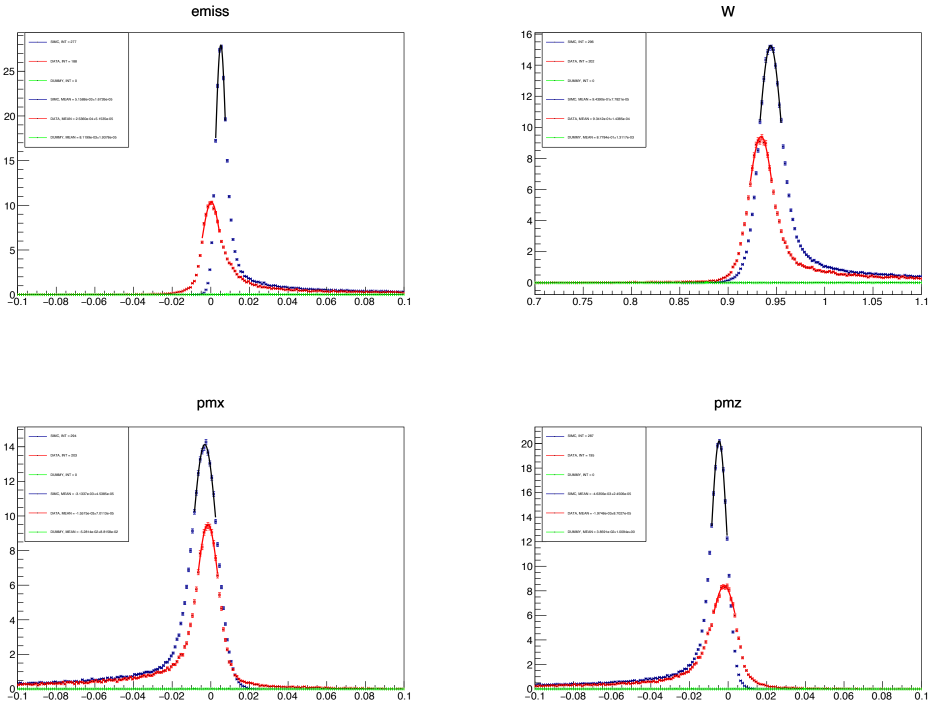

Figure 4.1: Distribution of normalized yields for missing energy, in-plane missing momenta and invariant mass without offset for elastic e-p coincidence data taken at 6.2 GeV [51]. The blue correspond to SIMC, red correspond to data from the LH_2 target and green correspond to data from the aluminum (dummy) target.

program determines offsets for beam energy, spectrometer central momentum and in-plane angles. This is done by using the difference between centroid values (a Gaussian fit is made to the full width half maximum region of each peak and that value used as the centroid), for each variable in Fig. 4.1, of the experimental data and simulation and the known kinematic dependencies between these quantities. An initial offset study for high Q^2 Kaon-LT Heep coin data was completed where the offsets were

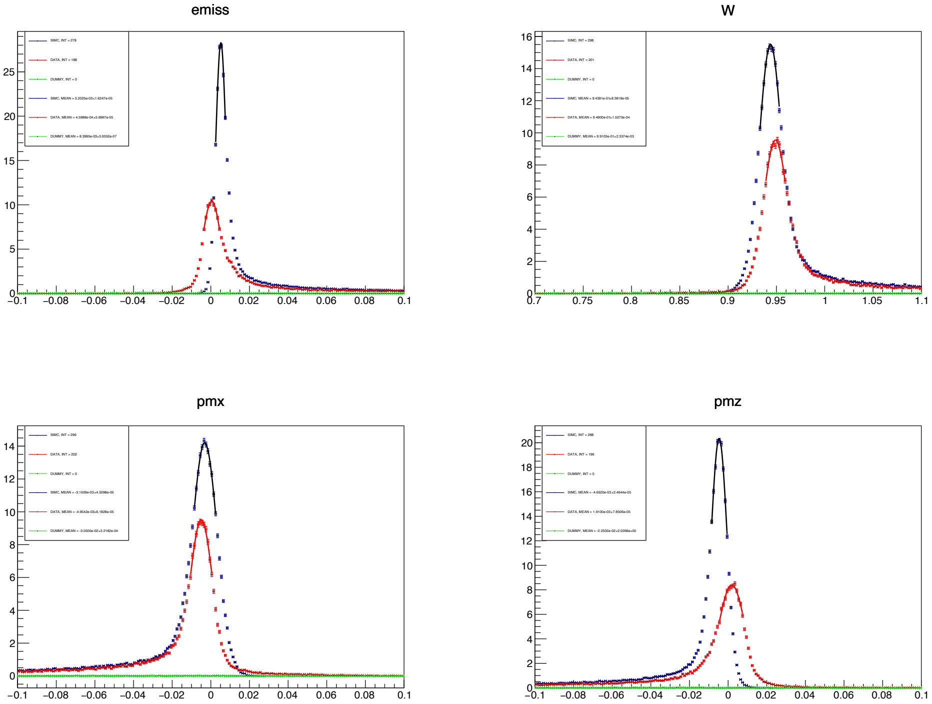

Figure 4.2: Distribution of normalized yields for missing energy, in-plane missing momenta and invariant mass with offset for elastic e-p coincidence data taken at 6.2 GeV [51]. The color legend is the same as in Fig. 4.1.

determined for each beam energy separately. Later, a global offset study was done for all Kaon-LT data and calculated a set of global offset values. The goal of the global offsets was to get reasonable agreement between the experimental data and simulation for all datasets. Finally, an optimization of the global offsets was done to obtain a set of offsets which can then be used for physics data. A detailed description of the offset study from the Heepcheck program is available in [58]. Fig. 4.2 shows the the comparison of the experimental data and simulation after applying the offsets for beam energy, spectrometer central momentum and in-plane angle.

The out-of-plane angle offsets are calculated using the discrepancy between y-component of missing momentum for data and simulation. The study was done under the assumption that the electron beam is centered on the target and any target offset

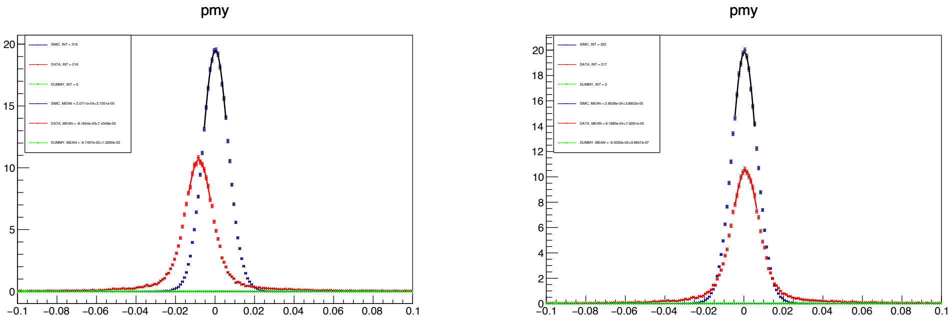

Figure 4.3: Distribution of normalized yields for the y-component of missing momentum before (left) and after (right) applying the out-of-plane offset for elastic e-p coincidence data taken at 6.2 GeV [51]. The color legend is the same as in Fig. 4.1.

E_b	dE_b	dP_e	dP_p	$d\theta_e$	$d\theta_p$	$d\phi_e$	$d\phi_p$
10.585	$+0.05\%$	-0.01%	-0.02%	$+1.0$	$+1.1$	$+2.51$	-0.11
8.209	$+0.05\%$	-0.01%	-0.02%	$+1.0$	$+1.1$	$+2.51$	-0.11
6.190	-0.02	-0.01%	-0.02%	$+1.0$	$+1.1$	$+2.51$	-0.11
4.932	-0.07%	-0.01%	-0.02%	$+1.0$	$+1.1$	$+2.51$	-0.11
3.835	-0.03	-0.01%	-0.02%	$+1.0$	$+1.1$	$+2.51$	-0.11

Table 4.1: Kinematic offsets for elastic e-p coincidence data collected during the Kaon-LT experiment. Here angle offsets are in units of mrad and the momentum and beam energy offsets are normalized to the spectrometer central momenta and beam energy. The sub-scripts e and p correspond to electron arm (HMS) and proton arm (SHMS) [51, 58].

is negligible. A detailed description of the out-of-plane offset procedure is available in [58]. Fig. 4.3 shows a comparison for the experimental data and simulation for the y-component of the missing momentum (P_y^{miss}). The final offsets are tabulated in Table 4.1, where the second column correspond to the offset in beam energy, the third and fourth columns correspond to offsets in central momenta of HMS and SHMS respectively, column five and six correspond to in-plane angle offsets for HMS and SHMS respectively, and the last two columns give the out-of-plane angle offsets for HMS and SHMS respectively.

4.3.2 $H(e, e'p)$ Yield Ratio

A detailed study has been done on all of the Heep coin data from the Kaon-LT experiment. The first step in this study is to accurately perform a particle identification and event selection. This process is similar to the procedure outlined in Chapter 3. The only difference is the selection of protons in the SHMS instead of pions which can achieved by flipping the Cherenkov cuts listed in Table 3.2. After the successful event estimation and particle ID, the next step is to estimate efficiency and live time corrections, which are used to normalize the data. As explained in Sections 3.4 and 3.5, the efficiency for each detector is calculated separately and then a total efficiency is calculated by multiplying all the individual efficiencies. Since the data are also normalized by total live time, it is also included in the total efficiency calculation of each run. The uncertainty in the total efficiency is estimated by adding, in quadrature, all of the uncertainties associated with each efficiency. The data are also normalized by beam charge to yield per unit charge (mC). To simplify the normalization process, an effective charge is calculated by multiplying the total efficiency with the total beam charge. The data taken from the aluminum target are used to subtract the contribution from the aluminum walls of the hydrogen target. The efficiency calculation and effective charge normalization for aluminum target data is done in an identical manner to the regular hydrogen target data and then the yield is subtracted from the hydrogen data.

$$Y_{data} = \frac{\text{No. of Events}}{\text{Effective Charge } \times \text{Target boiling correction}} \tag{4.40}$$

$$\text{Effective Charge} = \text{Total Charge} \times \text{Total Efficiency} \tag{4.41}$$

Once the cuts are applied and the effective charge normalization is done, the data

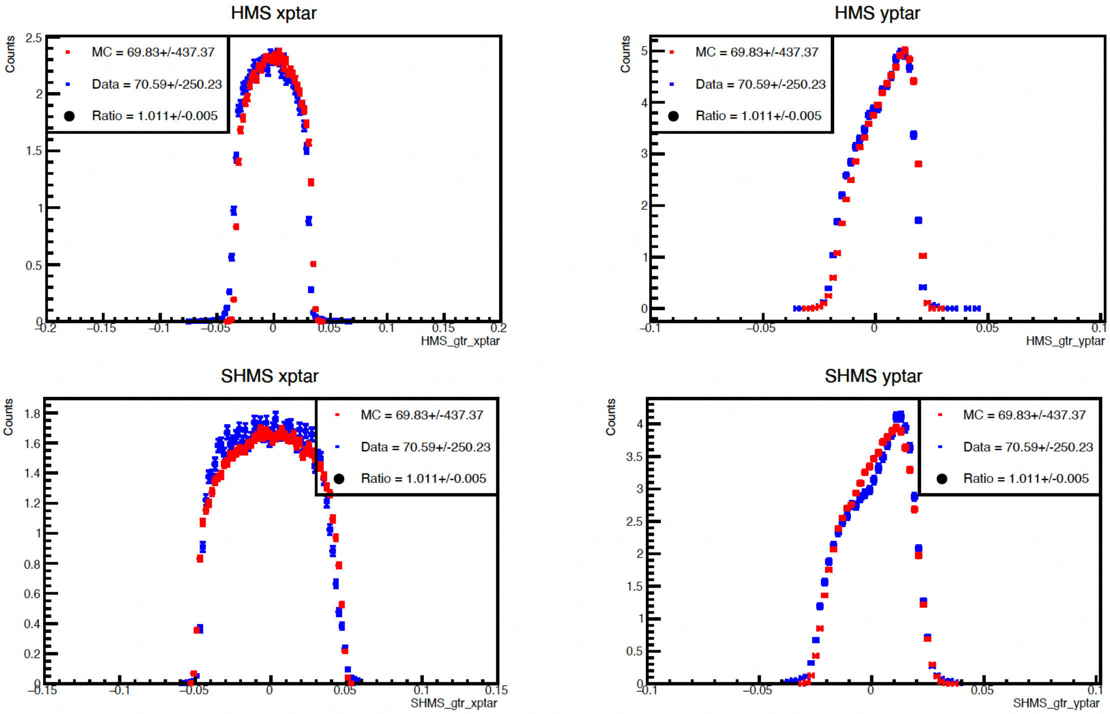

Figure 4.4: Comparison of reconstructed target quantities (X'_{tar} and Y'_{tar}) for HMS (top) and SHMS (bottom) between normalized yields from the experimental data and simulation [59]. The red correspond to SIMC and blue correspond to data.

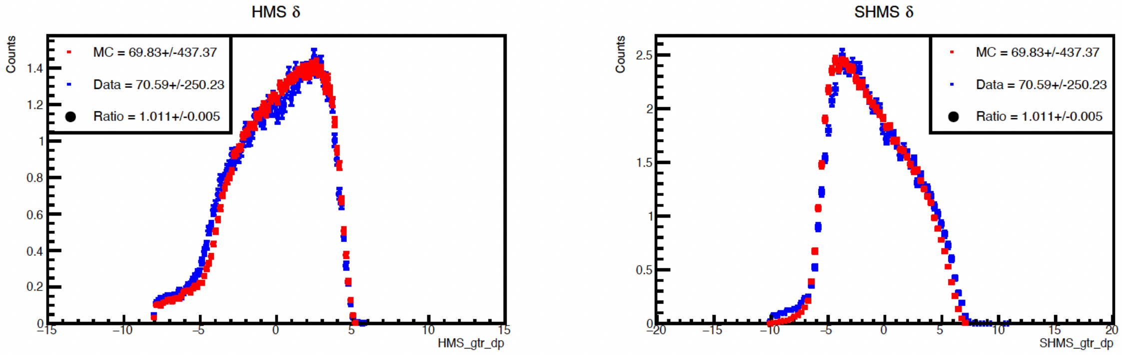

Figure 4.5: Comparison of momentum acceptance (δ) for HMS (left) and SHMS (right) between normalized yields from the experimental data and simulation [59]. The color legend is the same as in Fig. 4.4

are ready to be compared with simulated events. Simulated events are already normalized to unit charge and the events are normalized with the weights from the known elastic scattering cross-sections. Since SIMC does not generate detector response (e.g. number of photoelectrons), therefore, the comparisons are usually done by looking at the acceptance variables (focal plane quantities, reconstructed target quantities etc). Fig. 4.4 shows the comparison of reconstructed target quantities. The results show that the SIMC is in good agreement with the experimental data, as both yield and shape of the distributions are comparable with high accuracy. The momentum spread, (δ) is an important variable to be compared between experimental data and SIMC as it confirms that the experimental spectrometer acceptance is consistent with the simulated expectation. Fig. 4.5 shows that both HMS and SHMS have good comparison between the data and SIMC. The HMS has narrower momentum acceptance whereas SHMS has much wider momentum acceptance (as listed in Table 2.4). The plot shows δ value in percentage of the central momenta.

The whole analysis is repeated for each Heep coincidence dataset from the Kaon-LT experiment and the final step is compare the yield ratios for each Heep coincidence setting. Fig. 4.6 shows the yield ratios for all data sets. It can be observed that the yield ratios are close to one for all the settings. This confirms that all the experimental effects are understood to a high precision and experimental data is reproducing the known elastic cross-section used in the simulation. These ratios also confirm that the procedure of calculating normalized experimental yields is accurate and this method can be used for the physics data. It is important to note that these results does not include proton absorption correction (which is estimated to be 2-4%).

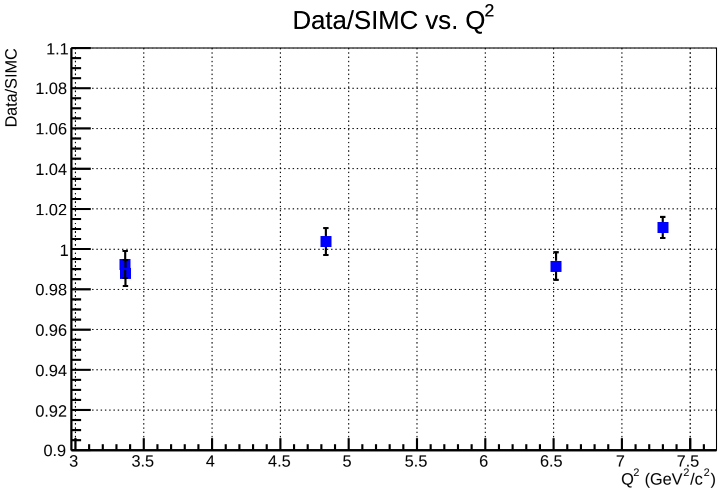

Figure 4.6: Comparison of Data/SIMC yield ratio with respect to the four momentum transfer (Q^2) for all elastic coincidence data from the Kaon-LT experiment [59].

4.4 Missing Mass Study

The Hall C spectrometers give access to very good missing mass resolution. Fig. 4.7 shows the missing mass distribution including both experimental data and different simulated processes for the pion electroproduction reaction. The plot on the left gives the range of missing mass, including the exclusive peak and part of the resonance region, which clearly shows a clean neutron peak due to $p(e, e'\pi^+)n$. The radiative tail of neutrons show a mismatch between experimental data and simulation which indicates that experimental data are smeared out and this effect is more prominent at higher energies ($E_{beam} > 8$ GeV). The figure on the right is a zoomed in version of the same plot to focus on the Δ^0 region. As has been demonstrated in Fig. 3.18, the

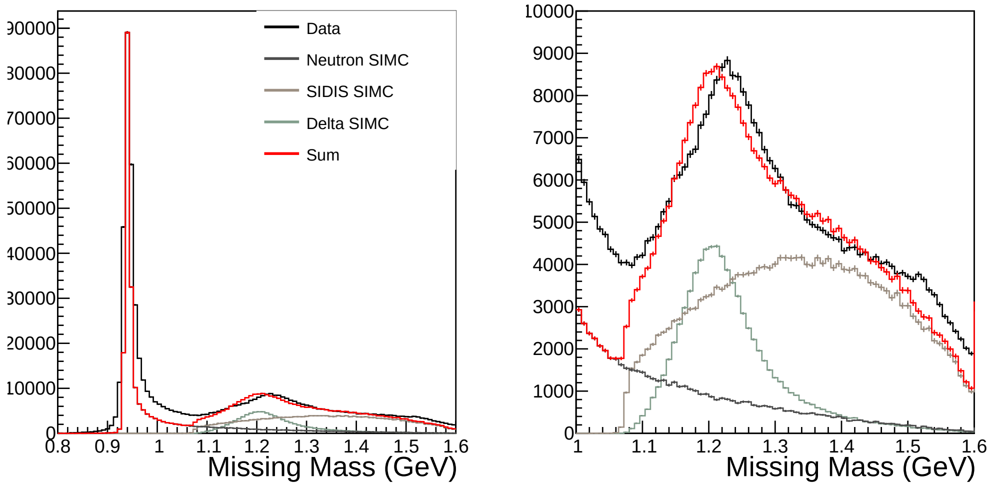

Figure 4.7: Missing mass distribution for the exclusive pion electroproduction reaction from Kaon-LT data ($Q^2 = 2.1\ GeV^2,\ W = 2.95\ GeV$).

$p(e, e'\pi^+)n$ sample can be selected by using a missing mass cut around the neutron peak. On the other hand, the Δ^0 is a broad distribution that sits on a significant background due to multi-pion non-resonant processes. This means that Δ^0 can't be selected using only a missing mass cut and requires a more sophisticated background study.

4.4.1 SIMC resolution correction

The resolution difference between experimental data and simulation comes from inaccurate detector response in the simulation. This resolution difference is problematic in the Δ^0 region because it is contaminated by $p(e, e'\pi^+)n$ and $p(e, e'\pi^+)X$ background processes and each background needs to be estimated accurately before isolating the Δ^0 events. The HMS spectrometer has been simulated to higher accuracy during the analysis of 6 GeV experiments. The SHMS spectrometer is brand new and therefore the simulation of this spectrometer isn't optimized yet. A major task of Kaon-LT experiment is to commission the SHMS. Therefore a resolution correction study was done to optimize the drift chamber resolution in SIMC.

The resolution difference between data and simulation varied for different Kaon-LT kinematics. An initial study was done to optimize the simulation resolution for each kinematics separately. This resulted in different resolution correction factors (in the range of 3-10 times the default resolution) for each kinematics. Since the drift chamber resolution should be independent of kinematics for each set of data taken during Kaon-LT, a global correction factor is needed for all data. This procedure was done to get an overall improved agreement for all kinematic settings. An important constraint during this study was to keep the simulated distribution from over estimating the width of the data. Figure 4.8 shows a comparison of missing mass distribution for uncorrected and corrected simulation and experimental data.

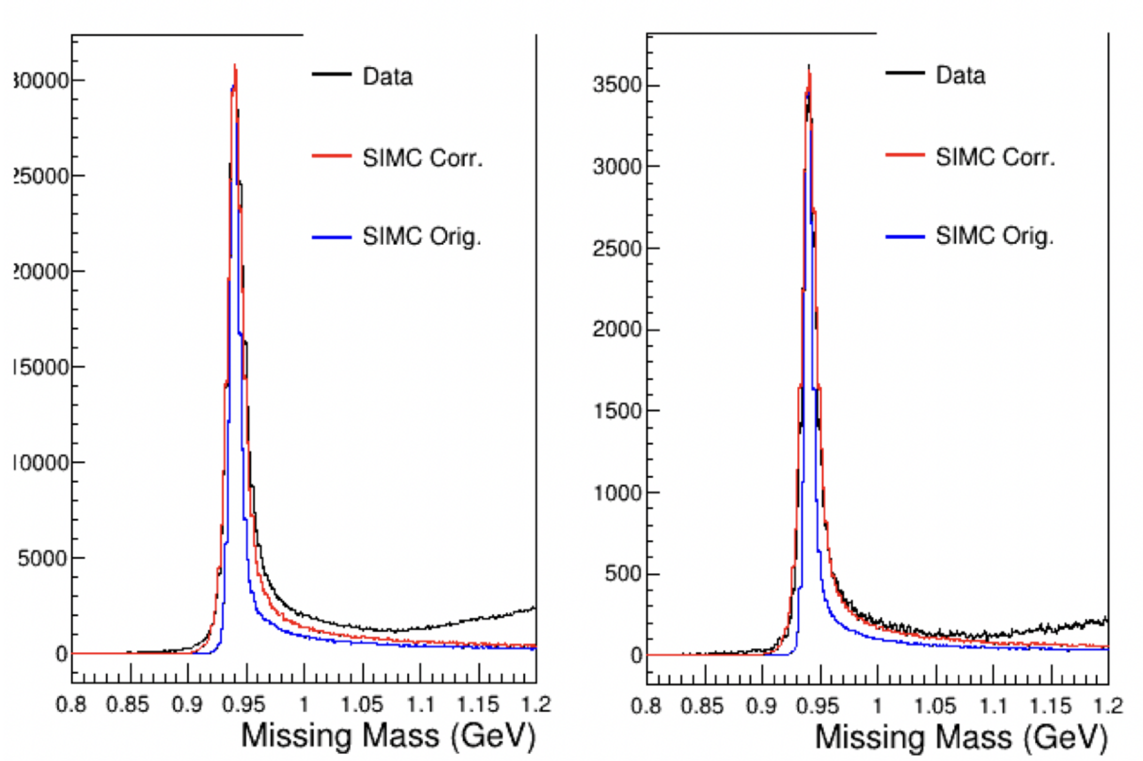

Figure 4.8: Missing mass distribution for data and simulation (original and corrected) for $Q^2 = 3.0$ GeV^2 (left) and $Q^2 = 4.4$ GeV^2 (right). It can be seen that resolution corrected SIMC distribution agrees better with the data at higher Q^2.

The next step is to check the t-dependence of the resolution correction. This is important because the experimental missing mass resolution changes for different t-bins. The width of the neutron peak, as well as the radiative tail, is small at low $-t$. A possible source of this difference can be the increase in background physics processes at higher $-t$, whereas these processes are kinematically forbidden at low $-t$. Figure 4.9 confirms the resolution corrected simulation doesn't overestimate the experimental data over a wide range of $-t$. The overall agreement between

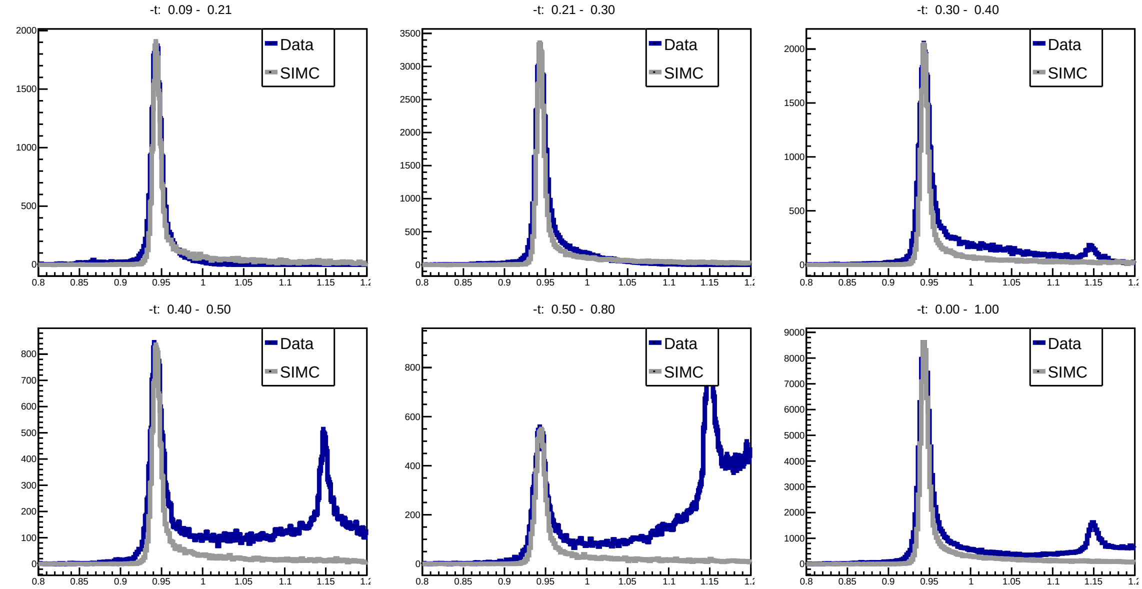

Figure 4.9: Missing mass distribution for data and corrected simulation binned in t for $Q^2 = 4.4$ GeV^2. The SIMC distribution is only for the $p(e, e'\pi^+)n$ whereas experimental data contains multiple pion electroproduction processes as well as some some kaon electroproduction events.

simulation and experimental data is improved. The small mismatch is incorporated in the systematic uncertainty of background study given in Section 5.5. The final step is to compare the reconstructed target angles for the SHMS. This is also important because resolution correction in missing mass should not have an adverse effect on the reconstructed quantities. Figure 4.10 confirms that the reconstructed angles X'_{tar} and Y'_{tar} are consistent for uncorrected and corrected simulation samples. The final correction factor used for all simulation samples is resmult = 3.5 (original factor was resmult = 1.9). This factor is multiplied to the drift chamber resolution calculation in the SHMS.

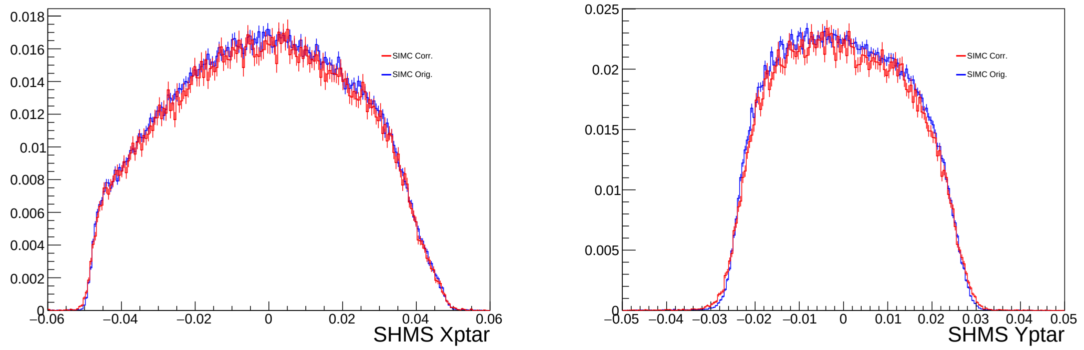

Figure 4.10: Distribution for reconstructed target quantities for SHMS before and after resolution correction for $Q^2 = 4.4$ GeV^2.

4.4.2 $\pi^+\Delta^0$ shape study

The missing mass distribution in the Δ^0 region is contaminated by other background physics processes. The contamination from the exclusive kaon electroproduction reaction $p(e, e'K^+)\Lambda$ can be removed by using a heavy gas Cherenkov cut in the SHMS. This leaves events with only pions in the final state. Background contributions in the Δ^0 region include the radiative tail of $p(e, e^{'}\pi^+)n$ and multi-pion phase space in the form of Semi Inclusive Deep Inelastic scattering (SIDIS), $p(e, e^{'}\pi^+)X$ processes. The first attempt to estimate this background was to use a simulation for both background processes and fit to the experimental data for each kinematics. This

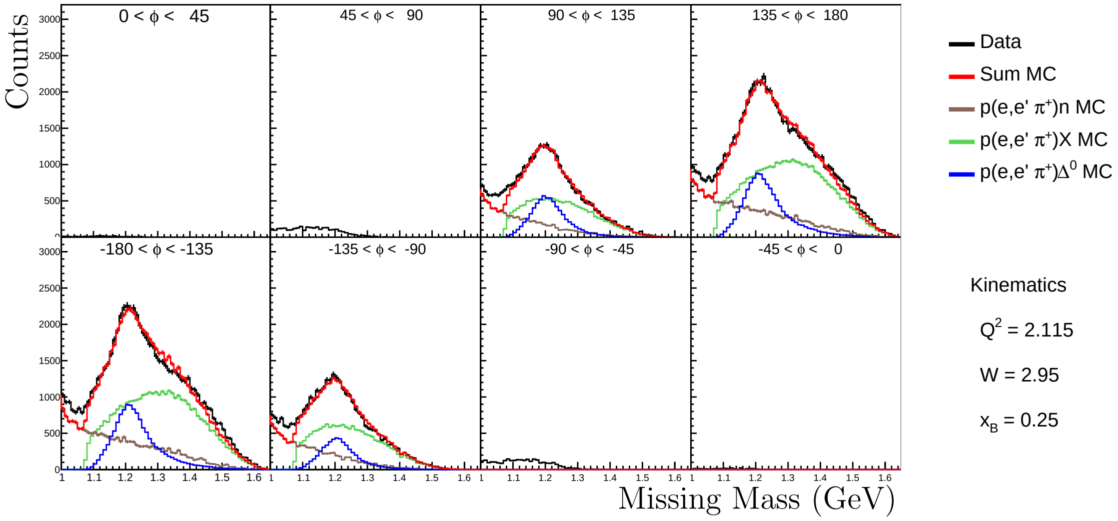

Figure 4.11: Shape study for missing mass distribution in the region of Δ^0 for left SHMS setting data in each ϕ bin ($Q^2 = 2.1$ GeV^2, $W = 2.95$ GeV). The simulated processes are fitted to the data.

meant that each physics process (signal and each background) for every kinematic setting from Kaon-LT experiment (for 10.6 GeV datasets) would need to simulated three times corresponding to three SHMS settings. The SIDIS simulation package was provided by the Hall C SIDIS collaboration [60]. This study was unfruitful due to mismatch in shape of sum of all simulation and experimental data, as shown in Fig. 4.7. It was later revealed that the missing mass shape for one kinematic setting varied for different ϕ bins. This required a bin-by-bin missing mass shape study for each ϕ bin. The experimental data and all the simulated processes were then binned identically and the simulated background was fitted to the data.

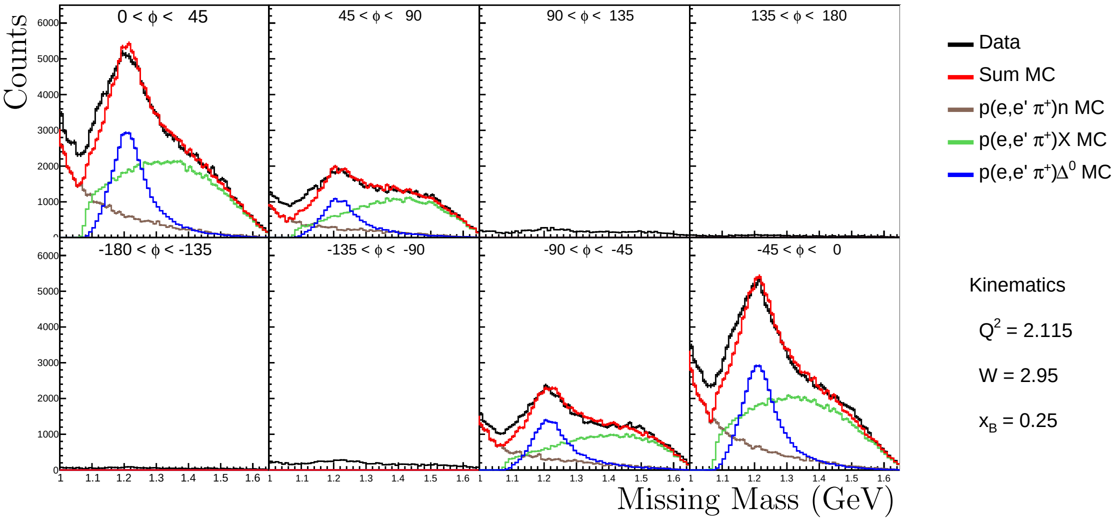

Figure 4.12: Shape study for missing mass distribution in the region of Δ^0 for right SHMS setting data in each ϕ bin ($Q^2 = 2.1$ GeV^2, $W = 2.95$ GeV). The simulated processes are fitted to the data.

The background shape study was done separately for each SHMS setting and helicity state. Figures 4.11 and 4.12 show a bin-by-bin shape study for left and right SHMS setting data. It can be seen that these settings are mirror images of each other and do not give full ϕ coverage individually. On the other hand, the center SHMS setting gives full coverage across all ϕ bins as shown in Figure 4.13. The 3 SHMS settings combine to give full phi coverage over a wide range of t, as shown in Fig. 2.34.

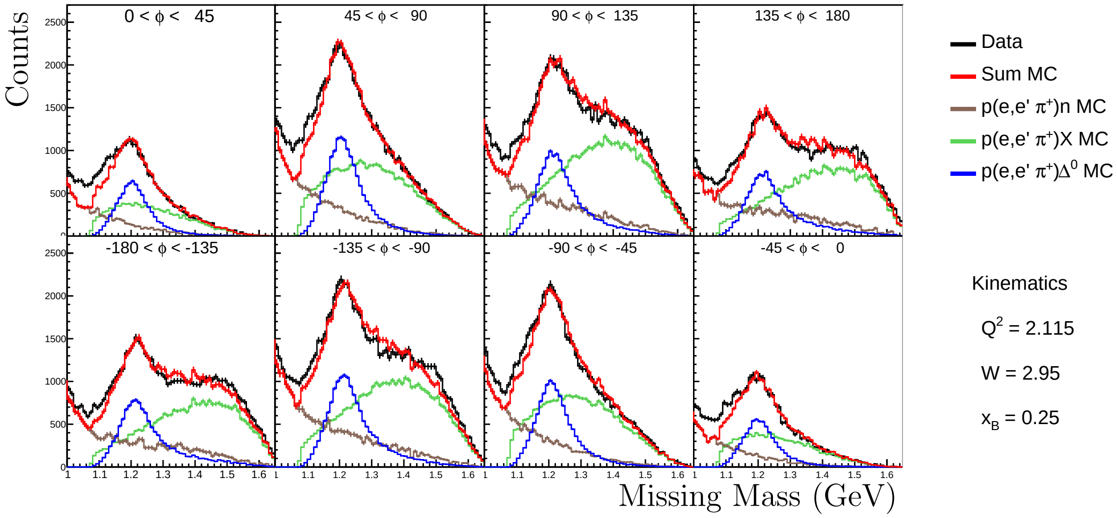

Figure 4.13: Shape study for missing mass distribution in the region of Δ^0 for center SHMS setting data in each ϕ bin ($Q^2 = 2.1$ GeV^2, $W = 2.95$ GeV). The simulated processes are fitted to the data.

In each ϕ bin, the SIDIS simulated distribution is fitted to the data in a missing mass region where there's no contribution from Δ^0 events (1.4 - 1.55 GeV). The neutron simulated distribution is scaled to the neutron data peak region (0.925 - 0.955 GeV). The two backgrounds are added together and then subtracted from the data. The remaining experimental data distribution is used to fit the Δ^0 simulated distribution. Finally, the sum of the three simulated processes is compared with the total experimental data. The goal of this study was to get good overall agreement between data and simulation across all bins. It can be observed from the plots that some bins have better agreement than others, but the overall agreement shows that data shape can be reproduced by the sum of all the simulated processes in the region of interest (1.11-1.40 GeV).

Several studies were performed to check the reliability of the fitting procedure. One of those studies was to check the diffractive ρ production process ($p(e, e'\rho^+)n$ where $\rho^+ \rightarrow \pi^+\pi^0$) [53] as an additional background. As shown in Fig. 4.14, the shape of this process resembled the SIDIS background and both distributions overlapped,

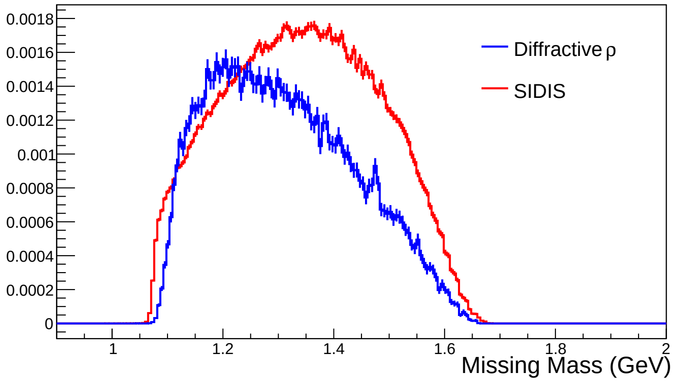

Figure 4.14: Missing mass distribution comparison for simulated Semi-Inclusive Deep Inelastic Scattering (SIDIS) and Diffractive ρ production ($Q^2 = 2.1$ GeV^2, $W = 2.95$ GeV).

making it very difficult to separate these two processes. Each of these processes was separately used to estimate the background in the higher missing mass region (above 1.4 GeV) and the results showed that SIDIS process gave a better agreement to the experimental data in that region. Therefore the ρ process was not used in the final shape study.

The combined background from neutron and SIDIS simulation processes was fitted to the total background in the experimental data. Similarly, the Δ^0 simulation is fitted with the background subtracted experimental data. Figures 4.15 and 4.16 show that the fitting procedure gives good agreement between data and simulation. The yields

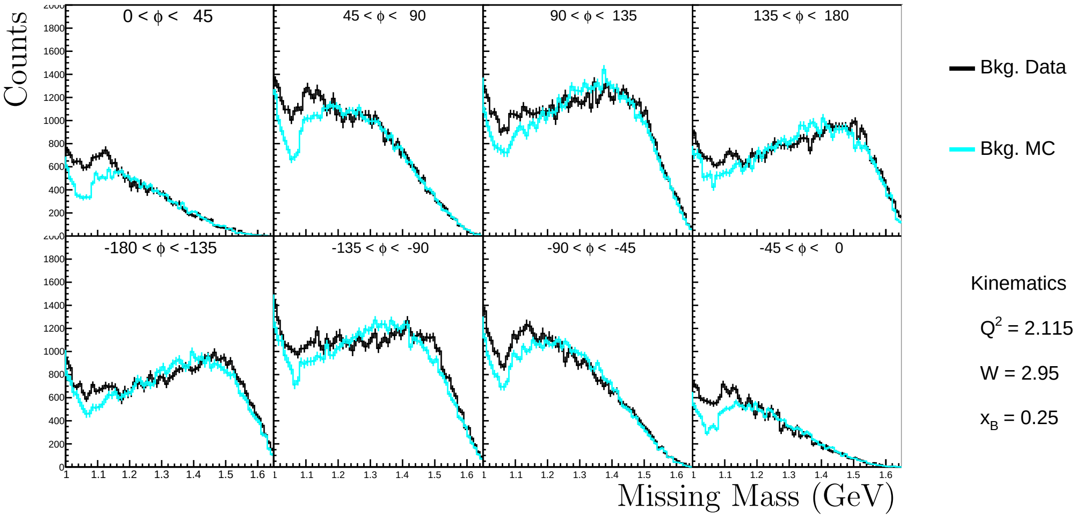

Figure 4.15: Missing mass distribution for the the sum of fit background processes in the region of Δ^0 for center SHMS setting data in each ϕ bin (Q^2 = 2.1 GeV^2, W = 2.95 GeV). The simulated processes are fitted to the data.

for each bin are calculated by integrating the background subtracted experimental data in the region (1.11 - 1.40 GeV). A small mismatch can be observed between the Δ^0 simulation and background subtracted experimental data in the tail regions. The mismatch to the left of the Δ^0 peak is due to a small contamination from the neutron radiative tail and the mismatch to the right of Δ^0 comes from higher resonance pion electroproduction reactions. Since these mismatches are small and outside the integration range, a systematic uncertainty can be calculated for the cross-section. This will be discussed in detail in the next chapter.

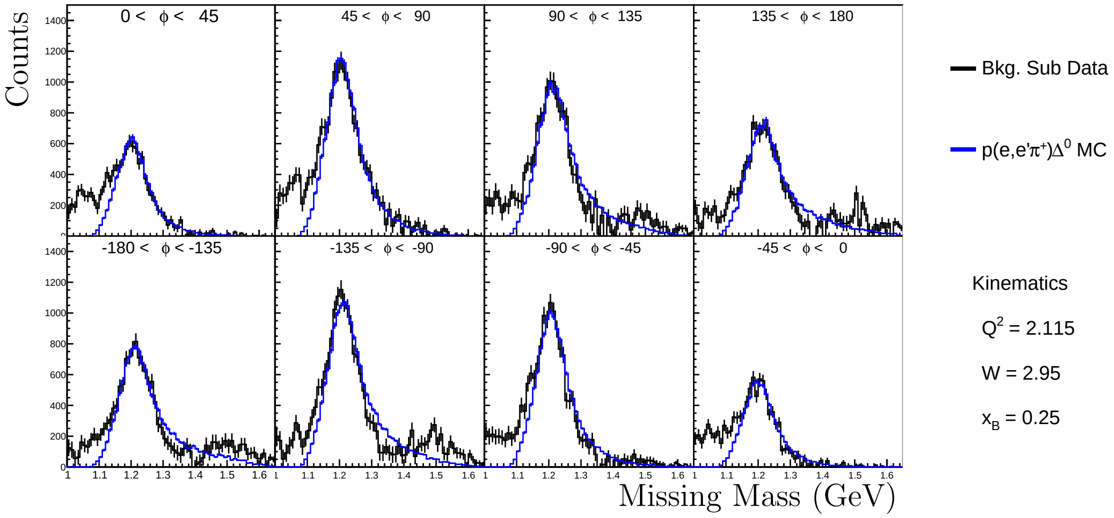

Figure 4.16: Missing mass distribution after all background processes are subtracted in the region of Δ^0 for center setting data in each ϕ bin ($Q^2 = 2.1$ GeV^2, $W = 2.95$ GeV).

Chapter 5

Results and Discussion

This chapter describes the physics results from this research work. To begin, a description of the binning procedure of the data and simulation into different kinematic quantities is provided. The method of beam spin asymmetry measurement is then outlined with the results from the $\pi^+\Delta^0$ beam spin asymmetry analysis. Later on, the extraction of the polarized cross-section from the beam spin asymmetry is explained. Final results with respect to $-t$ and Q^2 are shown and also a comparison with existing measurements from Hall C and CLAS12 is made. The systematic uncertainty studies are described and estimated systematic errors are outlined. Finally, the possible future studies are described before the overall conclusion.

5.1 $t-\phi$ Binning

As discussed in Section 4.4, the missing mass study is done using a number of simulated processes. The shape of the missing mass distribution changes for different t and ϕ bins. First, the event selection and PID cuts (listed in Chapter 3) are applied to get a clean sample of pion electroproduction events. Then, random coincidence events are subtracted. This procedure is separately done for the liquid hydrogen data and the aluminum (dummy) target data. The contribution from the aluminum walls of the hydrogen target is removed by subtracting the charge normalized yields of the aluminum target from the hydrogen target.

The data are then binned in t, where a missing mass cut around the Δ^0 is applied

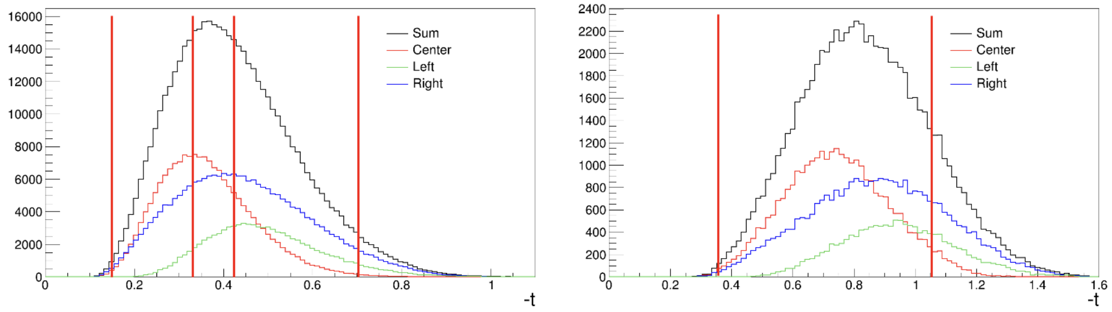

Figure 5.1: Distribution of $-t$ for Δ^0 events (including backgrounds) for $Q^2 = 3.0$ GeV^2, $W = 3.14$ GeV (left) and $Q^2 = 5.5$ GeV^2, $W = 3.02$ GeV (right) with three SHMS settings. The vertical lines correspond to the bin boundaries where left and right regions are excluded from the analysis.

in addition to the other cuts. This data sample includes all the pion background processes as the missing mass shape study is done after binning. During the t binning, three important criteria were considered. The first criterion was to have similar number of events in different bins within each kinematic setting. The second was to make sure that the three SHMS settings together should give a full ϕ coverage. The third was to exclude the higher $-t$ region where Δ^0 events are negligible, this excluded events at very high $-t$. Fig. 5.1 shows the $-t$ distribution where the left plot corresponds to a high statistic kinematic setting and the right plot corresponds to a low statistic kinematic setting. The vertical lines correspond to the t bin limits.

After t bin selection, the missing mass distributions are plotted for each t bin.

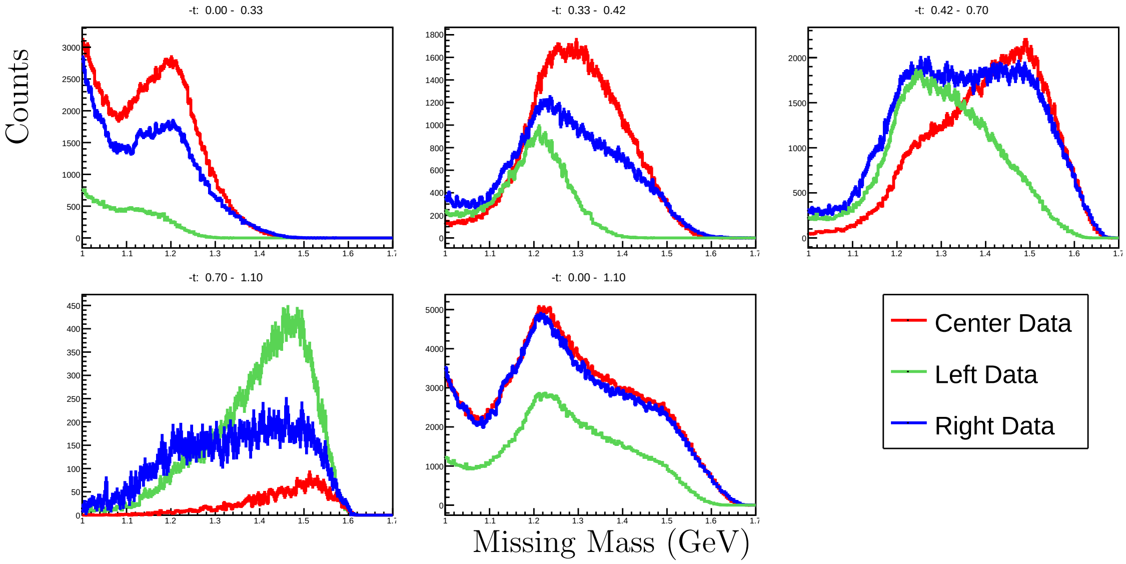

Figure 5.2: Missing mass distribution for different t bins in the region of Δ^0 ($Q^2 = 3.0$ GeV^2, $W = 3.14$ GeV). Different colors correspond to three SHMS angle settings.

Fig. 5.2 shows these missing mass distributions in the Δ^0 region. It can be seen that the first t bin is dominated by Δ^0 events (signal), the second and third t bin has more contribution from SIDIS events (background) and the final t bin has negligible signal events. This shows that the signal-to-background ratio changes with respect to t. The top three plots correspond to the t region which was included in this analysis and the bottom left plot corresponds to the exclusion region. The bottom center plot corresponds to the missing mass distribution covered by all the data with no t cut. The exclusion region varies for each kinematic setting because the t coverage is different for each kinematic setting. By excluding this region, both the background process contamination and the associated systematic uncertainty is reduced. The final physics results have three t bins for the high statistic kinematic settings and one or two t bins for the low statistic kinematic settings.

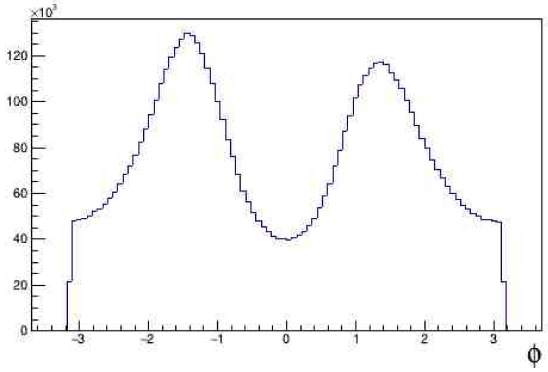

Figure 5.3: Distribution of ϕ for Δ^0 events (including backgrounds) for $Q^2 = 3.0$ GeV^2, $W = 3.14$ GeV. The ϕ distribution is divided into 8 equal size bins

Fig. 5.3 shows a one-dimensional ϕ distribution. For the ϕ bins, the data is divided into eight equal size bins because the fitting of the sinϕ dependence requires a minimum of 8 bins. The amplitude of sinϕ is difficult to extract with a lower number of ϕ bins. The limited Δ^0 statistics preclude finer ϕ binning. The ϕ binning is done separately for each SHMS setting and the yields are calculated by integrating the missing mass distribution, after the background subtraction, in the Δ^0 region (1.11-1.4 GeV). Fig. 5.4 shows the kinematic coverage of data for t and ϕ after combining the three SHMS angle settings.

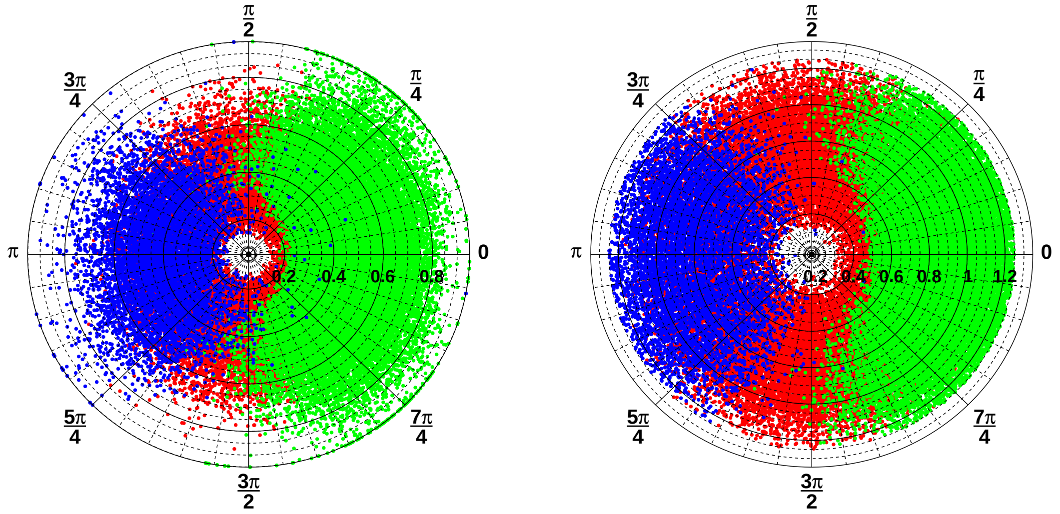

Figure 5.4: A two dimensional distribution of $-t$ (radial axis) and ϕ (azimuthal axis) for $Q^2 = 3.0$ GeV^2 (left) and $Q^2 = 5.5$ GeV^2 from the Kaon-LT experiment. The three colors correspond to three SHMS angle settings where red corresponds to center setting, blue corresponds to left setting and green corresponds to right setting.

5.2 Beam Spin Asymmetry

The beam spin asymmetry provides clean access to the polarized cross-section $\sigma_{LT'}$ (see Eq. 1.3). The BSA is the difference in fractional cross-section based on the helicity of the incident electron. The positive helicity corresponds to the spin of incident electron parallel to the direction of motion and negative helicity corresponds to the spin of the incident electron anti-parallel to the direction of motion. The general relation for beam spin asymmetry A_{LU} is given by:

$$A_{LU} = \frac{1}{P}\left(\frac{\sigma^{+} - \sigma^{-}}{\sigma^{+} + \sigma^{-}}\right) \tag{5.42}$$

Here, L and U refer to longitudinally polarized electron beam and unpolarized target, P is the polarization of the electron beam which is measured at the source and precessed to Hall C to give the polarization at the target (as described in Section 2.2.6). σ^{+} and σ^{-} correspond to the cross-sections for positive and negative helicity states. Since the asymmetry is a ratio of cross-sections, the correction factors (efficiencies, target boiling etc) cancel provided the helicity dependence in these quantities is small. This is true in the absence of the application of radiative corrections. These cross-sections (σ^{+} and σ^{-}) can therefore be replaced by experimental yields (Y). During the Kaon-LT experiment, the helicity correlated charge measurement was unavailable, but this charge asymmetry is considered very small ($< 0.1\%$) [61]. Additionally, a non-zero charge asymmetry should result in an offset in the ϕ-dependent asymmetry, so adding an offset as a fit parameter would allow a constraint on the charge asymmetry. The above relation can be rewritten as:

$$A_{LU} \ = \ \frac{1}{P}\left(\frac{Y^{+} \ - \ Y^{-}}{Y^{+} \ + \ Y^{-}}\right) \tag{5.43}$$

5.2.1 $\pi^{+}\Delta^{0}$ Asymmetry

The yields are calculated by integrating the background subtracted data in the Δ^0 missing mass region. This is separately done for each $-t$ and ϕ bin as well as each SHMS setting. These yields are used to calculate A_{LU} for each SHMS setting separately. These three SHMS settings are then combined through error weighted average to get the total A_{LU} for a given t, ϕ bin. Figures 5.5 and 5.6 show the results for beam spin asymmetry, where a clear sinusoidal distribution can be observed across all kinematic settings. The amplitude of sinϕ fit is extracted from $A_{LU}^{sin\phi}$ for each t-bin. The other moments (as shown in [25]) cannot be extracted for this analysis, due to low statistics, as it requires finer ϕ binning. The statistical uncertainty is given by:

$$\delta_{stat.} \ = \ \frac{2}{P}\sqrt{\frac{(Y^{+} \ . \ Y^{-})}{(Y^{+} \ + \ Y^{-})^{3}}} \tag{5.44}$$

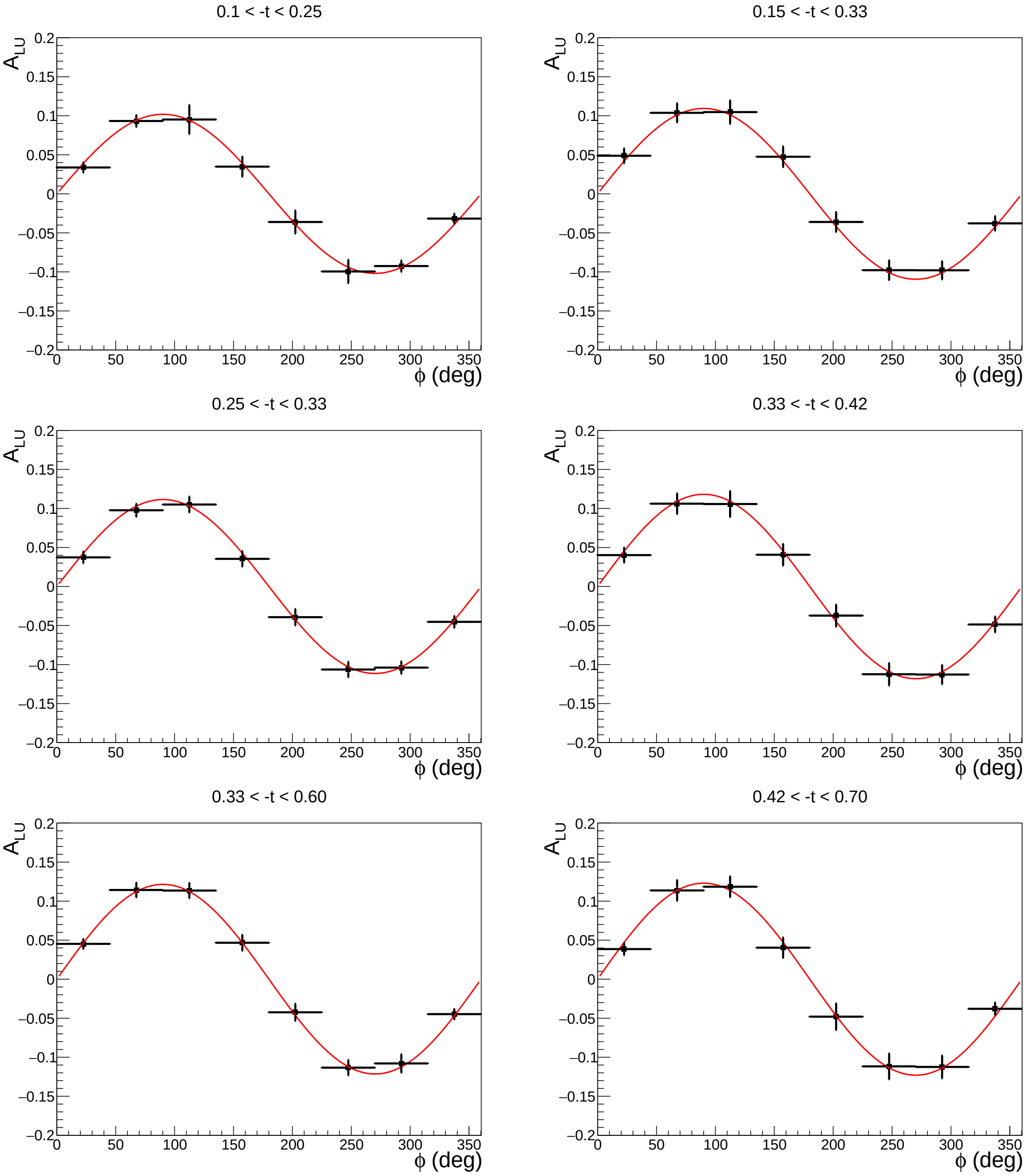

Figure 5.5: Distribution of beam spin asymmetry (A_{LU}) v/s ϕ for $Q^2 = 2.1\ GeV^2, W = 2.95\ GeV$ (left column) and $Q^2 = 3.0\ GeV^2, W = 3.14\ GeV$ (right column) for different $-t$ bins.

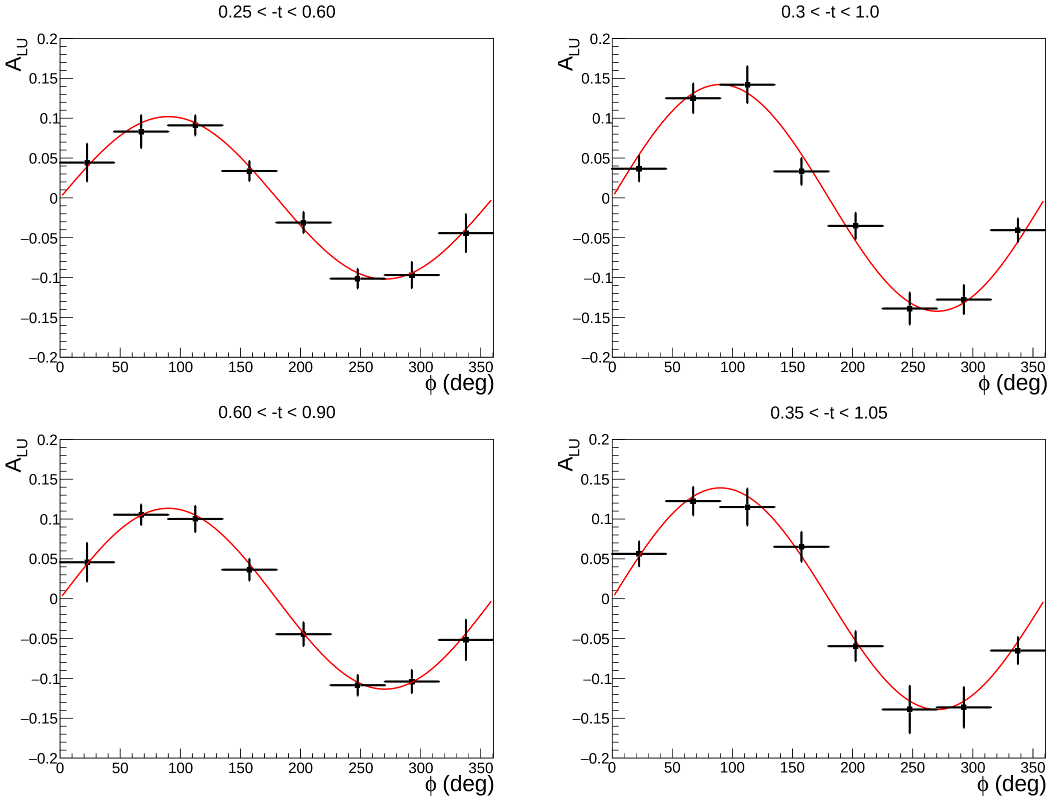

Figure 5.6: Distribution of beam spin asymmetry (A_{LU}) v/s ϕ for $Q^2 = 3.0\ GeV^2, W = 2.32\ GeV$ (left column), $Q^2 = 4.4\ GeV^2, W = 2.74\ GeV$ (top right) and $Q^2 = 5.5\ GeV^2, W = 3.02\ GeV$ (bottom right).

5.3 Cross-Section Ratio ($\sigma_{LT'}/\sigma_0$)

The cross-section ratio $\sigma_{LT'}/\sigma_0$ can be extracted from the beam spin asymmetry, since A_{LU} is directly proportional to the cross-section ratio. The magnitude of the $sin\phi$ fit is related to the cross-section ratio as follows:

$$A_{LU}^{sin\phi} = \sqrt{2\epsilon(1 - \epsilon)}\frac{d\sigma_{LT'}}{d\sigma_0} \tag{5.45}$$

where

- ϵ is the polarization of virtual photon (values listed in Table 2.9).
- σ_0 is the unpolarized cross-section.

Fig. 5.7 shows the t dependence of the cross-section ratio for a wide range of kinematics. The t-dependence of the cross-section is important as it is sensitive to the reaction mechanism (as described in Section 1.2). The pion pole process (as

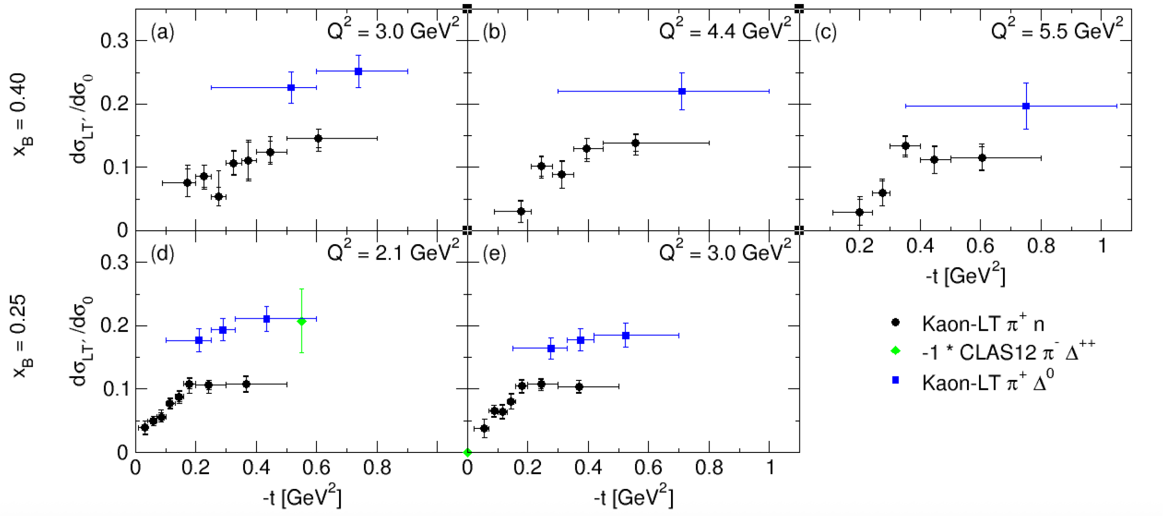

Figure 5.7: Results for cross-section ratio $\sigma_{LT'}/\sigma_0$ with respect to $-t$. The bottom two panels are higher statistics settings with x$_B$ = 0.25 and top three panels are lower statistics settings with x$_B$ = 0.40.

described in Chapter 1) is expected to contribute more strongly at low $-t$. The $\pi^+\Delta^0$ cross-section ratio is compared with results for the π^+n final state from the same experiment [62] and to the $\pi^-\Delta^{++}$ measurement from CLAS12 [23]. The results show that even though the t binning for Δ^0 is coarse as compared to the ground state neutron reaction, both show similar trends with the cross-section ratio increasing at high $-t$. It can also be observed that the polarized cross-section magnitude is approximately double for the Δ^0 reaction as compared to the ground state neutron reaction. The x_B dependence, between top row and the bottom row plots appear to be flat for the cross-section ratio.

Fig. 5.8 shows the Q^2 dependence of the cross-section ratio. The Q^2 dependence is also important, as it can explain the change in polarized cross-section ($\sigma_{LT'}$) with respect to change in unpolarized cross-section (σ_0). As shown in the figure, $\pi^+\Delta^0$

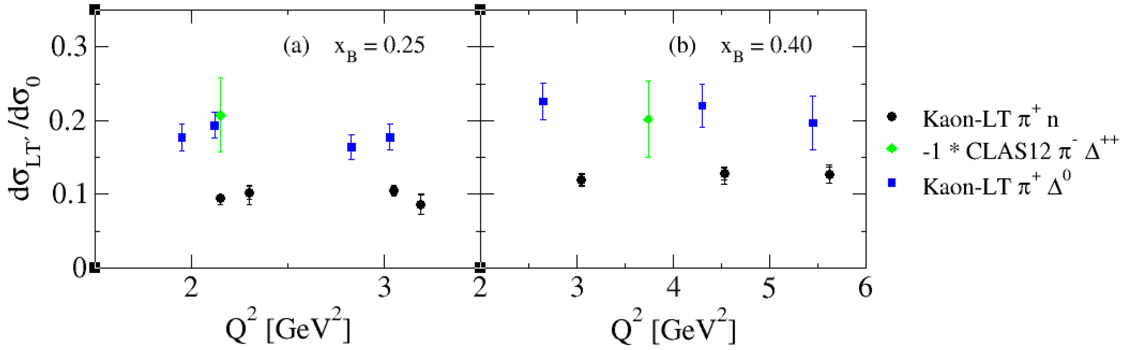

Figure 5.8: Results for the cross-section ratio $\sigma_{LT'}/\sigma_0$ with respect to Q^2. The two plots corespond to data at two different values of x_B.

results are also compared with $\pi^+ n$ reaction from the same experiment and the $\pi^- \Delta^{++}$ reaction from CLAS12. The results confirm that the cross-section ratios for Δ^0 are larger than the ground state neutron reaction but similar in magnitude to the CLAS12 results. It is also important to mention that the polarized cross-section results from CLAS12 are negative and a factor of -1 is multiplied in both figures to compare the

Q^2_{mean}	$-t_{mean}$	$A_{LU}^{sin\phi}$	δ_{stat}	ϵ	$\frac{d\sigma_{LT'}}{d\sigma_0}$	δ_{stat}
1.95	0.21	0.102	0.010	0.79	0.177	0.018
2.12	0.289	0.111	0.010	0.79	0.183	0.018
2.31	0.434	0.121	0.011	0.79	0.211	0.019
2.83	0.276	0.109	0.011	0.67	0.165	0.017
3.03	0.374	0.118	0.012	0.67	0.178	0.018
3.23	0.524	0.123	0.012	0.67	0.185	0.019
2.65	0.515	0.102	0.011	0.885	0.226	0.025
2.99	0.738	0.113	0.012	0.885	0.252	0.026
4.30	0.71	0.141	0.019	0.715	0.220	0.030
5.45	0.751	0.139	0.025	0.525	0.197	0.036

Table 5.1: Final results for beam spin asymmetry and cross-section ratio for all data. An estimate of systematic errors are given in Table 5.2.

magnitude of the cross-section ratio. The amplitudes for the two Δ processes are related by isospin symmetry and have a sign change [22]. The cross-section ratio is flat with respect to Q^2 for both values of x_B which means that polarized cross-section ($\sigma_{LT'}$) falls at the same rate as the unpolarized cross-section (σ_0). Table 5.1 list the final results including the mean kinematics.

5.4 Error Analysis

The error analysis for this work is categorized into two main types: statistical errors and systematic errors. The statistical errors have been included in the results shown in the previous section, providing a measure of the variability in the data due to limited statistics. However, systematic errors, which arise from various experimental and methodological factors, are yet to be fully quantified. The estimation of systematic uncertainties for the cross-section ratios is an ongoing effort.

The systematic uncertainty study will be conducted separately for each kinematic setting, ensuring a comprehensive understanding of the behavior of systematic effects across different experimental conditions. Each source of systematic uncertainty will be analyzed independently, and a total systematic error will be evaluated based on the observed trends and their contributions. The systematic error analysis is divided into three primary sub-categories:

Cut-Dependent Systematic Uncertainty

Cut-dependent systematic uncertainty arises from variations in the selection criteria applied during data analysis. Since these selection criteria significantly impact the final event sample, their influence on the extracted physics observables must be thoroughly examined. The approach to evaluating cut-dependent systematics involves varying one cut at a time while keeping others fixed and recalculating the beam spin asymmetry and the polarized cross-section ratio for each variation. The two most critical cut variations considered in this study are:

- **Number of Photoelectrons in the SHMS Heavy Gas Cherenkov:** The SHMS Heavy Gas Cherenkov (HGC) detector plays a crucial role in particle identification (PID) by distinguishing pions from protons and kaons. Since exclusive pion electroproduction with a Δ^0 final state heavily relies on accurate pion selection, variations in the HGC threshold can introduce systematic uncertainties. The default threshold for the number of detected photoelectrons was set to 2.0. To assess systematic effects, this threshold is increased to 3.0. Higher values are avoided as they would significantly reduce statistics, increasing statistical uncertainty. Lowering the threshold is also not practical, as it would introduce kaon contamination, thereby affecting the purity of the pion sample.

- **Missing Mass Cut Variation:** The selection of the Δ^0 final state is sensitive to the missing mass cut, which is applied after background subtraction. To evaluate its impact, the missing mass cut is varied by ±10%, creating two scenarios: one with a 10% wider cut and another with a 10% narrower cut. A larger variation is avoided, as it would introduce unwanted background contamination from other pion production processes.

- **Other Cut Considerations:** Additional selection criteria, such as coincidence time selection, are expected to have minimal impact on final yields ($< \pm 1\%$). However, their influence will be briefly assessed to ensure they do not introduce significant systematic biases.

A similar cut-dependent study was performed during the beam spin asymmetry and cross-section ratio analysis for the ground state $\pi^+ n$ analysis [62] from the same experiment. Based on the results from that analysis, the total cut-dependent systematic error for the $\pi^+\Delta^0$ analysis is estimated to be ±5%.

Simulation Fitting Systematic Uncertainty

Systematic uncertainties related to simulation fitting are expected to be among the most significant sources of systematic error in this work. These uncertainties arise from the procedure used to model and fit background contributions in the missing mass spectrum. The systematic uncertainty from simulation fitting is evaluated through two distinct methods:

- **Measurement of Missing Mass Residual:** The first method involves quantifying the discrepancy between total experimental data yields and those predicted by all simulated processes. The underlying assumption is that any systematic differences between the two arise from imperfections in the simulation model or background subtraction procedure. Fig. 5.9 shows the missing mass residual where the combined simulation distribution is subtracted from the experimental data. The discrepancies are examined within the missing mass integration region to ensure they are relevant to the extracted Δ^0 yields. Any differences outside this integration region are not included in the uncertainty

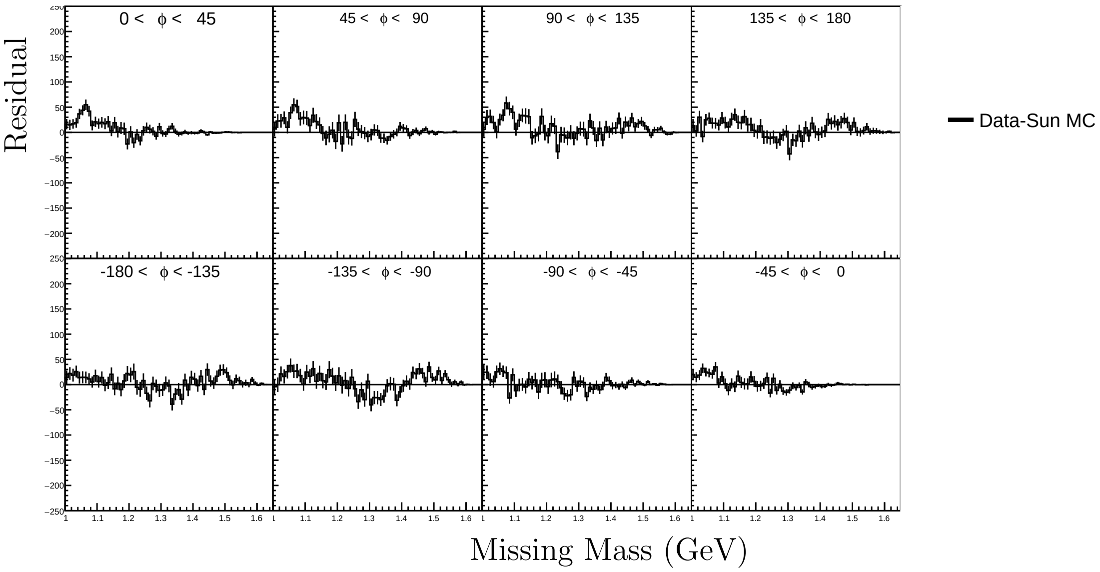

Figure 5.9: Missing mass distribution after all simulated processes are subtracted in the region of Δ^0 for center setting data in each ϕ bin ($Q^2 = 4.4$ GeV^2, $W = 2.74$ GeV).

estimation.

- **Comparison of Signal and Background Asymmetry:** The second method assesses the systematic uncertainty introduced by background contamination in the Δ^0 asymmetry. This is done by measuring the total background asymmetry in the Δ^0 missing mass integration region. Fig. 5.10 shows the beam spin asymmetry of the background for one kinematic setting. The comparison between the signal and background asymmetry shows that the sinϕ amplitude is comparable. This means that any contamination of background in the Δ^0 region does not change the Δ^0 asymmetry.

Based on the preliminary results for one kinematic setting and systematic error

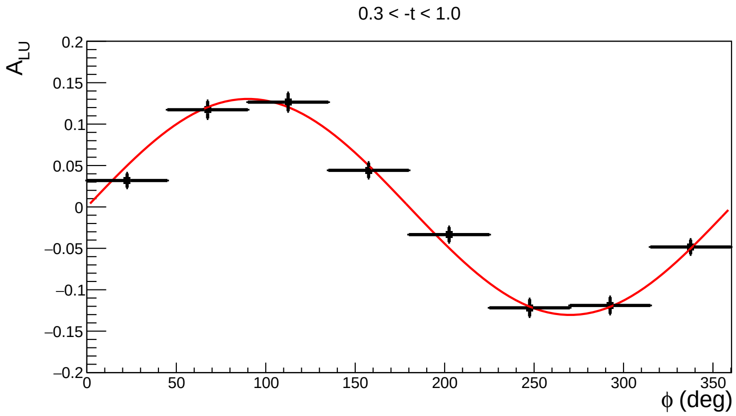

Figure 5.10: Distribution of background beam spin asymmetry (A_{LU}) v/s ϕ for $Q^2 = 4.4\ GeV^2, W = 2.74\ GeV$. This is calculated for the total background in the Δ^0 region (1.11-1.4 GeV).

study done for the CLAS12 $\pi^-\Delta^{++}$ analysis [23], the total simulation fitting systematic error for this analysis is estimated to be ±12%. To further refine this systematic uncertainty evaluation, variations in error across different kinematic settings will be studied to determine whether they exhibit point-to-point fluctuations, random variations, or a consistent pattern. Identifying the nature of these variations is essential for appropriately combining simulation fitting systematics with other sources of uncertainty in the total systematic error estimation.

Beam Polarization Uncertainty

The beam polarization uncertainty arises from limitations in the precision of beam polarization measurement during the experiment. Unlike other systematic uncertainties, this error remain is constant across all kinematic settings and does not require separate evaluation for each data point. The beam polarization was measured during the experiment data taking, and the associated uncertainty was determined as part of that measurement process, as described in Section 2.2.6. It is important to note that this uncertainty is asymmetric. The asymmetry arises due to different components of the beam polarization uncertainty. This uncertainty arises from a combination of LINAC imbalance, beam energy loss and erro in the measurement of beam polarization. This error will be taken into account when propagating uncertainties into the final cross-section ratios and beam spin asymmetry measurements.

It is important to mention that the experimental correction factors (detector efficiencies, target boiling etc) are expected to cancel in the ratio of the beam spin asymmetry calculation. Furthermore, the electron beam charge asymmetry is expected to be negligible, therefore they are not included in the final systematic error. Table 5.2 lists estimated systematic uncertainties for one kinematic setting ($Q^2 = 4.4\ GeV^2$, $W = 2.74\ GeV$). It is anticipated that the systematic errors for the other settings will be similar. The final systematic errors for all kinematic settings will be completed before the publication.

Kinematics	Cut-dependent	Fitting	Beam Pol.
$Q^2 = 4.30$	$\pm 5\%$	$\pm 12\%$	$+1\%$
$-t_{mean} = 0.71$			-3%

Table 5.2: A breakdown of different systematic uncertainties for $Q^2 = 4.4\ GeV^2$, $W = 2.74\ GeV$. The cut-dependent and fitting systematic errors are estimated.

5.5 Conclusion

The three-dimensional structure of hadrons remains an open question in modern nuclear and particle physics. Despite significant theoretical advancements, the internal structure of nucleons and their transitions to excited states are not fully understood. One of the major challenges is the validation of QCD factorization in exclusive processes, where different theoretical approaches, such as the Generalized Parton Distributions framework and the Regge approach, provide differing predictions. Experimental verification of these frameworks is crucial for advancing our understanding of non-perturbative QCD. In exclusive meson electroproduction reactions, the transition from a nucleon to its first excited state, the Δ resonance, has not been extensively studied. Transition GPDs, which encode information about the spatial and momentum distributions of quarks during such transitions, suffer from large theoretical uncertainties due to the lack of experimental constraints. Therefore, experimental measurements are essential to improve our understanding of transition GPDs and to provide input for refining theoretical models.

In this thesis, hadron structure has been investigated through the exclusive pion electroproduction reaction, which serves as an essential probe in understanding QCD dynamics. The pion, as the lightest meson, plays a fundamental role in chiral symmetry breaking and the strong interaction. Exclusive reactions, where all final-state particles are identified, provide a clean and precise way to study hadronic structure. This thesis presents the first-ever beam spin asymmetry measurement of exclusive pion electroproduction with the $\pi^+\Delta^0$ final state over a wide range of kinematic variables (Q^2, W, and $-t$). The beam spin asymmetry for the Δ^0 reaction has been measured, and the polarized cross-section ratio ($\sigma_{LT'}/\sigma_0$) has been extracted. The

t-dependence of the cross-section ratio provides insight into the reaction mechanism and tests the pion pole contribution, while the Q^2 dependence helps to assess the rate of change in polarized cross-section in comparison with respect to unpolarized cross-section.

The Kaon-LT experiment was one of the commissioning experiments in Hall C at Jefferson Lab following the 12 GeV energy upgrade. It was among the first experiments to utilize a coincidence trigger configuration in Hall C. The experiment was conducted over three separate run periods; however, the physics results presented in this thesis are based on data from the first run period, which had the highest electron beam energy. A substantial effort was made to understand the performance of the newly commissioned Super High Momentum Spectrometer (SHMS), ensuring its reliability for future experiments. These studies were completed for all three run periods, spanning electron beam energies from 3.8 to 10.6 GeV.

Extensive studies were carried out on all experimental systems in Hall C as part of this thesis work. The performance of the electron beam delivered to Hall C, the liquid and solid targets, the magnet systems in both spectrometers, and all the detectors were thoroughly analyzed. Particular attention was given to optimizing the tracking algorithm across a wide range of rates and particle species. These optimizations led to significant improvements in tracking efficiency, which have since been adopted by other experiments in Hall C. Additionally, the performance of particle identification detectors was carefully examined, leading to accurate particle identification and event selection. The data acquisition system was also studied in detail under various experimental conditions to ensure optimal performance.

A simulation-driven approach was employed to isolate exclusive $\pi^+\Delta^0$ events. Several pion processes were simulated to estimate background contributions accurately. A discrepancy in resolution between data and simulation was identified, prompting a resolution correction study that has since been incorporated into the standard Hall C simulation package. Furthermore, experimental kinematic offsets were determined by comparing data with simulations using well-known elastic e-p scattering cross-sections. This calibration enhanced confidence in the experimental apparatus and minimized systematic uncertainties in the final measurements.

The final physics results of this study focus on the exclusive $\pi^+\Delta^0$ reaction, where the beam spin asymmetry A_{LU} was measured with a longitudinally polarized electron beam and an unpolarized proton target. The results exhibit a clear $\sin\phi$ dependence across a broad range of kinematics, confirming the expected behavior of beam spin asymmetry. The polarized cross-section ratio ($\sigma_{LT'}/\sigma_0$) was extracted from the beam spin asymmetry and analyzed as a function of t and Q^2. The results were compared to measurements from the same experiment for the ground-state nucleon and to the exclusive $\pi^-\Delta^{++}$ reaction measured at CLAS12. The comparison reveals that the magnitude of the cross-section ratio ($\sigma_{LT'}/\sigma_0$) is approximately twice that of the ground-state nucleon reaction, while it is similar in magnitude to the CLAS12 results. The observed difference in sign between the two measurements is consistent with isospin symmetry considerations. While limited statistics prevent a definitive conclusion about the t-dependence, the observed trend aligns with expectations (cross-section ratio is expected to increase as a function of t at fixed Q^2 and W). The flat Q^2 dependence suggests that the polarized cross-section falls at the same rate as the unpolarized cross-section.

This work provides clear evidence that the exclusive $\pi^+\Delta^0$ reaction can be successfully studied in Hall C at Jefferson Lab. Despite the experiment not being specifically designed to investigate this reaction, meaningful results were obtained, demonstrating the potential for future measurements with improved statistics and dedicated experimental configurations. These findings lay the groundwork for future investigations into transition GPDs and hadron structure, contributing to our broader understanding of QCD and the nucleon-to-resonance transitions.

5.6 Future Work

The work presented in this thesis lays a strong foundation for the study of exclusive pion electroproduction reaction, but several avenues remain for further exploration.

These include ongoing systematic studies, additional analysis using existing experimental data, and future experiments designed to provide a deeper understanding of hadron structure within the framework of QCD.

One of the major ongoing efforts is the detailed study of systematic uncertainties associated with the beam spin asymmetry and polarized cross-section ratio measurements for the exclusive $\pi^+\Delta^0$ reaction. This includes identifying and quantifying different sources of systematic errors. A cut-dependent study is being conducted to assess the sensitivity of results to event selection criteria, while another study evaluates the uncertainties introduced by the simulation-driven background subtraction method for the exclusive $\pi^+\Delta^0$ process. Additionally, uncertainty contributions from the beam polarization measurement will be incorporated into the total systematic uncertainty. These systematic studies are critical for finalizing the measurements with high precision and will be completed before the publication.

Beyond the current work, the existing experimental data can be further analyzed to extract new physics results. Theoretical models for transition GPDs indicate that experimental input is essential for reducing uncertainties and improving model constraints. One important step in this direction is the study of the neutron-to-Δ ratio for total unseparated cross-sections. To achieve this, an initial analysis can integrate over the azimuthal angle ϕ and extract a finer t-dependence of the unseparated cross-section. The high-ϵ data can be analyzed first, followed by the inclusion of low-ϵ data to enable an ϵ-dependence study of the unseparated cross-section from two different reactions.

Additionally, a longitudinal/transverse (L/T) separated cross-section analysis can be performed for the ground state π^+n reaction. This is feasible due to the relatively high statistics of the exclusive π^+n reaction in the collected dataset. The analysis requires both high-ϵ and low-ϵ data and will allow a detailed t-dependence study of the separated cross-sections. Such a study can provide further insights into the reaction mechanism and allow for a precise test of the pion pole for the ground state nucleon. Furthermore, the pion form factor can be extracted from the separated longitudinal cross-section using models. This will represent the first measurement of the pion form factor at these kinematics, offering new insights into the transverse spatial distribution of partons and testing QCD factorization in this kinematic regime.

While the existing data offer valuable opportunities for further analysis, some critical aspects of transition GPD studies require new experimental data. A dedicated experiment focused on the exclusive $\pi^+\Delta^0$ reaction in Hall C would be essential for advancing our understanding of nucleon-to-resonance transitions. Such an experiment could significantly extend the kinematic range, allowing for a rigorous test of reaaction mechanism at high kinematics. Additionally, acquiring high statistics for the current kinematic range would enable a full L/T separation for the transition reaction, further enhancing our understanding of hadron structure through transition GPDs. The current data demonstrated that the ground state $\pi^+ n$ is the dominant background in the region $|t| < 0.45$ GeV^2 whereas SIDIS is the dominant background in the region $|t| > 0.45$ GeV^2. In order perform a full L/T separation for the exclusive $\pi^+\Delta^0$ process, a future experiment should consider taking 300,000 total events for each kinematic setting, which will result in $\approx$ 100,000 Δ^0 events. In order to test the pion pole for the Δ^0 resonance, it's also important to collect data near the t_{min}.

Future experiments will play a crucial role in hadron structure studies, particularly in improving our understanding of transition GPDs. A dedicated experiment in Hall C will provide a unique testing ground for hadron structure studies, helping to address key open questions in the field and significantly advancing the understanding of nucleon-to-resonance transitions within the QCD framework.

Bibliography

[1] P Achenbach et al. The present and future of QCD. *Nuclear Physics A*, 1047:122874, 2024.

[2] K Nakamura, C Amsler, Particle Data Group, et al. Particle Physics Booklet. *Journal of Physics G: Nuclear and Particle Physics*, 37(7A):075021, 2010.

[3] John Arrington et al. Revealing the structure of light pseudoscalar mesons at the electron-ion collider. *Journal of Physics G: Nuclear and Particle Physics*, 48(7):075106, 2021.

[4] Hideki Yukawa. On the interaction of elementary particles I. *Proceedings of the Physico-Mathematical Society of Japan. 3rd Series*, 17:48–57, 1935.

[5] Cesare Mansueto Giulio Lattes, Giuseppe PS Occhialini, and Cecil Frank Powell. Observations on the tracks of slow mesons in photographic emulsions. *Nature*, 160(4067):486–492, 1947.

[6] SR Amendolia et al. A measurement of the pion charge radius. *Physics Letters B*, 146(1-2):116–120, 1984.

[7] P Brauel et al. Electroproduction of π^+n, π^-p and $K^+\Lambda$ final states above the resonance region. *Zeitschrift für Physik C Particles and Fields*, 3(2):101–123, 1979.

[8] GM Huber et al. Charged pion form factor between $Q^2 = 0.60$ and 2.45 GeV^2. II. Determination of, and results for, the pion form factor. *Physical Review C*, 78(4):045203, 2008.

[9] HP Blok et al. Charged pion form factor between $Q^2 = 0.60$ and 2.45 GeV^2. I. Measurements of the cross section for the ^{1}H$(e, e^{'}\pi^+)n$ reaction. *Physical Review C*, 78(4):045202, 2008.

[10] John C Collins, Davison E Soper, and George Sterman. Factorization for short distance hadron-hadron scattering. *Nuclear Physics B*, 261:104–142, 1985.

[11] JM Laget. Exclusive meson photo-and electro-production, a window on the structure of hadronic matter. *Progress in Particle and Nuclear Physics*, 111:103737, 2020.

[12] M Vanderhaeghen, M Guidal, and J-M Laget. Regge description of charged pseudoscalar meson electroproduction above the resonance region. *Physical Review C*, 57(3):1454, 1998.

[13] D Dreschsel and Lothar Tiator. Threshold pion photoproduction on nucleons. *Journal of Physics G: Nuclear and Particle Physics*, 18(3):449, 1992.

[14] LN Hand. Experimental investigation of pion electroproduction. *Physical Review*, 129(4):1834, 1963.

[15] John C Collins. Hard-scattering factorization with heavy quarks: A general treatment. *Physical Review D*, 58(9):094002, 1998.

[16] Andrei V Belitsky and AV Radyushkin. Unraveling hadron structure with generalized parton distributions. *Physics reports*, 418(1-6):1–387, 2005.

[17] Peter Donald Bruce Collins. *An introduction to Regge theory and high energy physics*. Cambridge University Press, 1977.

[18] Pierre AM Guichon and Marc Vanderhaeghen. Virtual Compton scattering off the nucleon. *Progress in Particle and Nuclear Physics*, 41:125–190, 1998.

[19] J-M Laget. Photoproduction of vector mesons at large momentum transfer. *Physics Letters B*, 489(3-4):313–318, 2000.

[20] Markus Diehl. Generalized parton distributions. *Physics Reports*, 388(2-4):41–277, 2003.

[21] Xiangdong Ji. Gauge-invariant decomposition of nucleon spin. *Physical Review Letters*, 78(4):610, 1997.

[22] Peter Kroll and Kornelija Passek-Kumerički. Transition GPDs and exclusive electroproduction of π-Δ (1232) final states. *Physical Review D*, 107(5):054009, 2023.

[23] S. Diehl et al. First Measurement of Hard Exclusive $\pi^-\Delta^{++}$ Electroproduction Beam-Spin Asymmetries off the Proton. *Phys. Rev. Lett.*, 131(2):021901, 2023.

[24] V. D. Burkert et al. The CLAS12 Spectrometer at Jefferson Laboratory. *Nucl. Instrum. Meth. A*, 959:163419, 2020.

[25] S. Diehl et al. A multidimensional study of the structure function ratio $\sigma_{LT'}/\sigma_0$ from hard exclusive π^+ electro-production off protons in the GPD regime. *Phys. Lett. B*, 839:137761, 2023.

[26] A. Kim et al. Beam spin asymmetry measurements of deeply virtual π^0 production with CLAS12. *Phys. Lett. B*, 849:138459, 2024.

[27] Elliott D Bloom et al. High-Energy Inelastic e-p Scattering at 6 and 10. *Physical Review Letters*, 23(16):930, 1969.

[28] SA Wood et al. Jeffereson Lab Hall C Standard Equipment Manual. *Thomas Jefferson National Accelerator Facility (TJNAF) Tech. Report*, 2017.

[29] Christoph W Leemann, David R Douglas, and Geoffrey A Krafft. The Continuous Electron Beam Accelerator Facility (CEBAF) at the Jefferson Laboratory. *Annual Review of Nuclear and Particle Science*, 51(1):413–450, 2001.

[30] RD McKeown. The jefferson lab 12 GeV upgrade. *American Institute of Physics Conference Proceedings*, 1374(1):121–126, 2011.

[31] Charles E Reece. Continuous wave superconducting radio frequency electron linac for nuclear physics research. *Physical Review Accelerators and Beams*, 19(12):124801, 2016.

[32] Fulvia C Pilat. The 12 GeV energy upgrade at Jefferson Laboratory. *Thomas Jefferson National Accelerator Facility (TJNAF) Tech. Report*, 2012.

[33] Carlos Yero (PhD Thesis). Cross section measurements of deuteron electro-disintegration at very high recoil momenta and large 4-momentum transfers (Q^2). *Florida International University*, 2020.

[34] Burcu Duran (PhD Thesis). The J/ψ-007 Experiment: A Search for the LHCb Charm Pentaquarks in Hall C at Jefferson Lab. *Temple University*, 2021.

[35] C Yan, R Carlini, and D Neuffer. Beam energy measurement using the arc beam line as a spectrometer. *Thomas Jefferson National Accelerator Facility (TJNAF) Tech. Report*, 1993.

[36] Tanja Horn (PhD Thesis). The pion charge form factor through pion electroproduction. *University of Maryland*, 2006.

[37] KB Unser. The parametric current transformer, a beam current monitor developed for LEP. *American Institute of Physics Conference Proceedings*, 1992.

[38] DJ Mack. Beam current monitors for Hall C. *American Institute of Physics Conference Proceedings*, 1992.

[39] W-M Yao. 1 and 2007 partial update for the 2008 edition available on the PDG WWW pages. *J. Phys. G*, 2006.

[40] D. Gaskell and S. Wood. Private Communication. *Thomas Jefferson National Accelerator Facility (TJNAF)*, 2023.

[41] Dave Meekins. Hall C target configuration (8-9-2017). *Thomas Jefferson National Accelerator Facility (TJNAF) Tech. Report*, 2017.

[42] John Arrington et al. The Science and Experimental Equipment for the 12 GeV Upgrade of CEBAF. *Thomas Jefferson National Accelerator Facility (TJNAF) Tech. Report*, 2005.

[43] M. Fowlerl and T. Horn. HMS Magnet Control System and How to. *Thomas Jefferson National Accelerator Facility (TJNAF) Tech. Report*, 2009.

[44] T Horn et al. The Aerogel Čerenkov detector for the SHMS magnetic spectrometer in Hall C at Jefferson Lab. *Nuclear Instruments and Methods in Physics Research Section A: Accelerators, Spectrometers, Detectors and Associated Equipment*, 842:28–47, 2017.

[45] T Horn, GM Huber, P Markowitz, et al. Study of the L-T Separated Kaon Electroproduction Cross Section from 5-11 GeV. *Jefferson National Accelerator Facility PAC 36*, 2009.

[46] M. Jones et al. HCANA Github - https://github.com/JeffersonLab/hcana/. *Thomas Jefferson National Accelerator Facility (TJNAF)*, 2009.

[47] Rene Brun and Fons Rademakers. ROOT—An object oriented data analysis framework. *Nuclear instruments and methods in physics research section A: accelerators, spectrometers, detectors and associated equipment*, 389(1-2):81–86, 1997.

[48] O. Henson et al. Hall A Analyzer (PODD) - https://redmine.jlab.org/projects/podd/wiki. *Thomas Jefferson National Accelerator Facility (TJNAF)*, 2009.

[49] Ali Usman. Update on Kaon-LT Experiment. *Thomas Jefferson National Accelerator Facility (TJNAF) Winter Meeting Proceedings*, 2021.

[50] Vijay Kumar (PhD Thesis). Measurement of the Pion Exclusive Electroproduction Cross-Section in the E12-19-006 Experiment in Hall-C at Jefferson Lab. *University of Regina*, 2024.

[51] Richard Trotta (PhD Thesis). Determination of Pion and Kaon Structure Using the Sullivan Process at Moderate to large Fractional Momentum. *The Catholic University of America*, 2024.

[52] S. Kay. Cointime Peak Stability Studies. *Thomas Jefferson National Accelerator Facility (TJNAF) Tech. Report*, 2020.

[53] Dave Gaskell and John Arrington. SIMC - Physics Monte Carlo for Hall C and Hall A. *Thomas Jefferson National Accelerator Facility (TJNAF) Tech. Report*, 2009.

[54] Gaskell et al. SIMC Github - https://github.com/JeffersonLab/simc-gfortran. 2009.

[55] T Horn. Global analysis of exclusive kaon and pion electroproduction. *Physical Review C—Nuclear Physics*, 85(1):018202, 2012.

[56] M. Berz and K. Makino. COSY Infinity - https://www.bmtdynamics.org/cosy/. *Michigan State University*, 2023.

[57] J. Volmer et al. Usage of the Heepcheck program. *Thomas Jefferson National Accelerator Facility (TJNAF) Tech. Report*, 1999.

[58] G Huber. Beam and Spectrometer Offsets from Kaon-LT Heep Coincidence Data. *Thomas Jefferson National Accelerator Facility (TJNAF) Hall C Quarterly Analysis Meeting Proceedings*, 2023.

[59] A. Hamdi. Private Communication. *University of Regina*, 2023.

[60] D. Gaskell and P. Bosted. Private Communication. *Thomas Jefferson National Accelerator Facility (TJNAF)*, 2022.

[61] Reza Kazimi et al. CEBAF injector achieved world's best beam quality for three simultaneous beam with a wide range of bunch charges. *Thomas Jefferson National Accelerator Facility (TJNAF) Tech. Report*, 2004.

[62] Alicia Postuma. From Spin to Structure: Beam Spin Asymmetry and the Strong Force. *Thomas Jefferson National Accelerator Facility (TJNAF) Meeting Proceedings*, 2023.

[63] S. Kay. Drift Chamber and Calorimeter Calibrations. *Thomas Jefferson National Accelerator Facility (TJNAF) Tech. Report*, 2019.

Appendix A

Offset Corrected Kaon-LT Experiment Kinematics

This appendix provides experimental kinematics for all Heep coincidence data and the physics data (listed in Section 2.7) after the offset corrections (discussed in Section 4.5.1).

E_b (GeV)	$Q^2 (GeV^2)$	P_{SHMS} (GeV/c)	P_{HMS} (GeV/c)	$\theta_{SHMS}(^\circ)$	$\theta_{HMS}(^\circ)$
10.591	7.3	4.830	6.583	26.21	18.90
8.213	6.5	4.667	4.362	24.06	25.84
6.187	4.8	3.479	3.567	28.59	27.31
4.929	3.4	2.578	3.121	33.56	27.21
3.834	3.4	2.578	2.024	29.37	38.66

Table A: Kinematic settings for all Heep coin data from the Kaon-LT experiment after correction.

E_b(GeV)	ϵ	P_{HMS}	θ_{HMS}	P_{SHMS}	θ^{center}_{SHMS}	θ^{left}_{SHMS}	θ^{right}_{SHMS}
Q^2 = 5.5 (GeV^2), W = 3.02 (GeV)							
10.591	0.53	3,263	23.06	6.828	9.61	12.63	6.56
8.213	0.18	0.961	49.37	6.741	6.27	8.56	-
Q^2 = 4.4 (GeV^2), W = 2.74 (GeV)							
10.591	0.72	4.707	17.13	5.378	12.87	15.87	9.87
8.213	0.48	2.326	27.83	5.378	10.07	13.07	-
Q^2 = 3.0 (GeV^2), W = 2.32 (GeV)							
10.591	0.88	6.583	11.97	3.479	18.24	21.24	15.24
6.187	0.57	2.183	27.30	3.479	13.35	16.34	-
Q^2 = 3.0 (GeV^2), W = 3.14 (GeV)							
10.591	0.67	4.200	14.99	6.041	9.47	12.52	6.56
8.213	0.39	1.819	25.95	6.041	6.97	9.97	-
Q^2 = 2.1 (GeV^2), W = 2.95 (GeV)							
10.591	0.79	5.287	11.22	4.973	10.80	13.81	7.80
6.187	0.25	0.887	36.21	4.973	6.26	8.54	-
Q^2 = 0.5 (GeV^2), W = 2.40 (GeV)							
4.929	0.70	2.064	12.77	2.578	8.92	11.92	6.07
3.834	0.45	0.967	21.20	2.578	6.85	9.85	-

Table B: Detailed breakdown of Kaon-LT kinematics settings after correction.

Appendix B

Detector Calibrations

This appendix provides a brief overview of the calibration procedures for the focal plane detectors used in the Kaon-LT experiment. Proper calibration ensures that the detector signals are accurately converted into physical quantities, which is essential for reliable data analysis. The focal plane detectors include Drift Chambers, Hodoscopes, Cherenkovs and Calorimeters. For each detector, a representative plot illustrating the calibration results is presented. The calibration procedures were carried out by other members of the collaboration. Further details can be found in the cited documents.

Drift Chambers

Drift chamber calibration involves determining timing offsets for each wire to ensure proper alignment of measured drift times. The process begins by setting initial timing corrections and generating an uncalibrated dataset. A calibration routine is then executed, which analyzes the drift time distributions and calculates necessary corrections. The updated calibration parameters are applied, and a second round of data processing is performed to generate a calibrated dataset. The final step involves comparing the uncalibrated and calibrated results to verify improvements in drift distance and residual (as shown in Fig. A). The calibration operates under the assumption that over a given drift cell the particle illumination is uniform. While the before calibration plot shows non-uniformities, the after calibration plot is much flatter, with the exception of a small population spike at the distant end of the cell. For more information on the drift chamber calibrations see [63].

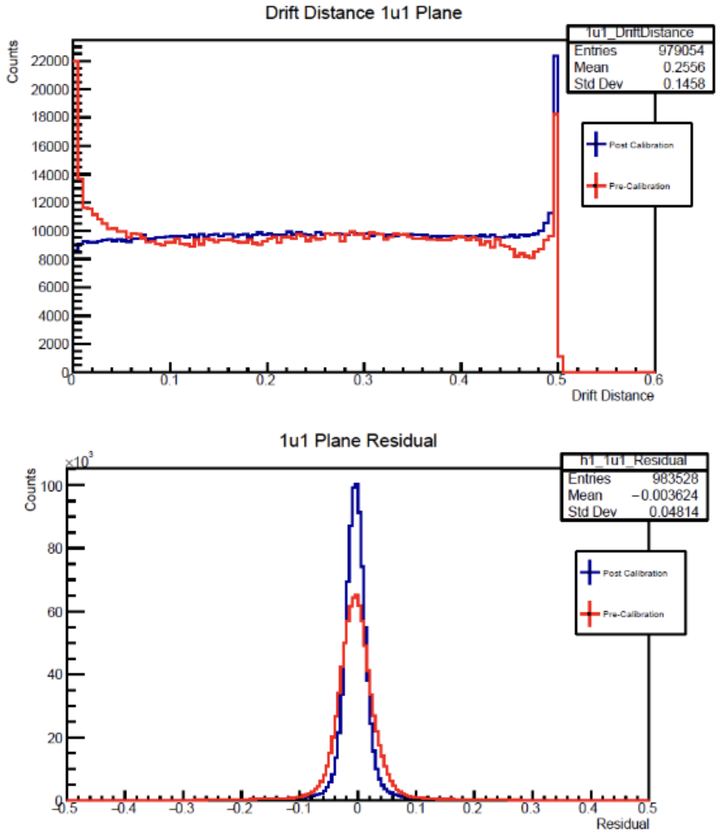

Figure A: Comparison of the drift distance (top) and residual (bottom) for uncalibrated and calibrated data [63].

Hodoscopes

Hodoscope calibration involves determining timing corrections for accurate time-of-flight measurements. The process starts by selecting a reference detector and using an iterative method to adjust timing offsets. Data is initially processed to generate an uncalibrated dataset, which is then analyzed to calculate necessary timing corrections. These corrections account for signal propagation, time-walk effects, and path length variations. The updated calibration parameters are applied, and the data is reprocessed to obtain a calibrated dataset. The final step involves verifying the calibration by comparing the β distributions (as shown in fig. B). For more information on the hodoscope calibrations see [33].

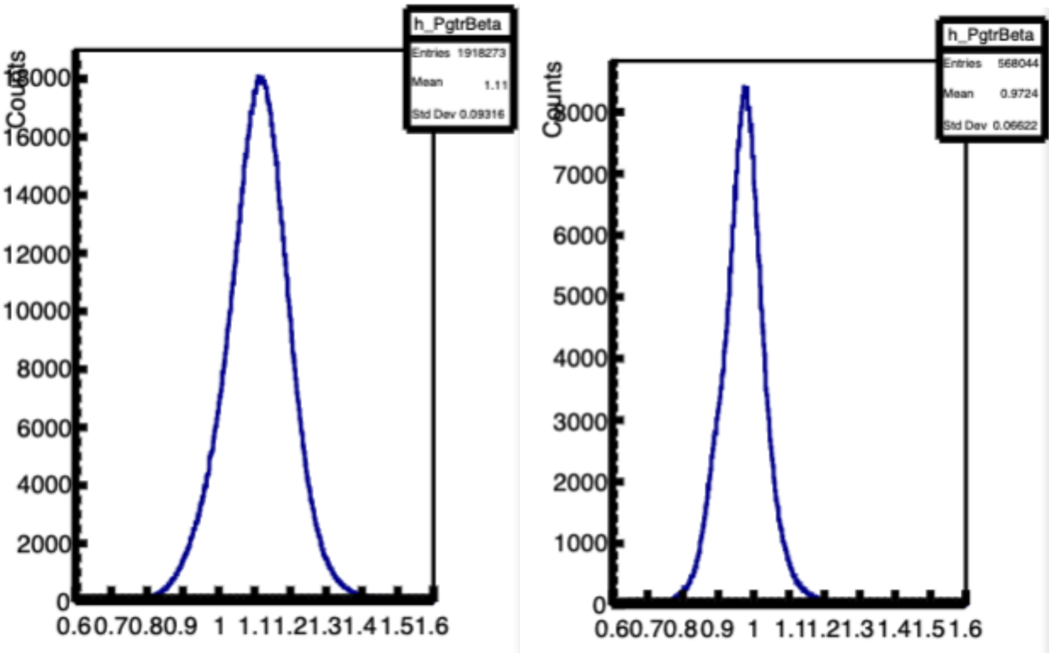

Figure B: Distribution of β before (left) and after (right) hodoscope calibration [59].

Cherenkovs

Cherenkov detector calibration ensures that the single photoelectron response of the detector is correctly aligned at 1. The process involves analyzing the signal from each photomultiplier tube (PMT) in the detector by plotting the signal distribution and fitting a Gaussian function to determine the mean value of the single photoelectron peak. The calibration factor is obtained by taking the inverse of the mean value for each PMT. These new calibration factors replace the previous ones in the parameter file. Once updated, the data is reprocessed with the new calibration values, and the results are compared with the previous dataset. A successful calibration results in the single photoelectron peak aligning at the expected value, ensuring accurate detection efficiency. For more information on the HMS and SHMS Cherenkov detector

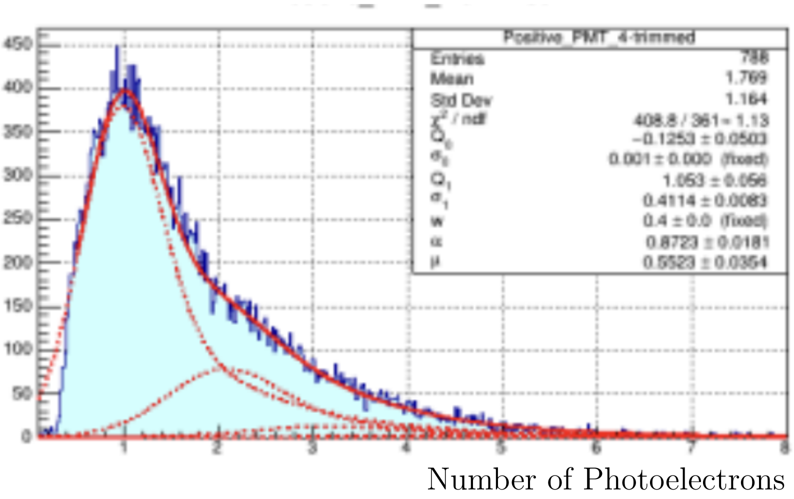

Figure C: Distribution of number of photoelectrons in the aerogel Cherenkov with different fits from the calibration [49].

calibrations see [49, 50].

Calorimeters

Calorimeter calibration ensures that the detected energy signals are accurately converted into normalized energy values. The process involves selecting a high-statistics electron dataset (in the HMS) to provide reliable calibration. The detected energy deposition is analyzed by comparing the normalized track energy (Edep/p) before and after calibration. This process involves the track from drift chamber extrapolated to the calorimeter face, and only those blocks within threshold distance of that track which are above threshold energy deposit are included. Blocks far from the extrapolated track and blocks below the threshold are excluded. The calibration involves adjusting gain constants to align the summed energy for an electron cluster at 1. These updated values replace the previous calibration parameters. After applying the new calibration, the data is reprocessed, and the results are compared with the uncalibrated dataset. A successful calibration ensures that the normalized track energy distribution is correctly peaked at the expected value for specific particle type, verifying the calorimeter's efficiency. For more information on the calorimeter calibrations see [63].

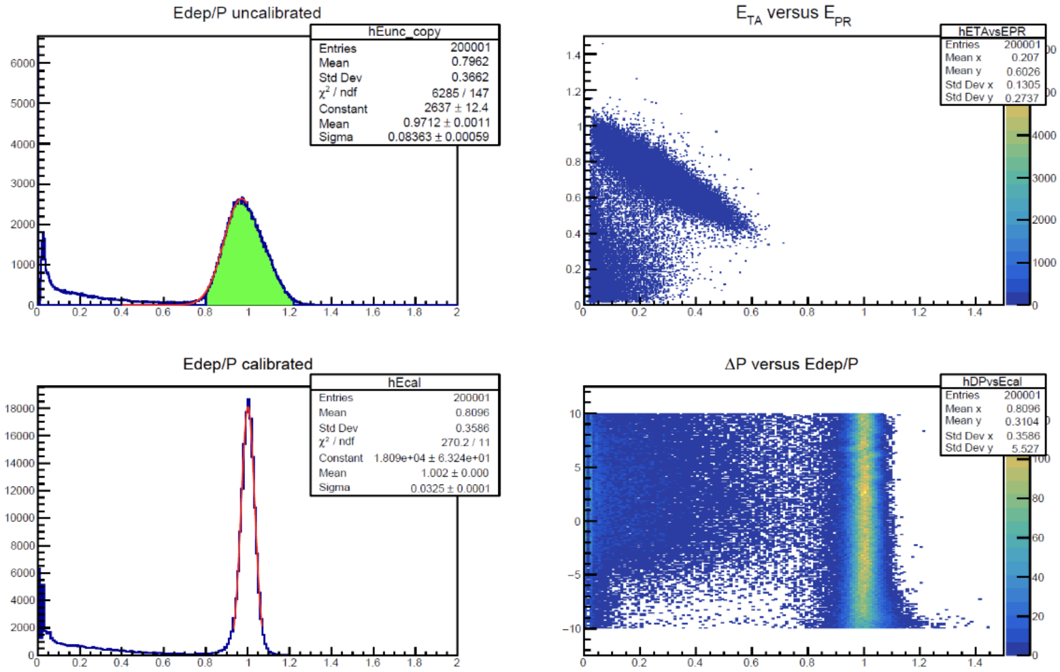

Figure D: Distribution of normalized energy before (top) and after (bottom) the calorimeter calibration for electrons in the HMS [63].

Appendix C

Additional Δ^0 Shape Study Figures

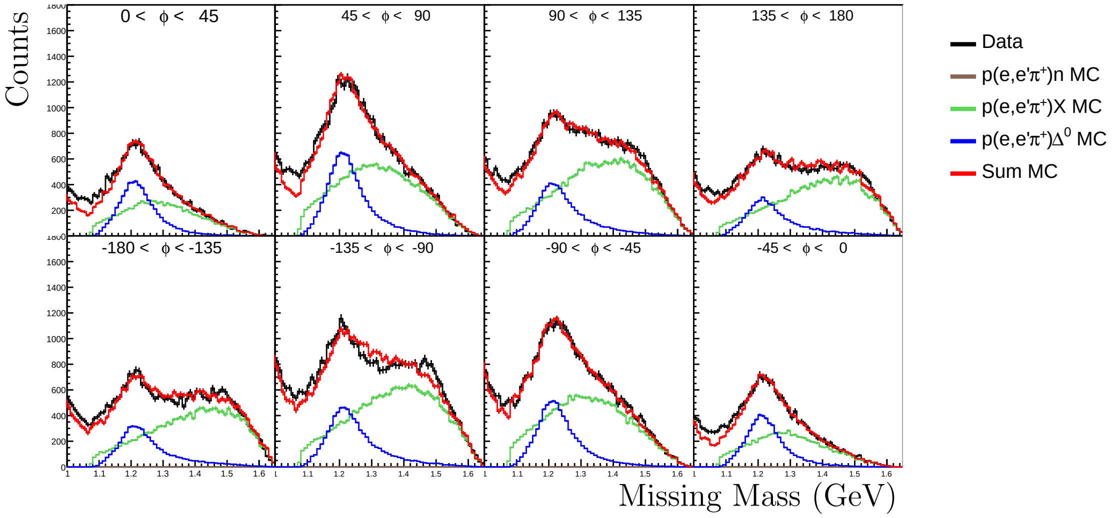

Figure E: Shape study for missing mass distribution in the Δ^0 region for center SHMS setting data in each ϕ bin ($Q^2 = 3.0$ GeV^2, $W = 3.14$ GeV).

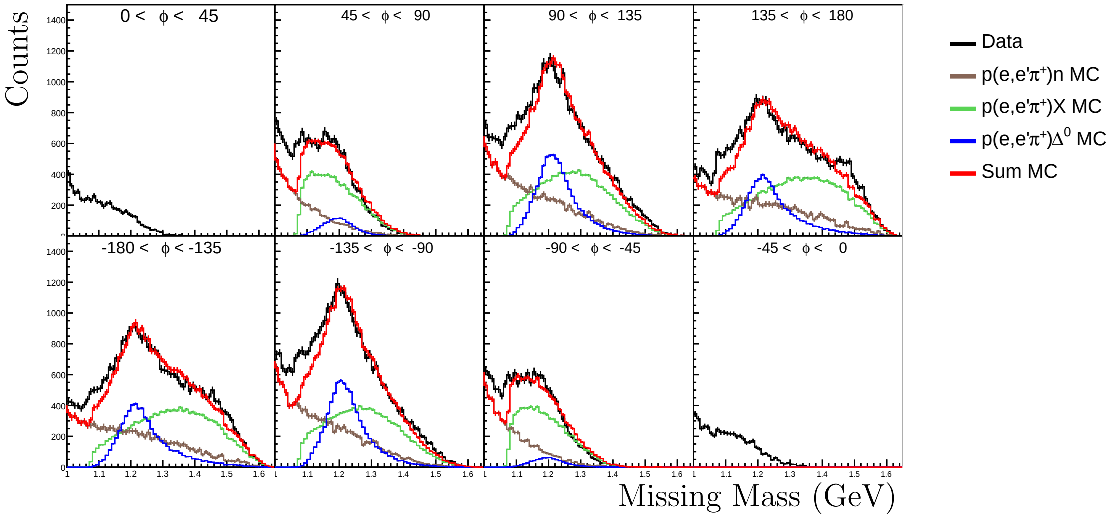

Figure F: Shape study for missing mass distribution in the Δ^0 region for center SHMS setting data in each ϕ bin ($Q^2 = 3.0$ GeV^2, $W = 2.32$ GeV).

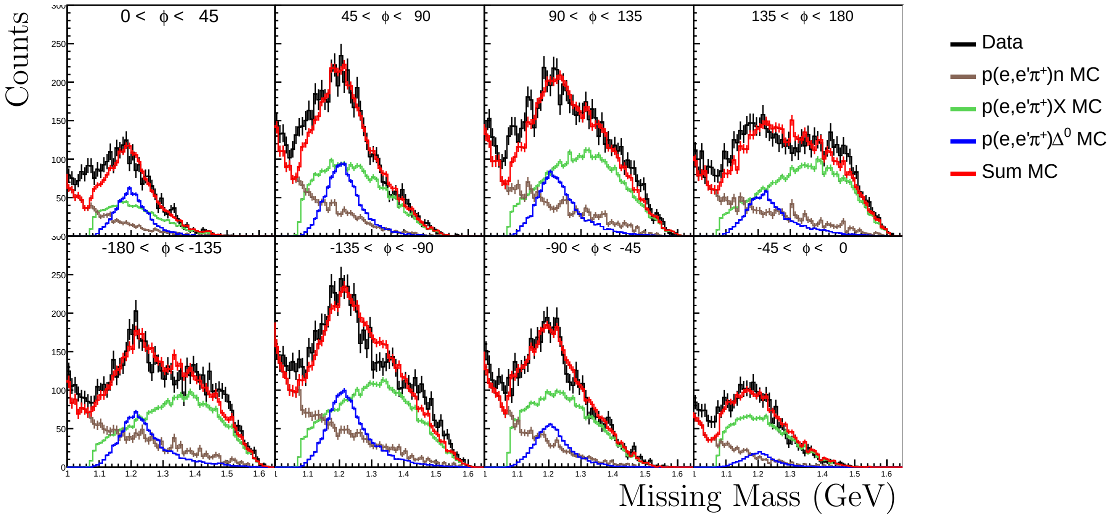

Figure G: Shape study for missing mass distribution in the Δ^0 region for center SHMS setting data in each ϕ bin ($Q^2 = 4.4$ GeV^2, $W = 2.74$ GeV).

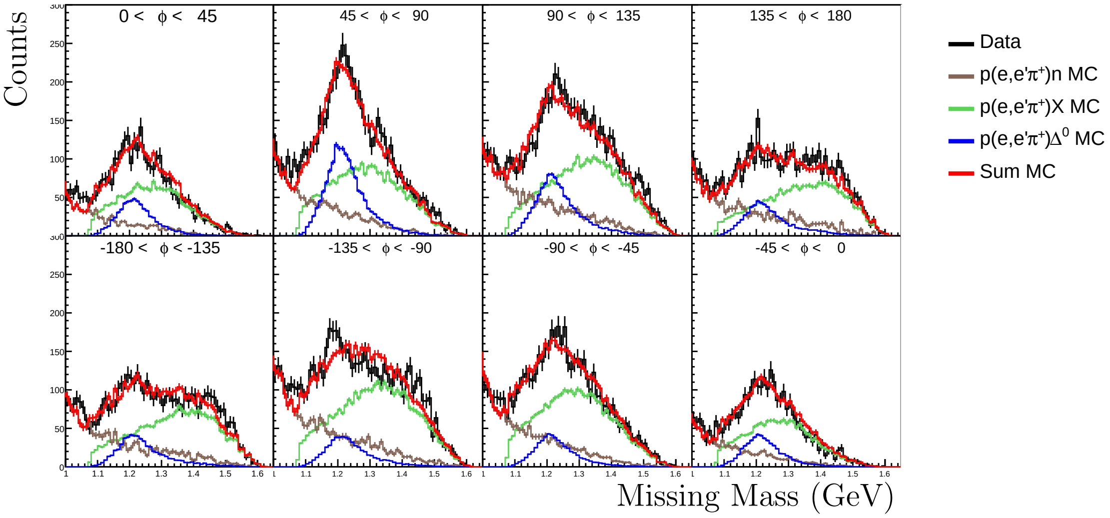

Figure H: Shape study for missing mass distribution in the Δ^0 region for center SHMS setting data in each ϕ bin ($Q^2 = 5.5$ GeV^2, $W = 3.02$ GeV).